FUNDAMENTAL PROPERTIES AND PROCESSES OF ENERGETIC MATERIALS

A Dissertation

by

OSCAR ULISES OJEDA MOTA

Submitted to the Office of Graduate Studies of
Texas A&M University
in partial fulfillment of the requirements for the degree of

DOCTOR OF PHILOSOPHY

August 2011

Major Subject: Chemical Engineering

Fundamental Properties and Processes

of Energetic Materials

FUNDAMENTAL PROPERTIES AND PROCESSES

OF ENERGETIC MATERIALS

A Dissertation

by

OSCAR ULISES OJEDA MOTA

Submitted to the Office of Graduate Studies of
Texas A&M University
in partial fulfillment of the requirements for the degree of

DOCTOR OF PHILOSOPHY

Approved by:

Chair of Committee,	Tahir Cagin
Committee Members,	Raymundo Arroyave
	Mahmoud El-Halwagi
	M. Sam Mannan
Head of Department,	Michael Pishko

August 2011

Major Subject: Chemical Engineering

ABSTRACT

Fundamental Properties and Processes

of Energetic Materials. (August 2011)

Oscar Ulises Ojeda Mota, B.S. National Polytechnic Institute;

M.S., University of North Texas

Chair of Advisory Committee: Dr. Tahir Cagin

Energetic materials comprise a set of systems of tremendous technological importance. Besides helping shape landscapes to establish communications, they have been used to reach fuel reservoirs, deploy safety bags and prevent heart strokes. Understanding its behavior can help in attaining strategic and tactical superiority, and importantly, preserve lives of people who handle these materials.

The large discrepancy in length and time scales at which characteristic processes of energetic materials are of relevance pose a major challenge for current simulation techniques. We present a systematic study of crystalline energetic materials of different sensitivity and analyze their properties at different theoretical levels. Equilibrium structures, vibrational frequencies, conformational rearrangement and mechanical properties can be calculated within the density functional theory and molecular dynamics at finite temperatures. We have found marked differences in the calculated properties in systems with ranging sensitivities. Reactions at elevated temperatures have been studied using *ab initio* molecular dynamics method for crystals of nitroethane.

Furthermore, while presenting the state of the art of energetic materials modeling, the limitations of each methodology are also discussed. Prospective systems and an elasticity driven approach that can be applied to other type of materials is also presented.

DEDICATION

To my Family

ACKNOWLEDGEMENTS

I would like to thank my committee chair, Prof. Tahir Cagin, and my committee members, Dr. Raymundo Arroyave, Prof. Mahmoud El-Halwagi and Prof. M. Sam Mannan, for their guidance, support and motivation through example, throughout the course of this research.

Thanks also go to my friends and colleagues and the department faculty and staff for making my time at Texas A&M University an unforgettable experience. I also want to extend my gratitude to CONACYT, which provided funding for the early part of my doctoral program. I would like to thank the following: Dr. Mustafa Ulludogan and Dr. Cem Sevik for sharing their knowledge with me, Dr. Lisa Perez, the Laboratory for Molecular Simulation at Texas A&M University, and Dr. Vellas and the Supercomputing Centers of Texas A&M College Station and Texas A&M Qatar for providing support and computer time. I particularly appreciate the fruitful input of Dr. Sreeram Vaddiraju.

I also would like to acknowledge my mentors from the Escuela Superior de Ingeniería Química e Industrias Extractivas, Prof. Miguel Angel Valenzuela, and the team from the Laboratorio de Catálisis y Materiales Ambiental. From the Universidad Autónoma de Coahuila, I would like to thank Prof. Oscar Mendoza (R.I.P.) and Ms. Gloria Natividad. They have made possible our continuous education.

My endless gratitude to Oscar Miguel, Norma Yolanda, and Rodrigo Miguel for their encouragement and to my wife Sarah Cecilia, for her patience and love.

TABLE OF CONTENTS

CHAPTER Page

LIST OF FIGURES

FIGURE Page

FIGURE Page

FIGURE Page

FIGURE Page

LIST OF TABLES

TABLE Page

CHAPTER I

INTRODUCTION*

Energetic Materials

The development of energetic materials for the use of human beings started with the development of black powder some 2000 years ago[1]. Black powder consists of the granular ingredients sulfur (S), charcoal, and saltpeter, (KNO_3) which provide oxygen to the combustion reaction. Energetic materials (EM) are stable organic compounds[2] with varying enthalpies of formation. Some of the most commonly used materials are nitromethane (NM, Figure 1.1), 1,3,5-triamino-2,4,6-trinitrotoluene (TATB), 1,3-dinitrooxy-2,2-bis(nitrooxymethyl) propane or pentaerythritol tetranitrate (PETN) and the compound known as her majesty explosive, HMX, amongst others. Their applications range from initiators in safety bags to detonation charges, and from propellants to secondary explosives, making them of particular technological relevance. They are characterized by their ability to undergo chemical transformations starting from the initiation of reactions at the molecular level, to sustaining a supersonic detonation at macroscopic scale. This multi-scale phenomenon is observed if enough external energy, either in the form of a heat pulse or a large pressure wave, is supplied to a secondary EM to react, a detonation front will form. In this front, a sudden increase in the material density will be accompanied by a release of temperature, detonation products (usually hot gases), and light, in the opposite direction of the detonation front.

This dissertation follows the style of *The Journal of Physical Chemistry B*.

This sudden release in pressure and temperature, will affect the un-reacted mass, ahead of the detonation front, increasing the velocity of its propagation. Sensitivity is related to the materials tendency to initiate under conditions that would be otherwise considered safe[3]. It is well known that EM display anisotropic sensitivity to heat and mechanical shock[4-7]. Naturally, this has raised serious issues related to safety, logistics, time burdens related to handling of these materials and to additional costs associated with them. Impact Sensitivity is commonly assessed by the drop height test in which the distance for a 50% chance of detonation of a standard weight is measured (Table 1.1). For the most commonly used secondary energetic materials, we can find the following experimental results[8]:

Table 1.1 Drop height test for selected energetic materials[8].

	H_{50}/cm
TATB	>320
RDX	22/41
β-HMX	26/37
PETN	12/37'
NM	-

In general, prediction of the reactivity and sensitivity of an explosive is complex since it depends on the interaction of mechanical, chemical and thermodynamic conditions. It is well known that the impact/shock sensitivity of the EM depend strongly on the geometry of the contact relative to the shape of the sample, the material's structure, morphology and its chemical and thermodynamic properties[9]. The time scales and characteristic lengths can vary from a few angstroms, as in the case of lengths of

bonds and ordering of molecules within a crystal, to a few nanometers; as in the case of the thickness of initiating reactive layer, and up to a large distance as in the case of the of the material experiencing a shock compression of the expanding wave. The study of effect of the steep changes in density and pressure as the shock propagates through the media if defined through a continuum description requires incorporation of high gradients and rapid variation of field variables[10].

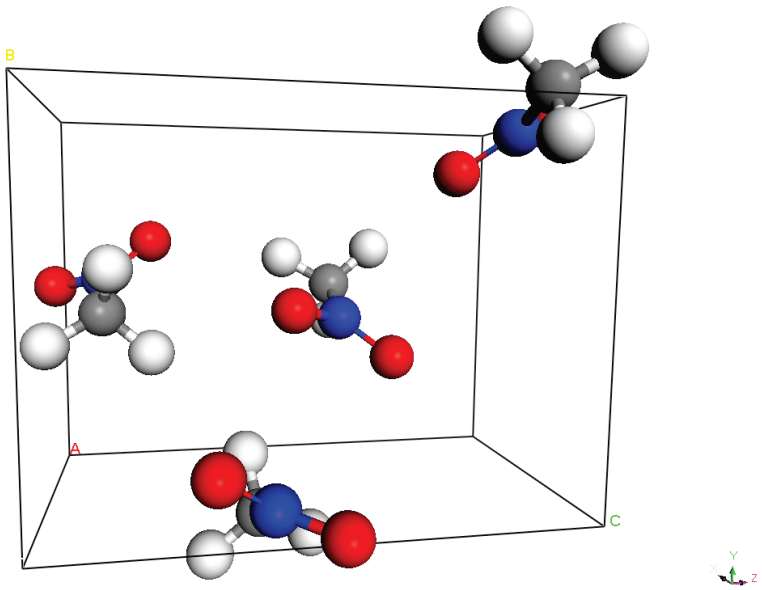

Figure 1.1 NM unit cell.

The need for a multi-scale modeling approach that can probe a material system to provide a description of processes ranging from molecular level to macroscopic behavior is thus advantageous. This is particularly pertinent to the study of energetic materials (EM); commonly classified as explosives because upon ignition they produce a detonation front. This is the process of a supersonic combustion that produces a shock

wave and a reaction zone behind it[11]. Assuming a continuous elastic media, the irreversible adiabatic compression zone left behind the shock wave causes the material to increase its temperature to the point of ignition and cause detonation[12] (viz. deflagration, which is a much slower reaction such as the burning of wood). In this way, the shock wave propagates, effectively steeping the density or pressure change as it moves through the media. Due to the complex nature of the processes related to these materials, some experimental data has just started to emerge for some of them[13]. In order to understand the chemical, physical and mechanical behavior of these materials one needs to employ theories ranging from quantum mechanics/quantum chemistry, molecular dynamics with reactive an non-reactive potentials[14], statistical thermodynamics[15,16], micromechanics, solid mechanics and fluid dynamics allowing for reactions. Although the theory of explosions in gas phase is well developed[17,18], for a condensed detonating secondary energetic material, which is initiated by another more reactive material, like a metal azide or perchlorates[19,20] a molecular description is far from being complete[21,22]. In the formulation of plastic bonded explosives, crystals of energetic materials are fragmented and compressed with a binder. In order to describe the dynamic response of explosive determination of their mechanical properties is essential, since localization of strain energy has long been the suspect of the formation of reaction zones[23], or "hot-spots". In addition to this, fracture along a given plane can act as energy barriers and hinder a reaction from completing, hence causing unexpected behavior in some cases. In the following sections, we aim to present our current effort and relevant results in modeling the complex behavior of energetic materials as well as

referring to critical work conducted in this area by other researchers. Finite linear stress models (i.e., second order elastic constants) may give a best initial approximation to the response of the material under hydrostatic pressures. However, in order to fully represent the behavior of the material under large strains, higher order contributions, as well as a full understanding of the material's anisotropic response. This will require observing any structural rearrangements that the material may experience, and compare those to changes in their electronic structure, both in hydrostatic and non-hydrostatic conditions and with the inclusion of defects. Thermodynamic parameters can further be obtained by calculation of the vibrational frequencies[24]. These calculations are allowed in part by the development of the modern computational methods. In order to study the reactions in condensed phase we have used *ab initio* molecular dynamics methods at elevated temperatures. Furthermore, current advances in the area as well as the limitations and failures of each methodology are discussed.

Predictors and Models of Energetic Materials

Besides decreasing the sensitivity by rising the energy absorption of a material[25], the density of an EM is related to the speed of detonation in a compressive shock by the Huginot equation[26]. On mesoscale lengths, models applied to the processing of energetic materials[27,28], and the effect of detonation in pressure shock-waves has been investigated[29-31]. This has been further supported by molecular dynamic simulations which aid to develop equations of state[32,33], and were the account of anisotropy present in the crystal structure has not been of particular insight[34-40 40].

The aforementioned relationships have been successfully applied to predict some isotropic properties, such as sensitivity to an electric spark[41]. However, like in many crystalline solids, anisotropy can be observed[42]; within a single crystal of a given polymorph. The sensitivities to detonation can vary with the direction of the shockwaves with respect to crystallographic axes[25,43], giving rise to different physical observables such as slip plane, fracture type[44], and even electromagnetic spectra[45]

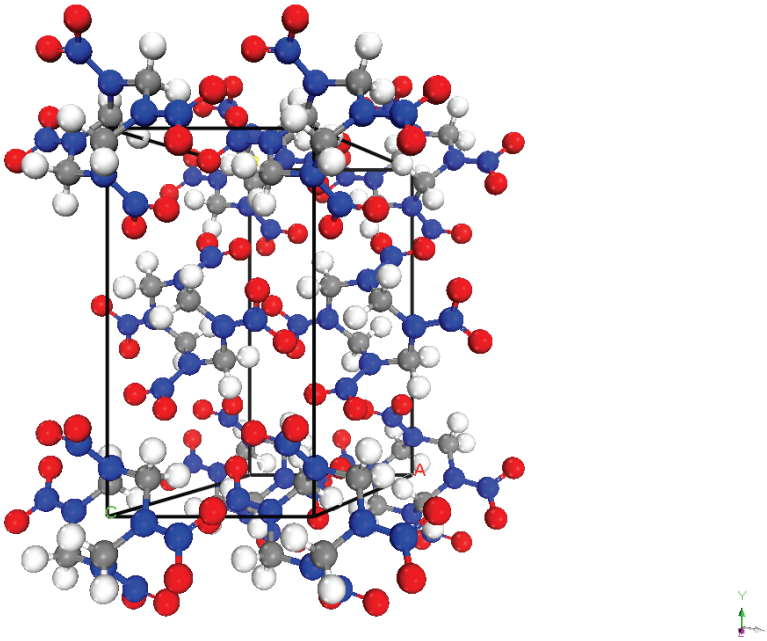

Figure 1.2 β-HMX unit cell.

For secondary energetic materials, anisotropy is particular relevance, since an external primary energetic material, or initiator, is commonly used. Coupling of initiator and anisotropic behavior can give rise to tailored properties.

Table 1.2 Sensitivity models for energetic materials.

Model	Advantages	Observations.
Oxygen Balance Model	Simple	Not a clear trend in chemical structures.
Heats of Formation/Reaction- and Sensitivity[46,47]	Takes into account chemical information	No differentiation between shock/impact sensitivities.
Heat Localization/Critical Size[48]	Accounts for thermal/strain effects	No discern in chemical nature of EM's
Charges/EPS surfaces of EM[49]	First Structure/Properties Relationship model	Applicable only to specific type of EM's
Spectroscopic Predictors[50] (Raman[51],NMR[52,53])	Discern between Low Velocity Detonation/Shock Compression	For ideal EM's
Metallization/Exitonic Model[54,55] Dynamic metallization[56]	Applicable to Shear deformation of Fox-7, probably to defective RDX and nm under shock compression.	Plausible explanation to detonation of specific (i.e., Fox-7) systems.
Effect of Defects/Work Hardening[57]	Account for non-ideal EM's. In some cases the effect of crystal structure is taken into account	The type of defect should most likely be discerned.
Mechano-chemical Model[58,59]	First Physical Description Relation of EM's at initiation	Contradicting Outcomes, Effect of defects and thermal transport is unclear. No direct experimental evidence
Neural Networks[60,61]	First Use of NN to predict EM's sensitivity	Large errors.

Up until 1995, the research area of molecular modeling and EM focused on studying simple molecules[62-67] and their electrostatic potentials[68]. These studies were focused on the heat of formation of some solid nitrated energetic materials, and involved the calculation of optimized structures obtained from ab-initio methods[69] (viz. experimentally obtained structures). Also the theoretical development of future energetic

materials was laid out towards high density substituted olefin rings and explosive polymer compunds[25,70]. It is around these years when the first aim towards modeling of the chemistry in complex molecules using a Hartree-Fock method[71], and the use of reactive force fields for molecular dynamics simulations was also established[72]. Some gas phase studies encompass decomposition mechanisms[73] studies, geometry and electronic structure optimization[74-77], heats of formation[49,78-80] and models for correlation of sensitivity and heats of detonation[47,81-84]. Earlier studies on the thermochemical properties of β-HMX (Figure 1.2) and its polymorphic phases[85-87 88 89] for schemes based on isodesmic (having the same type of bonds) and isogyric (spin-conserved) in which the effect of different basis sets is explored, indicate that a larger 6-311++G(3df,3pd) basis set on geometries optimized with the 6-31G(d) basis set[90] are need for accurate representation of our system. We will explore the effects of basis sets more into deep in an upcoming chapter. More recently, coupling of phonons to low frequency or "doorway" modes have been suggested as an initiation path in energetic materials[91]. So far there is not a single model that correctly predicts the sensitivity and behavior of secondary energetic materials. As we shall demonstrate, the difficulties lie in the need to obtain information at different scales and from different thermodynamic conditions. We include (Table 1.2) as a brief summary for the reader, highlights of some of the proposed models based on chemical and physical information of energetic materials.

Relevant to continuum length scales is the theory of unsteady state combustion phenomena in homogeneous systems, which was put forward by Zel'dovich. Since the

relaxation time of combustion in gas phase is very short as compared to the relaxation time of heat propagating in condensed phase, then combustion in the gas phase is determined by the thin condensed phase layer adjacent to the interface[29]. The process is examined by solving the heat conduction equation in condensed phase:

$$\frac{\partial T}{\partial t} = a\frac{\partial^2 T}{\partial x^2} - u\frac{\partial T}{\partial x} \qquad (1)$$

Where u(t) is the linear burning rate, a is the thermal diffusivity of the condensed phase, and the periodic boundary conditions are, x=0 at T=Ts (surface), T=Ta (ambient) as x goes to infinity. Using his model, it has been predicted that for slow (e.g. lower than 2nd order) reaction kinetics there is a zone of maximum temperature adjacent to the interface, at the condensed phase material; this is, the burning rate controlling zone lies in the condensed phase[92]. This is a relevant result taking into account that it was assumed previously that the burning rate controlling zone existed in the gas phase due to its proportionality to the pressure: studies should be directed towards a closer look at physical and chemical properties of the materials[93] for the ignition and growth models proposed[94-96], specially in the condensed phase.

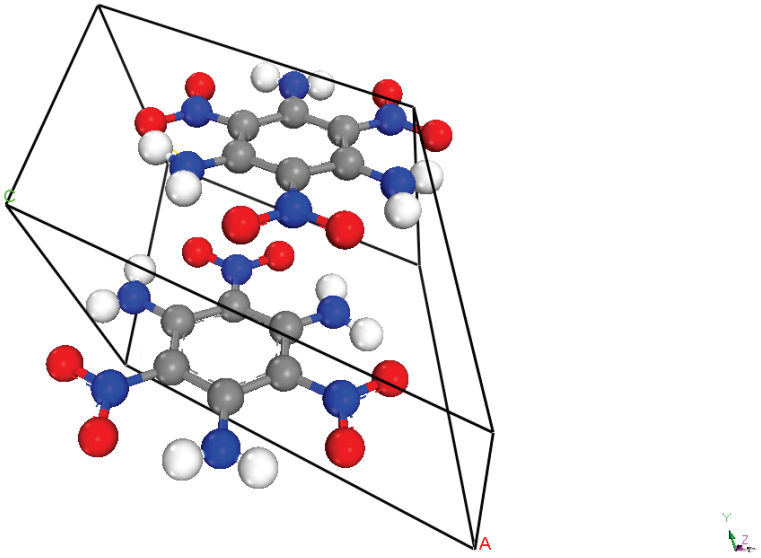

Figure 1.3 TATB unit cell.

We will look for thermodynamic properties and process fundamental of energetic materials, and compare and contrast the behavior of secondary materials of different sensitivities. This will prove that no overgeneralization can be valid, accounting for the application of these materials, and that structure and orientation can play an important role for different observed experimental behavior. The foundations laid here will serve as a model for future studies on energetic materials, and as methodology to probe through computational methods, of sensitivity markers of newly or yet to be synthesized energetic materials.

Methods and Computational Details

Energetic materials systems usually have a low symmetry crystal structures. TATB, the system with the lowest symmetry in the unit cell, has a space group P-1, only inversion as the symmetry operation (Figure 1.3). The higher symmetry system, PETN, is a tetragonal crystal, but its tetrahedral four arm chemical structure with a sp^3

hybridized central carbon has four resonant nitro groups at the end of these arms, with this stiffer structure (Figure 1.4).

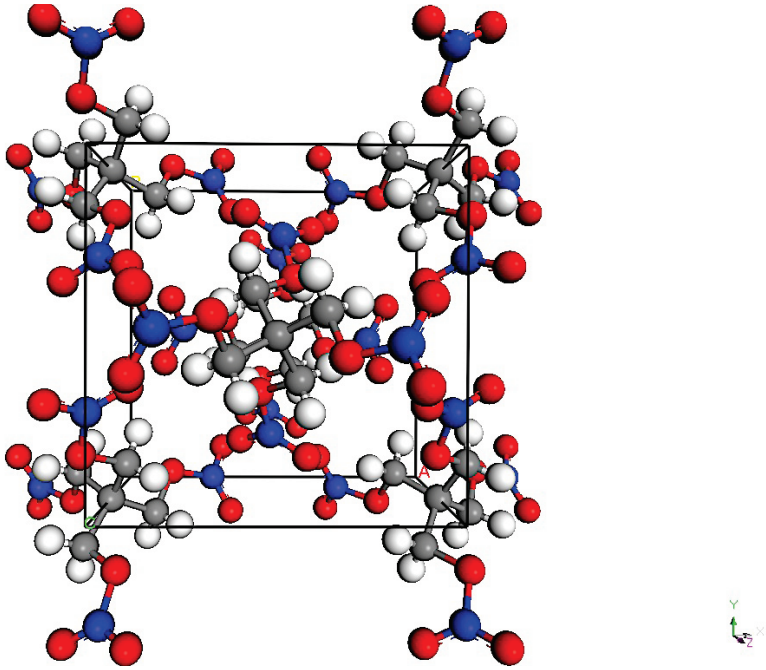

Figure 1.4 PETN unit cell.

Reduced symmetry calls for convergence to small tolerances in both energy (smaller than $3x10^{-6}$ eV, or 10^{-7} A.U.) of the self-consistent field cycle, and forces ($5x10^{-4}$eV/Å) are required, in *ab initio* quantum chemistry calculations. These calculations are conducted within the density functional theory[97] level, with gradient corrected Perdew-Burke- Ernzerhof (PBE) functional for the exchange and correlation[98]In the case of plane-wave approximation, we have used both ultra-hard and regular projected-augmented wave method potential lists (PAW), with the use of the VASP software. At the above tolerances used, convergence to 700 eV for normal potentials, and 1000 eV for ultra-hard potentials are employed. K-point sampling space converged at a Monkhorst-Pack grid size from 2x2x2 to 6x6x6 symmetric mesh size. Troullier-Martin

pseudopotentials[99], as well as PAW potentials[100-104] for the case of plane wave basis have been used. We will refer to the particular difficulties arising from the use of plane wave approximations in the treatment of molecular crystals in the forthcoming chapter. For the cases of parallel node runs, all the appropriate parameters have been optimized for work performed in each particular platform.

Further calculations on the systems have been performed with the Crystal06 package using a 6-31G* basis set. By means of localized basis sets that are used to represent all-electron systems (LCAO method), we have performed first principles calculations on aforementioned systems. For these calculations, extended basis sets[105] with primitive coefficients for carbon, hydrogen, nitrogen and oxygen, as implemented in the crystal06 package were employed[106]. Initial structures for these crystals were obtained from the Cambridge crystallographic data base[107]. In order to understand the potential energy landscape of 1,3,5-triamino-2,4,6-trinitrobenzene (TATB), *ab inito* calculations with the use of localized basis sets[108,109] are conducted on the TATB single molecule and TATB dimer structure. Both density functional theory[97,110] (DFT) calculations and the Möller-Plesset perturbation methods of singles and doubles (MP2) have been performed[111,112] to account for correlation and dispersive forces. In the long wavelength limit, *ab initio* methods allow for the study of changes with respect to a corresponding pressure via vibrational frequency calculations. We have used the optimized geometries for each system to obtain analytical first derivatives with respect to ionic displacements. Each atom is moved in directions along the three axis by a small step; the energy is then calculated self consistently. A total of 3N+1 calculations should be performed, but this

number is reduced when the symmetries of crystal are taken into account, as it is commonly implemented in the crystal06 code[113,114]. The analytical first derivatives are then used to construct the "Hessian" at Γ point through numerical differentiation. The Hessian is the matrix of second derivatives, or force constants that is diagonalized to calculate the mass-weighted dynamical matrix. The number of eigenvalues obtained follows the 3N-6 rule for non-linear molecules, where N is the number of atoms in the molecule and 6 modes correspond to translations and rotations in three dimensions. Calculation of the intensities is related to the derivative of the dipole moment with respect to the normal mode coordinate, times its degeneracy. The dipole moment can be obtained from the calculation of the Born effective charges[115,116], i.e.; the proportionality constant in the change of polarizabilities in one direction, with respect to a displacement along another direction. Large integration grids (XLGRID) and number of K-points (6x6x6 mesh) are required to fulfill the Born charge sum-rule, or the neutrality of the cell. We have further used a tolerance for the differences in the energy for a SCF calculation with a value of $1x10^{-8}$ A.U.

Additionally, we have performed molecular mechanics and molecular dynamics calculations with the DREIDING force field[117], as well as the following force fields; CVFF[118-125], Compass[126-129] and Universal[130]. Whenever force field assigned atomic charges were not available (i.e. Universal, Dre6), charges are determined from the Charge Equilibration (QEq) method[131]. In specific cases, we have employed Mulliken[132] charges form equilibrium DFT structures to perform dynamic modeling. Simulations with the Isothermal Isobaric ensemble (NPT) the codes LAMMPS[133], Cerius2 and

Materials Studio have been used. The DREX6 force field has been adapted to both LAMMPS and MaterialsStudio Forcite module. An equilibration time of at least 400 picoseconds (ps) is required for all the runs, with the averages taken over 200 ps long samples of a molecular dynamics simulation with an integration step size of 1 femtosecond (fs). Nose-Hoover thermostats and barostats are employed[134,135]. Multiple in-house scripts and codes have been developed to analyze and expedite data submission/and analysis. The calculation of the elastic properties from methods that entail finite deformations from first principles methods comprises its own set of difficulties. Issues like the type of approximation used, the type and size of deformation applied and the effect of higher order terms will be studied in depth in a forthcoming chapter.

Since the earlier studies[136]; it was clear that a systematic study of the structure and properties of energetic materials was not a simple task that could give meaningful information by the use of a generic basis set. For example, the initial calculated energy barrier for the rearrangement[137] of nitromethane (NM) to methylnitrite (MNT) was 47.0 Kcal/mol. Later, the value of 73.5 Kcal/mol reported by Mckee[138] indicated dissociation of NM as the most probable pathway. Nonetheless, Hu's group[139] reported NM breakdown via C-N bond rupture (61.9 kcal/mol) and Nguyen's group[140] have reported direct dissociation to CH_3 and NO_2 via radical formation (63 kcal/mol). Twenty years later, investigations with a transfer Hamiltonian indicates that the radical formation is the most probable pathway[141].

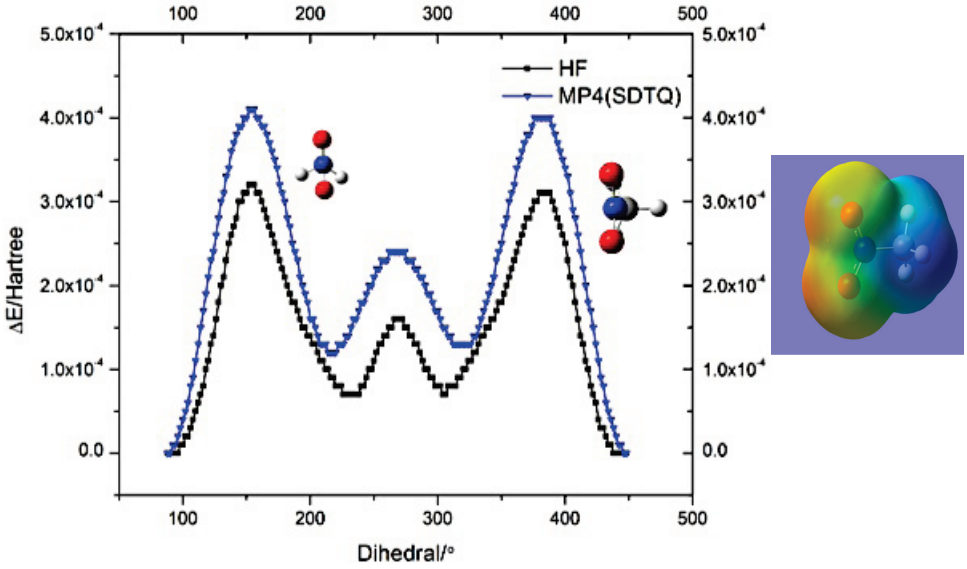

Figure 1.5 Potential energy surface of NM (left). Optimized molecular structure, with a charge isosurface of 0.1 atomic units (A.U.). The electrostatic potential mapped. Oxygen: red, nitrogen: blue, carbon: grey, hydrogen: white.

The adiabatic potential energy surface (PES) of the simplest secondary energetic material, NM, shows a multiple energy minima, caused by the interaction of the nitro oxygen atoms with the methyl hydrogen (Figure 1.5). Hydrogen, the central carbon atom, and one of the nitro group's oxygen atoms form the dihedral angle, initially at the optimized position ca. 90º. Increments of 2º used. We can expect a more complex potential energy surface (PES) for larger and more complex molecules like pentaerythritoltetranitrate [142] (PETN) and cyclotrimethylenetrinitramine (RDX).

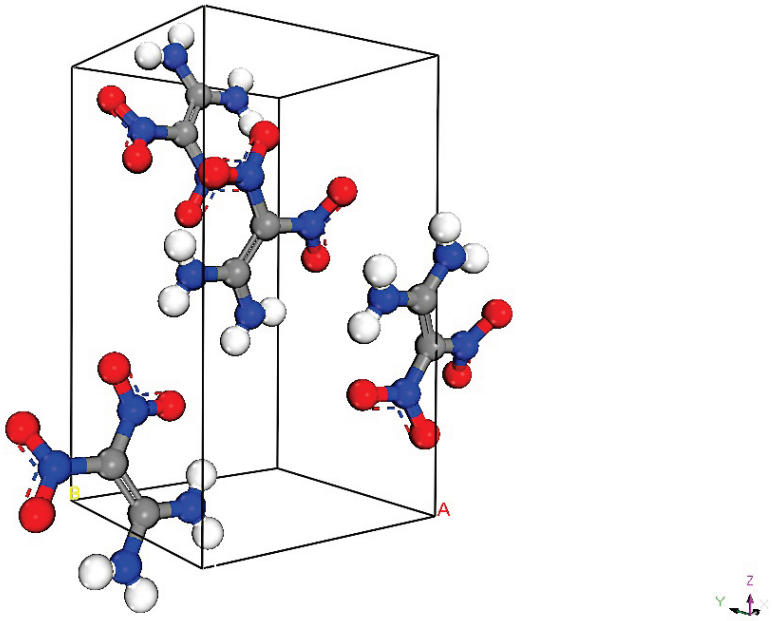

Figure 1.6 Fox-7 unit cell.

Due to the size and low symmetry of the relevant systems, the appearance of studies with periodic boundary condition studies came about much later[77,143,144] with the use of the Hartree-Fock approximation[145] and tools like fixed bonds/angles to reduce the degrees of freedom and thus the size of the calculations[71]. We have focused first on developing knowledge at the electronic level within the DFT approximation on the following systems; β-HMX[146-148], FOX-7[149-153] (Figure 1.6), 1,3,5-triamino-2,4,6-trinitrobenzene (TATB)[154-157], NM[158-160] and PETN-i[161-164]}. Other molecular crystals also studied are; 2-4-6-trinitrotoluene[165-168] (Figure 1.7), ethanol[169], benzene[170-172],urea[173-175], cyclohexa-2,5-diene-1,4-dione[176](p-quinone), Benzene-1,3-diol (resorcinol)[177], γ-glycine[178]. We will refer to these in detail in subsequent chapters.

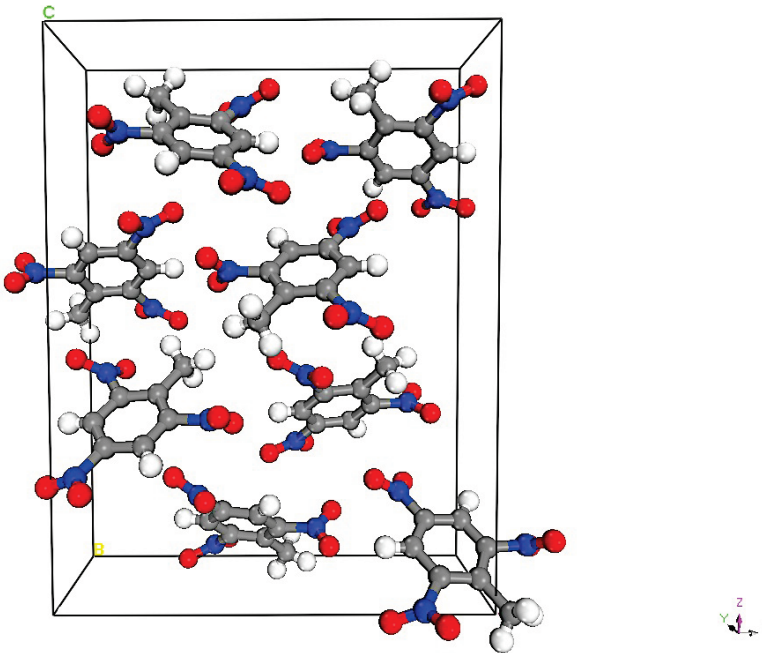

Figure 1.7 TNT unit cell.

Besides of its use in constitutive relations, we shall confirm in subsequent chapters that elasticity is an important property with particular behavior in specific types of secondary EM. Since all engineering models start from fundamental thermodynamic relations, obtained from the equation of state, we will continue with their study. We will start our incursion by comparing properties of other simpler systems for which abundant experimental information is available; binary metal nitrides. An accurate representation of our system will enable us to pursue other type of information, like second order elasticity, and anisotropic properties at elevated temperatures and pressures.

CHAPTER II

ELECTRONIC STRUCTURE

Metal Nitrides: A Comparison

Group AIII-nitride compounds are commonly regarded as wide band-gap semiconductors[179] with very high thermal conductivity which have important technological use[180-186]. More recently, the study of these material has been focused on their application as structural ceramics due to its chemical and radiation inertness[187-191] and to their higher energy of formation required to create defects[192]. In particular, aluminum nitride (AlN) has been successfully employed in applications ranging from microprocessors, diodes, and microelectronic circuits to environmental replacements for other type of oxides[193-195]. Being the most ionic of the group III-nitrides and accrue its high bulk resitivity[181,196-198] (ca. 10^{11} Ohm/cm^2) they have been studied as component of 1 dimensional structures with tailored optical properties[199,200]. To our knowledge previous density functional theory[97] (DFT) studies that involved the study of binary nitrides system under different pressures via plane wave pseudo-potentials (PWPP) results are performed with atmospheric pressure c/a ratios,[201-203] using the FLAPW method or the linear muffin-tin-orbital (LMTO) method[192] or the linearized augmented plane-waves (LAPAW) [184] with the generalized gradient approximation (GGA) method[204]. In these calculations, projector augmented plane wave type of potentials[205] with Perdew-Berke-Ernzerhof exchange correlation functionals [206] (hard version) were employed with the intention of obtaining energy-volume and energy pressure

characteristics at the optimized (relaxed) structural parameters (e.g. c/a ratio) for two binary nitride ceramics; aluminum nitride and zirconium nitride. The electronic structure of the former is also included.

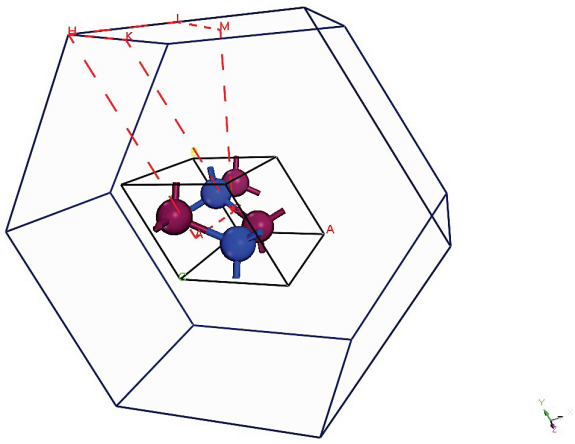

Figure 2.1 Wurzite AlN. (Nitrogen colored blue) High symmetry points in the first irreducible Brillouin Zone are labeled in orange.

The PAW pseudopotentials reconstruct the exact valence wave function with all nodes in the core regions, in addition to the fact of smaller core radii than ultrasoft Vanderbilt (US) pseudopotentials, PAW potentials are more accurate in describing mechanical properties of materials, whenever spin polarized calculations are not required. Either the conjugate- gradient iterative scheme or the block Davidson method for the Kuhn-Sham matrix diagonalization as implemented in the commercial software package VASP™ was employed. An effective kinetic energy cutoff of 1 keV is employed for the calculations, with a Monkhorst-Pack mesh grid size of 10x10x10 for the case of cubic structures, (11x11x11 size else).

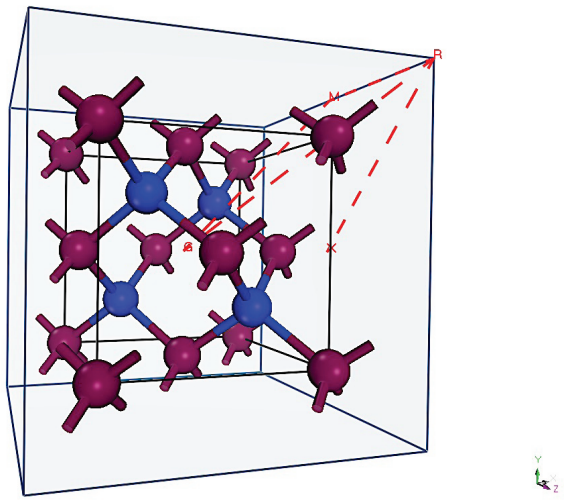

Figure 2.2 Zincblende AlN. (Nitrogen colored blue) High symmetry points in the first irreducible Brillouin zone are labeled in orange.

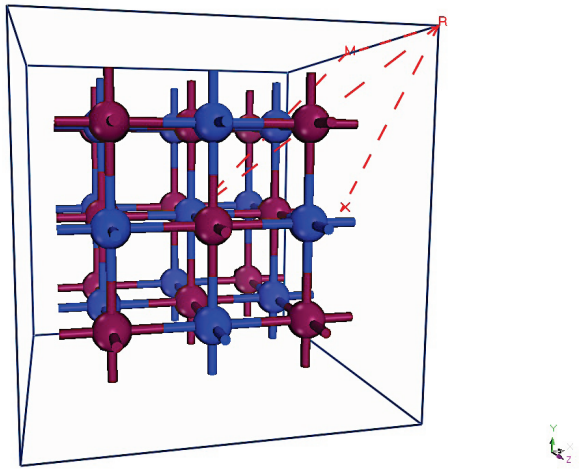

Figure 2.3 Rocksalt structure. Nitrogen colored blue. High symmetry points in the first irreducible Brillouin Zone are labeled in orange.

Although the relationship between binary nitride crystal structure and its properties have been of interest for various decades[207-209], some of their precise crystalline arrangements have been discovered until recently, for instance, the Zr_3N_4 the phase of

zirconium nitride was observed experimentally since 1993, but its point group symmetry was recognized until 1996[210]. The most stable crystalline array for AlN as well as some other aluminum carbonitrides[211] under ambient conditions is the wurzite or B4 structure (Figure 2.1). The tetrahedraly coordinated Al atom is surrounded by four holes in a regular N tetrahedron in the wurzite structure. Pyroelectric effect due to polarization along the c axis has been suggested[212]. Its structural parameter "u" deviates from the ideal 1.633 ratio with a value of 1.603 due to its particular geometric arrengement[213]. The presence of oxygen traces is also known to influence the hexagonal structure. Some reports have suggested the presence of a meta-stable zincblende phase[214] (B3), shown in Figure 2.2. A pressure induced phase transition to rocksalt structure (B1) (see: Figure 2.3) is also reported, varying from less than fourteen[214] to ca. 20 GPa[215]. In the case of ZrN, the most stable phase is the cubic[216] (B1) "rocksalt" structure while the orthorhombic Zr_3N_4 phase, obtained from stoichiometric ammonolysis with metallic sodium[209], presents Pmna point group symmetry[210]. The equilibrium values for both binary compounds at different phases are summarized in Table 2.1.

Table 2.1 Equilibrium values, binary metal nitrides.

	Volume	Energy	"a"	Erel (%)
AlN (B1)	16.44	-14.4859	4.036	2.504
AlN (B3)	20.96	-14.9071	4.377	1.363
AlN (B4)	42.50	-15.2265	3.131	0.621
ZrN (B1)	24.48	-20.2631	4.609	-0.014

Extensive parameters are normalized per formula unit. As mentioned earlier, PAW PBE type of potentials (hard version) was used to represent each ion in the calculation.

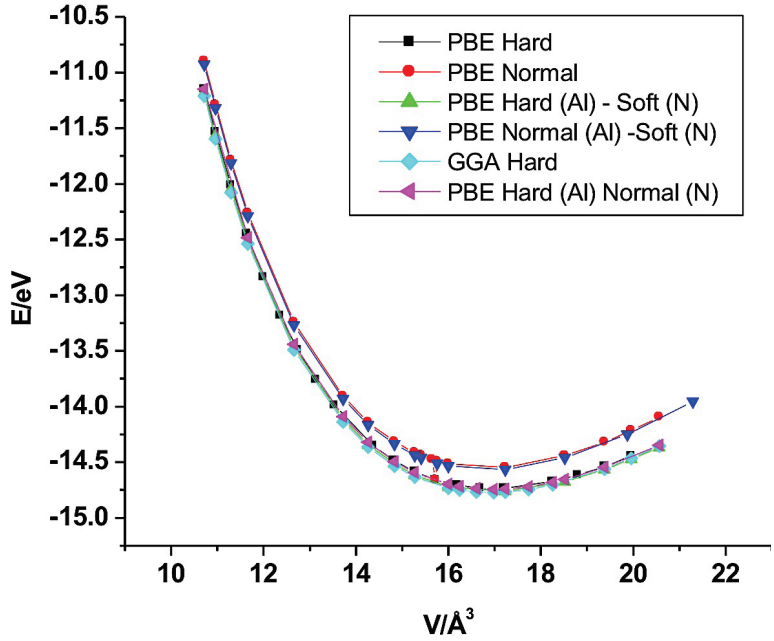

Figure 2.4 Results from different pseudopotentials. AlN, B1.

The crystal's cell parameters as well as atom positions were relaxed in order to reach the convergence criteria. An interesting observation points to the fact that for the most ionic B1 structure, the lattice constant value was better predicted when normal and soft versions (for Al and N respectively) of pseudopotentials were employed (see: Figure 2.4). In the case of AlN wurzite (B4) structure, the relative error between experimental unit cell volume[217] (41.71 $Å^3$) and the predicted volume is less than 2% $Å^3$.

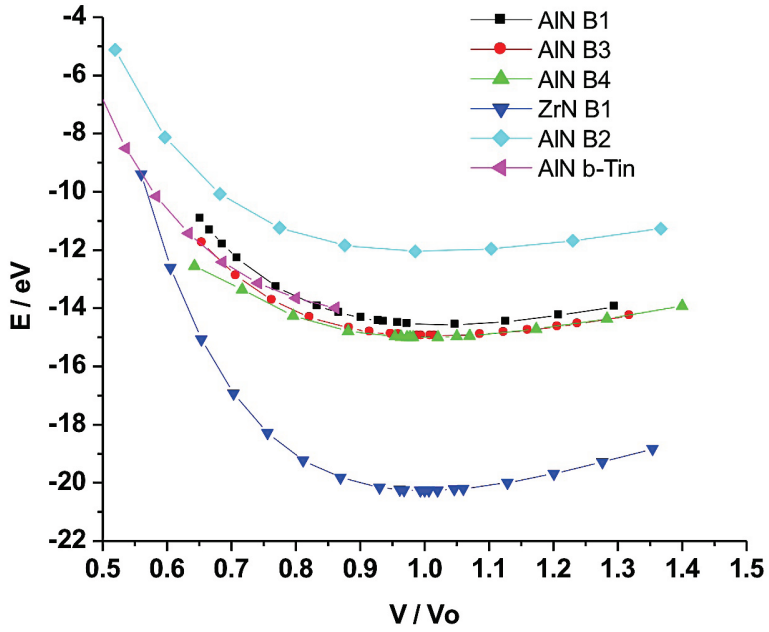

Figure 2.5 Energy as a function of volume. Nitride systems.

Starting from the primitive experimental crystal unit cell, the energy vs. volume at zero Kelvin behavior is calculated (Figure 2.5).

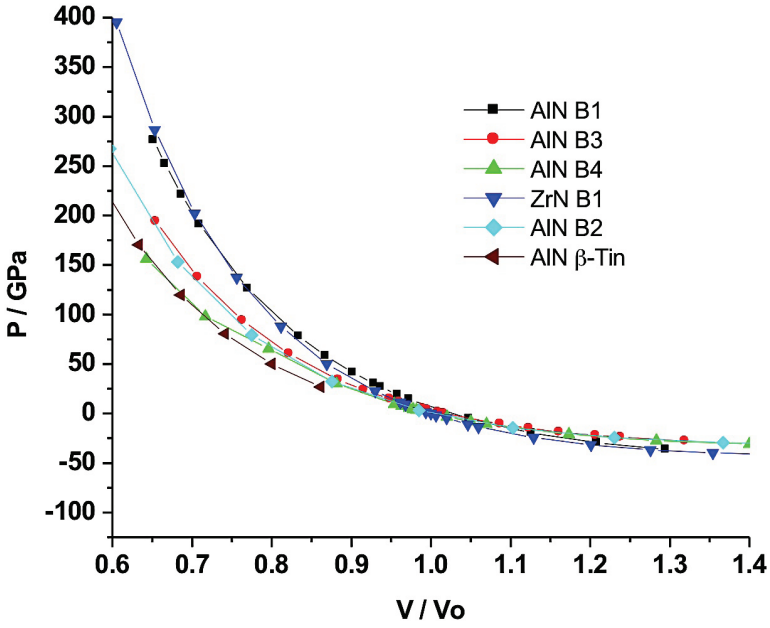

Figure 2.6 P vs V behavior of some nitride systems.

The abscissa is normalized with the volume required to get the structure in a state of zero stress, which is obtained by fitting data points to a 3rd order polynomial. The same pressure–volume characteristics of these systems can be observed in Figure 2.6. For the AlN wurzite structure, the ratio of lattice vectors C/A ratio changes as a function of the system's pressure, the trend towards lower C/A values at higher pressures can be seen in Figure 2.7. This is the first time that to our knowledge, a variable C/A calculation is included in a study that aims at representing the system at different pressures.

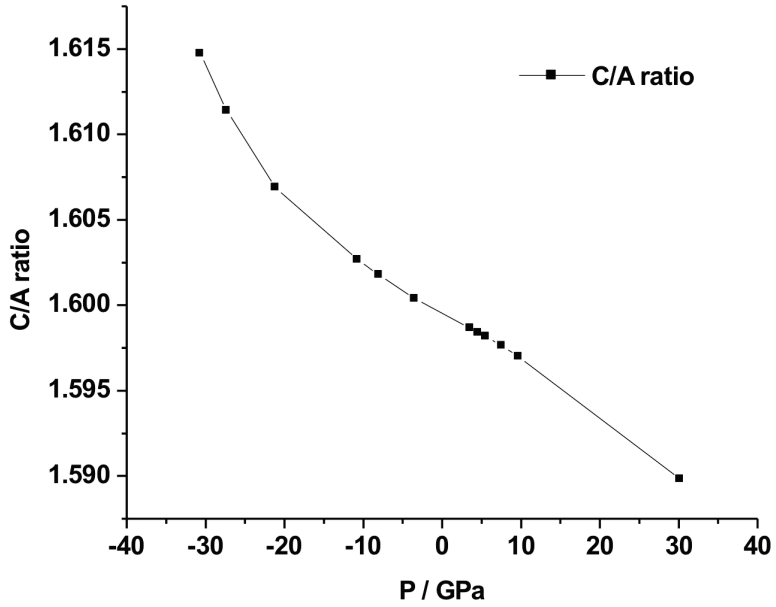

Figure 2.7 C/A ratio as a function of pressure for AlN (B4).

The corresponding enthalpy (H = U + PV) curves are presented for the experimentally observed AlN as well as for the ZrN B1 phase in the following Figures (Fig. 2.8, Fig. 2.9).

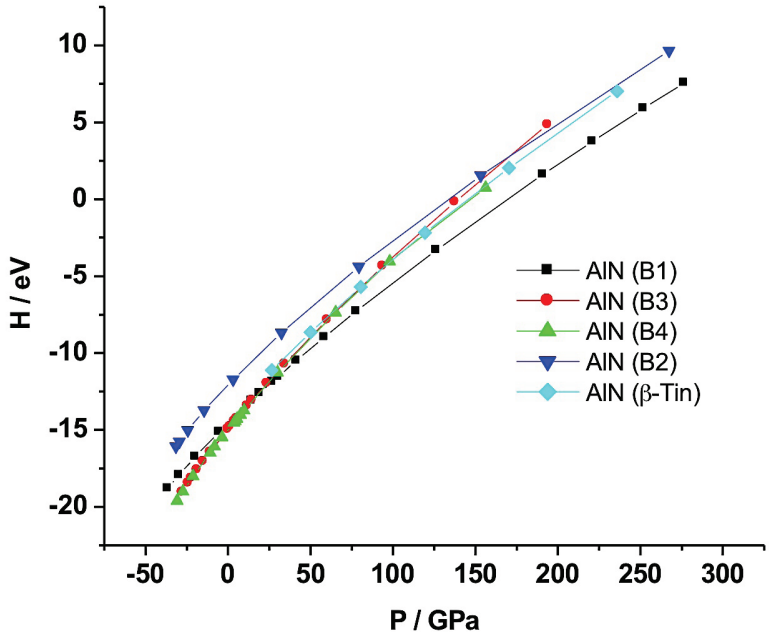

Figure 2.8 H vs. P for AlN system.

A phase transition occurs whenever there's a change the phase following a lowest enthalpy value for the H vs. P curve. We can observe (Fig. 2.8) that the metastable zincblende (B3) phase lies almost parallel atop of the enthalpy line for the wurzite structure. This might explain why this phase although observed, it is difficult to obtain experimentally. The corresponding B4 to B1 transition occurs ca. 17.8 GPa, (Fig. 2.9) this value compares with the experimental (17.02) one with good agreement (4.5%).

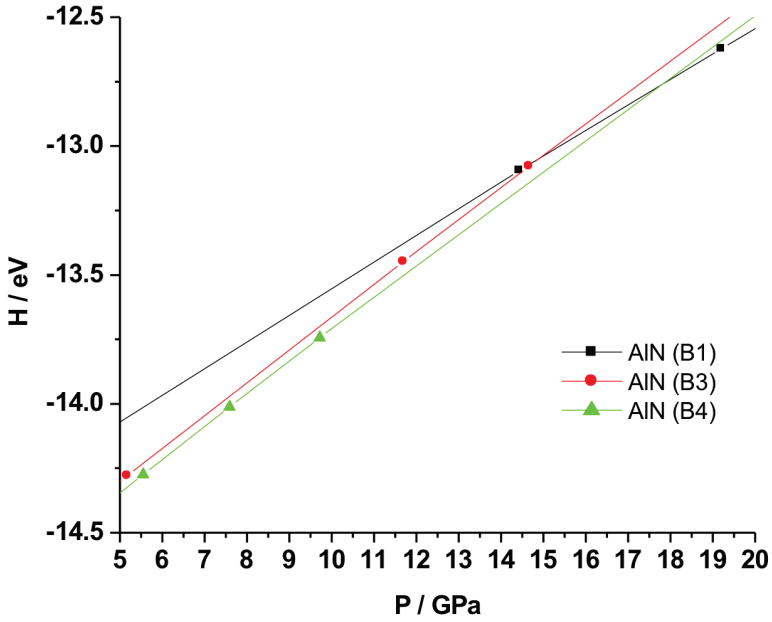

Figure 2.9 H vs V for B4 to B1 transition.

Previous reports have indicated a phase transition at ca. 16.6 GPa, although these results utilized the GGA exchange correlation functional, at experimental C/A (1.6) ration. More recently, PAW-PBE hard potentials have shown to represent better bulk properties of some simple (2 atom) crystals.

For the case of ZrN, the EOS was calculated for the B1, B2 and B3 structures; this can be observed in Figure 2.9. A comparison of the enthalpies of the systems as function of pressure can be found in Figure 2.10. The ability to correctly predict high-pressure behavior of chemically simple metal nitride systems (AlN in this case) can support exploration of the high-pressure behavior of other more complex systems, where the interaction between a metal and nitrogen its further expanded with the interaction of elements of more complex chemistry, like carbon.

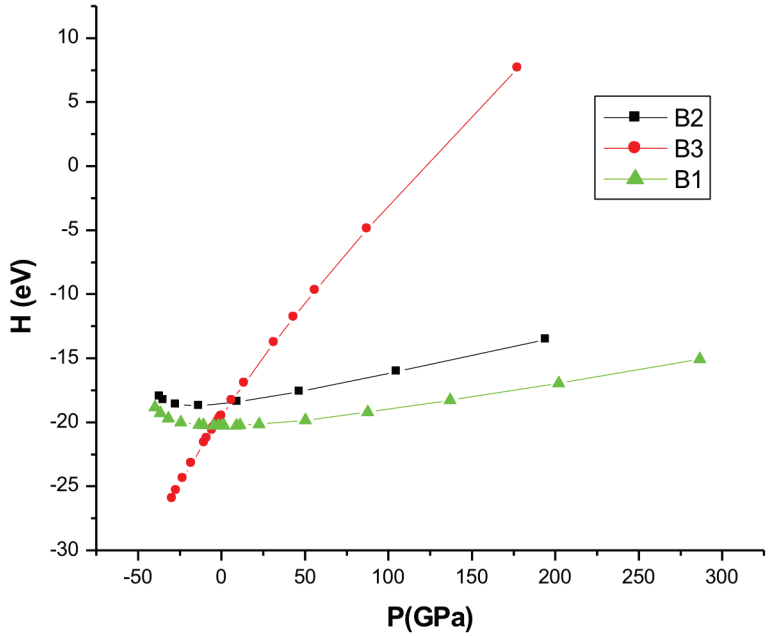

Figure 2.10 Enthalpy versus pressure for ZrN.

From the earlier calculations using orthogonalized linear combination of atomic orbitals[217] approximation (OLCAO) a reported band gap of 4.64 eV was reported. In its wurzite structure, AlN has an energy band gap of ca. 4.02 eV. Figure 2.11 shows the Density of states for the different AlN phases, as calculated with VASP, first a self-consistent single point energy calculation is performed, wit a small number of K-points (usually a 6X6X6 grid). The charge on each ion obtained from this SFC calculation is then used to obtain the DOS. We can see clearly occupation numbers in three regions of the energy axis. In particular, for the B4 structure, which is semiconductor, we see a gap between the vale of 0 eV and 4 eV. For the case of the B4 structure, there is four atoms per unit cell, hence two red lines and two blue lines are shown.

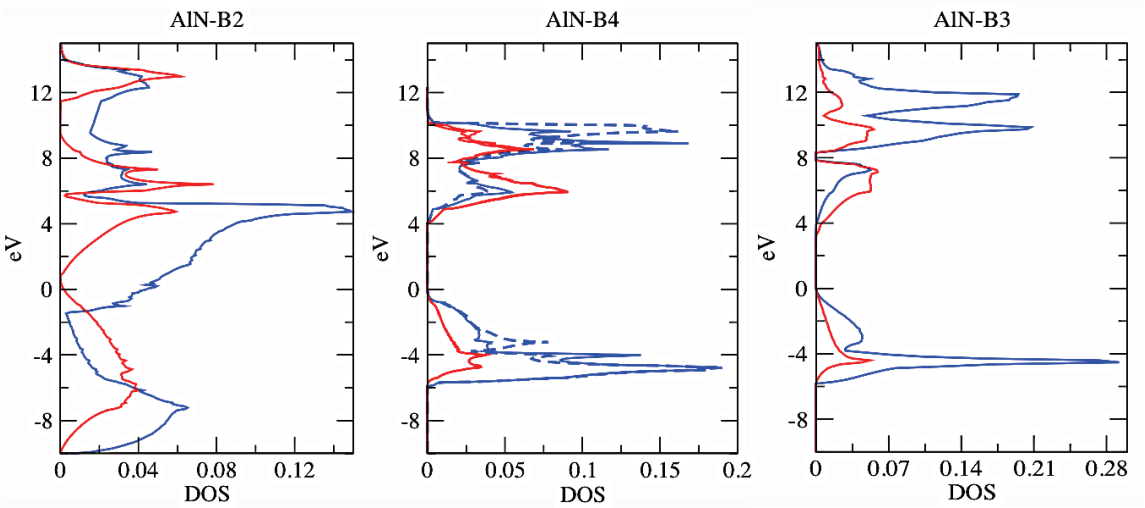

Figure 2.11 DOS for AlN. From left to right, density of States for the AlN systems B2, B4 and B3. States from Al: blue, N: red.

Electronic density occupation can be more clearly understood if we observe the corresponding density of states for each atom There is clearly a higher occupation number on the N above the normalized Fermi level, at 0 eV, while Al plays a more important role in the region close to the valence energy values (below 0 eV). We have previously shown the inverse space constructs of the primitive cells of the nitride systems. This will help us to understand the band structure diagram found in Figure 2.12. We see a band ordering along vectors of different momentum, which follow directions in inverse space. To understand this diagram, we can refer to the molecular orbital diagram of AlN (Figure 2.12). The occupation energies correspond to the 1σ, $1\sigma^*$ and 1π the later corresponding to the highest occupied molecular orbital (HOMO), the lowest energy unoccupied molecular orbital can be ascribed to the 2σ MO. There is clearly 4 occupied bands (one two of them degenerate) and 4 unoccupied bands, this is further

confirmed in the following band structure representation along high symmetry k-points (Figure 2.12) which corresponds to the AlN (B1) crystalline structure.

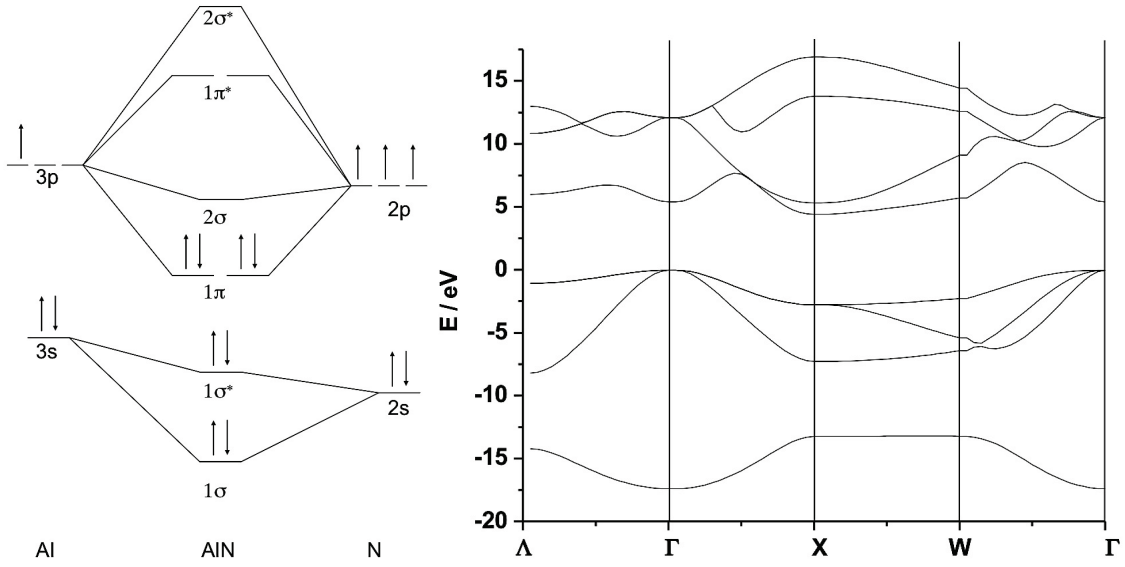

Figure 2.12 MO diagram for AlN(left). Band structure calculation for AlN , right**.**

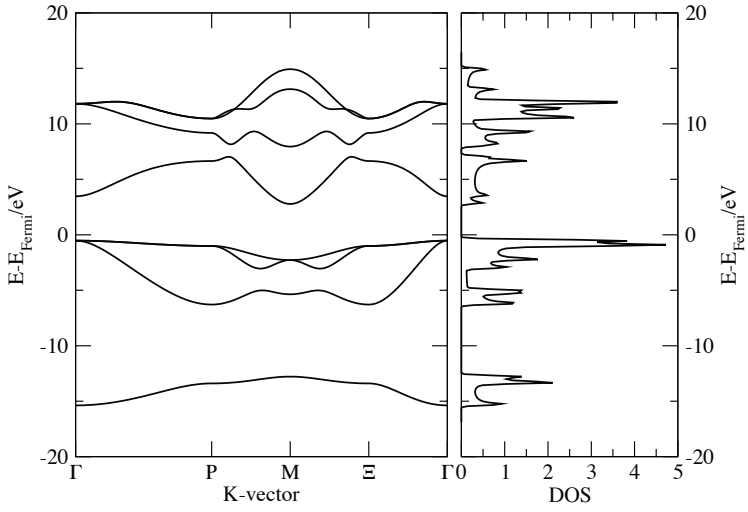

Figure 2.13 Band structure of AlN (B3). Total density of states (right**).**

For AlN, the electronic band structures of the other symmetries are shown in Figures 2.13, 2.14 and 2.15

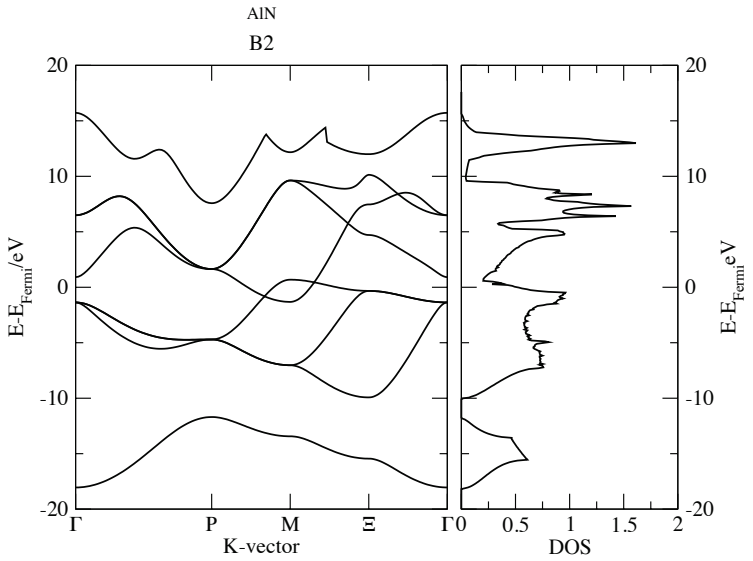

Figure 2.14 Band structure of AlN (B2). Total density of states (right**).**

From the energy gaps between zero eV and the next occupation energy level, we can deduce if the system behaves as a semiconductor, as in the B4 and B3 structures, or if they behave as in a quasi-metallic state (B2).

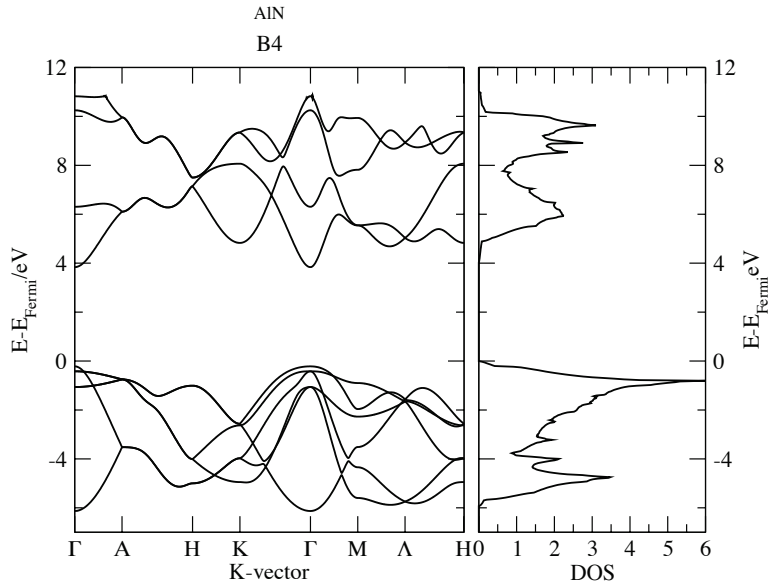

Figure 2.15 Band structure of AlN (B4). Total density of states, right**.**

With this understanding, we can proceed to study a more complex case, a metal-organic molecule, with interesting optical properties.

Viologen

Since their early development[218-222], the use of zirconium phosphate as structural component[223,224] has shown promising uses for their particular properties. Their application has ranged from components for sensor, or indicators[225-231].The present structure under study uses as linking pillar a form of a 4,4-bypiridinum salt, or viologen.

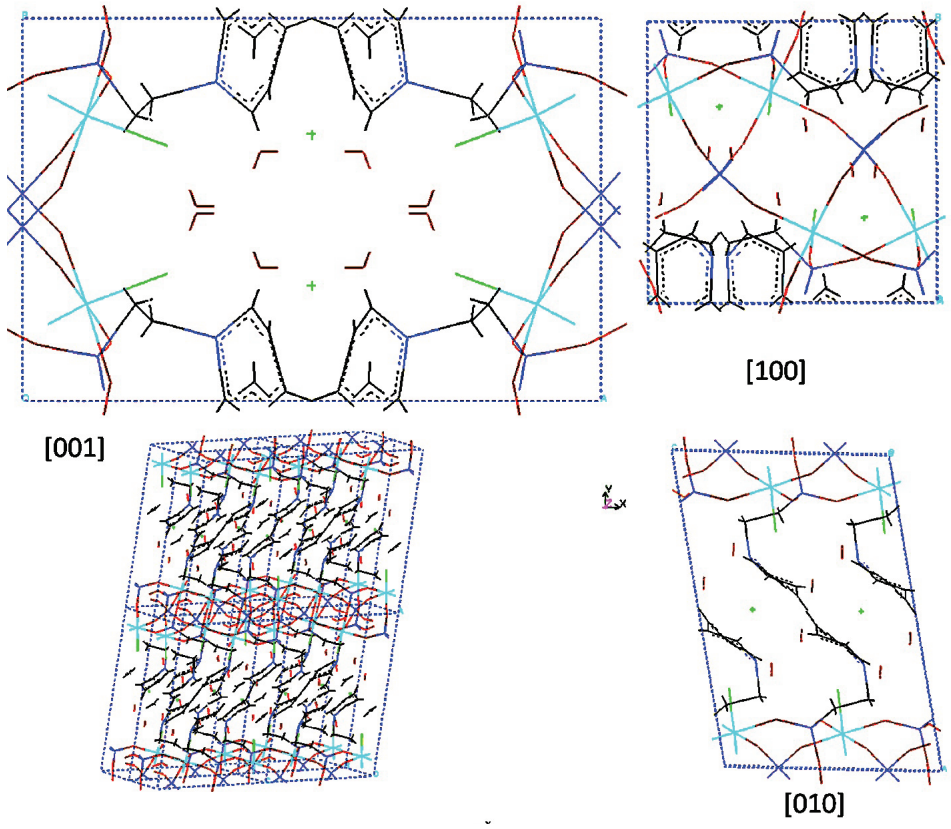

Figure 2.16 Structure of Zirconium Phosphate-viologen. Views along the three axial directions. Image of a 2x2x1 supercell, viologen seen as linker for the phosphate layers.

Depending on the substituent group to which it is bonded[231], the radical cation formed will have a blue-violet color at different values of pH. Charge transfer and properties in this environment is of interest[232,233]. In particular, inclusion of metals or other catalysts could pose a promising material for hydrogen generation[223,234,235].

Since the positions of hydrogen could not be resolved[236,237], we have placed hydrogen atoms in symmetric positions in order to complete stoichiometric composition (Figure 2.16). Structures with sodium and potassium as charge balancing counter ions have been prepared with the same initial reported structural frame. PAW potentials were

used. For all cases, the PBE exchange correlation method has been employed. In the case of Zr, the highest number of 12 electrons has been explicitly included in the calculations. The remaining inner shells have been taken care of by the use of pseudo potential.

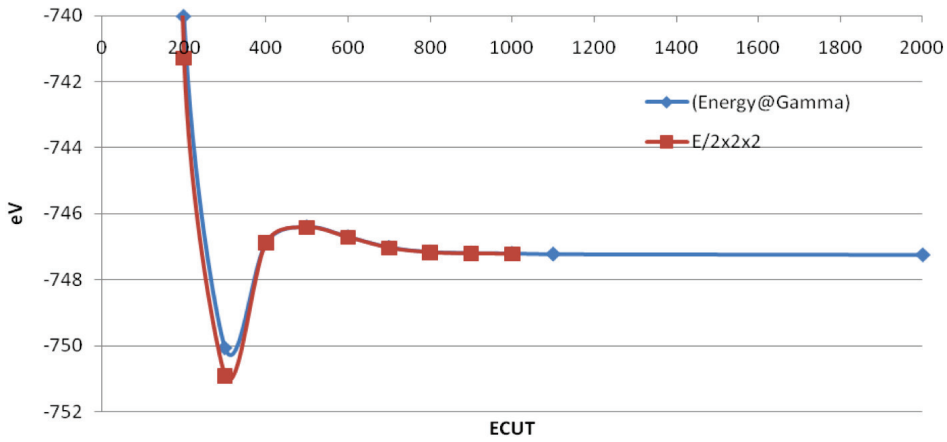

Figure 2.17 Convergence with respect to energy-cutoff (eV).

A 2x Monkhorst Pack integration scheme for the reciprocal space is used for a convergence of less than 1 meV in total energy with a 550 eV plane wave cutoff (Figure 2.17). The model contains a total of 124 atoms, and 468 electrons.

The optimized hydrogen caped structure, at the reported volume (no cell parameter relaxation) is shown in Figure 2.18. Two cells aligned along [010] are joined together to show the linking viologen molecule, which can be seen crossing the boundaries. The molecule binds to a Phosphate unit near the mid part of a [100] plane. Zirconium has distorted octahedral coordination bonding to four oxygen atoms and a fluorine atom. There are 8 water molecules per unit cell, fluorine act as a counter ion close to the aromatic ring of the viologen linking molecule. In the optimized structure, we see that water molecules surround the F ions such that coordination is observed, from the most

negative value of the isosurface of the total equilibrium charge. The charge surrounding the aromatic ring is also observed. The total energy in this case is -790.929199 eV.

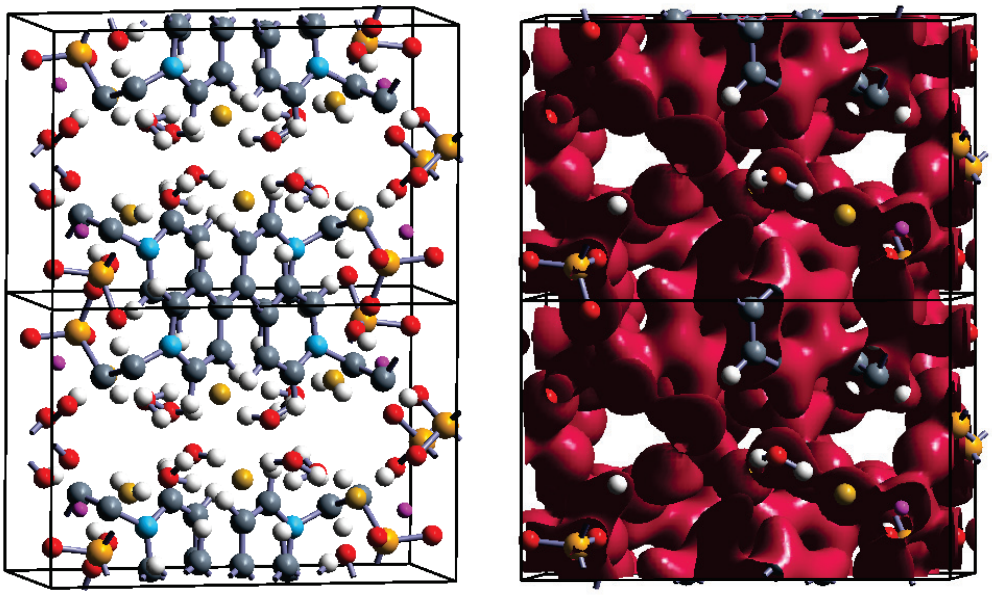

Figure 2.18 Two unit cells of ZrPh-viologen. The super cell is standing on the X-Z plane. Na-navy blue, Oxygen-red, Carbon-grey, Nitrogen-light blue, Zr-pink, F-ochre (close to corners), P-orange (close to the edges of cell). Negative charge iso-surface (right).

The reciprocal space Brillouin Zone is constructed following high symmetry points. Division is along 7 K-Points. The band structure is calculated by converging the total energy and charge with a dense integration mesh (5x), using the tetrahedron method. The converged charge is used then, to do a non-self-consistent calculation in which each k-point is treated individually. Due to the limitations in available physical memory, the path along each point is integrated with 20 divisions. Unless otherwise stated, the K-points used correspond to the coordinates in reciprocal space of a simple monoclinic system; Z,G,Y,A,B,D,E and C (Figure 2.19).

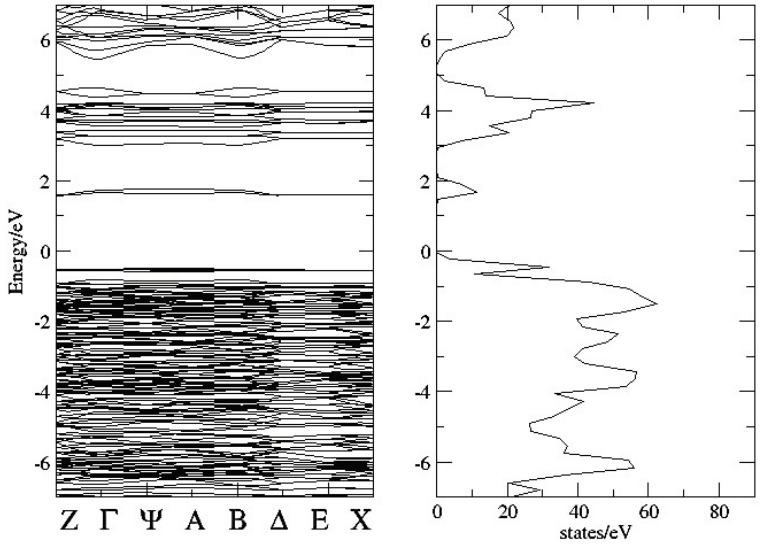

Figure 2.19 Band structure of ZrPh viologen. Hydrogen terminated system.

The indirect energy band gap, as measured from the DOS plot is of 1.24 eV. At Gamma point, this is, in the long wave range limit, the gap is 2.17 eV.

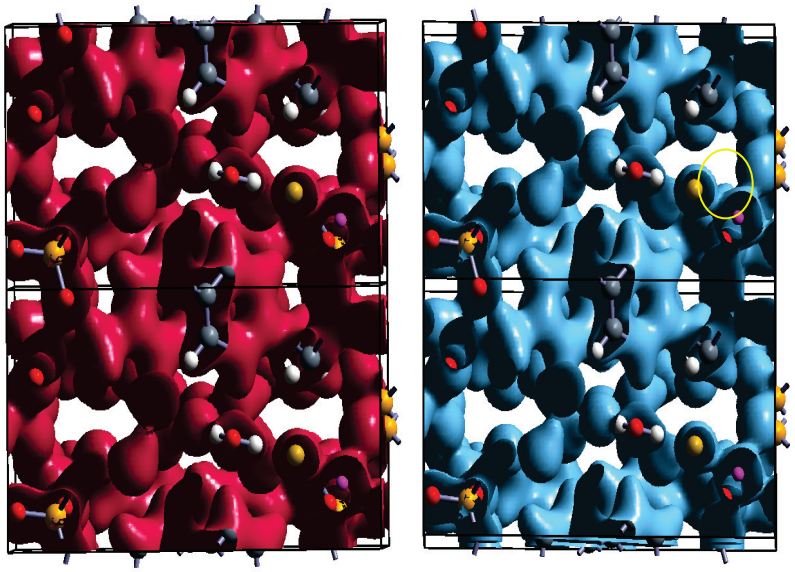

Figure 2.20 Minimum energy charge density, left. Average charge density isosurface, after lattice parameter optimization.

Upon relaxation of the lattice parameters, at a fixed experimental volume, the ‘a’ lattice parameter increased to 14.778 Å from the experimental value of 13.59Å, the B/A ratio change to 0.533 from 0.65 and C/A change from 0.68 to 0.533. As seen by the charge contour surfaces in the cell-optimized structure, there is an increased bonding from the closely coordinated F atom to the Metallic center (Figure 2.20). The distance from the F atom to the neighboring hydrogen in the atomic optimization is 1.51Å, while in the cell optimized structure this distance is increase to 1.72Å. The Fermi energy is now at 0.66 eV.

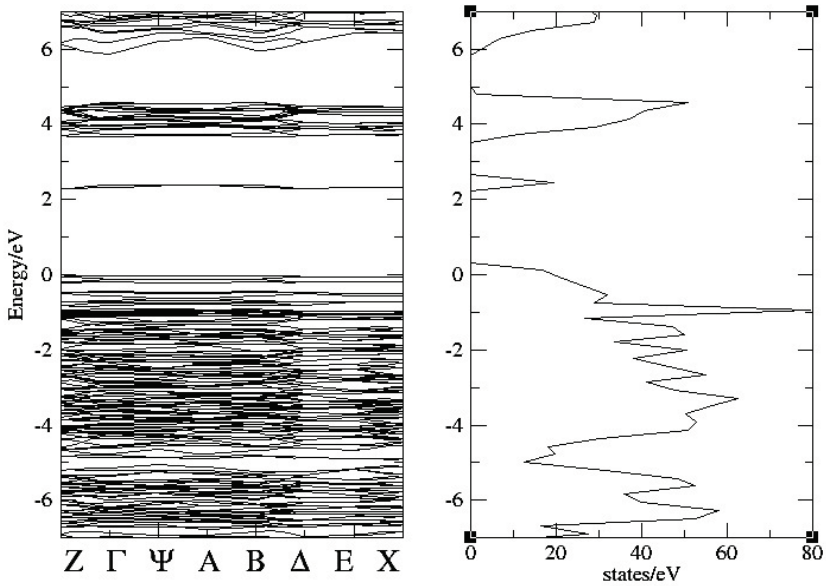

Figure 2.21 Electronic structure of ZrPh-viologen. DOS, right. Optimized unit cell.

We can see that the energy gap is ca. 2.22 eV, and there is an increase in the states near the Fermi energy, ca. -0.7 eV (Figure 2.21). Even though there is an off-shift in the DOS profile, the change in its features can qualitatively describe a change in the bonding structure of the system. A larger magnitude of the forces occurs in the system with

Sodium and Potassium atoms, causing a rupture in the aromatic system containing nitrogen. The structure was far different from the initial structure, and the system was reported to be semi-metallic. No aromatic ring was observed after the optimization. To circumvent this issue, we establish two different procedures; both of the methodologies seemed to preserve the aromatic backbone of the structure. First we proceeded to consecutively optimize the volume and cell parameters, in this way the initial step involved only arriving at the required volume for the current initial configuration. The second step involved fixing the carbons in the aromatic rings present to maintain their aromaticity, while relaxing the rest of the degrees of freedom. The EOS for some nitride compounds was presented (AlN, ZrN). The calculations performed with PAW-PBE potentials showed good agreement (less than 5%) with the experimental measured values. For the first time a study that includes the optimized C/A ratio for the wurzite structure at different volume is presented. The DOS calculation for AlN (B1) structure, showed the strongly ionic character of this system, with the larger electronic density over the more electronegative (N) ion. Also by applying a volume conserving strain, the first set of mechanical properties for these bimetallic cubic compounds is presented. Electronic structure of the different AlN phases is presented. Further electronic calculation for the ZrN system is required. Further calculations should include values for the elastic constant of the presented phases. Electronic band-gap calculations have been performed for ZrPh-viologen. We have found a band gap at Gamma of ca. 2.23 eV for relaxed atomic and lattice degrees of freedom. In account of the well-known underestimation of the band-gap value within DFT methods, an experimental value of

2.8 to 3.1 could be expected. The corresponding wavelength ca. 400 nm corresponds well with the observed color of the linking molecule. The effect of the chosen counter-cation has dramatic effect on the electronic structure of ZrPh-viologen.

Secondary Energetic Materials

With the information at hand, we can no proceed for calculations on EM. With the use of the self-consistent field Kohn-Sham orbitals, we are able to scrutinize the electronic structure of some commonly used energetic materials. If we take into account the electrostatic interactions amongst neighboring molecules within the same crystalline unit cell, we can see that non-bonding interactions become obvious. In Figure 2.22, we see the unit cell of fox-7, with the electrostatic potential map projected into the interior surfaces of the unit cell. The orbitals centered on each atom are colored gray.

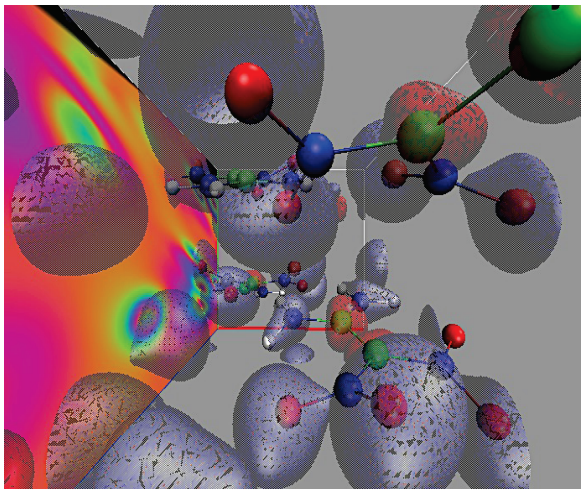

Figure 2.22 Electrostatic potential map, Fox-7.

The electrostatic potential of nitromethane, as visualized through the slice of a plane, can be shown on the next (Figure 2.23) Figure.

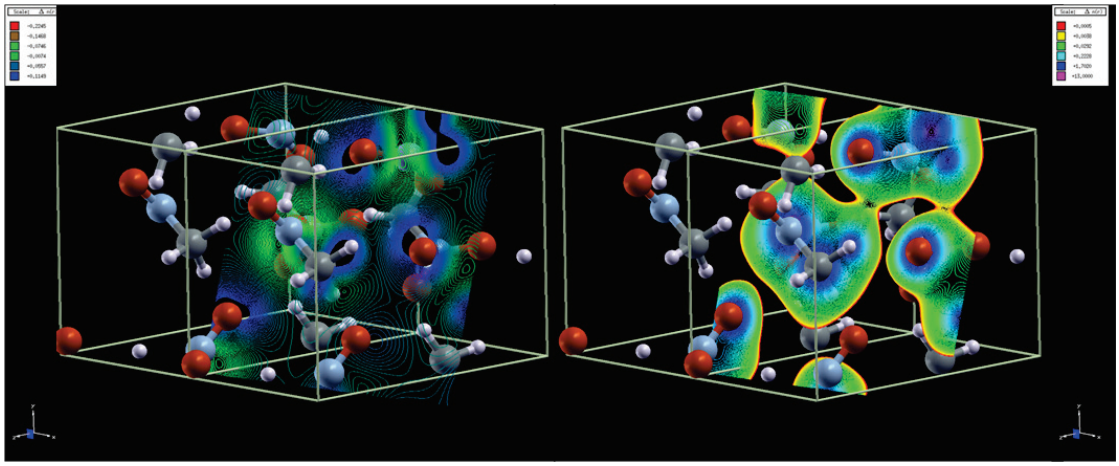

Figure 2.23 Electrostatic potential map, NM. Values after SCF shown left, difference with respect to the atomic overlap value, right.

It is customary to observe the final charge density or electrostatic potential, but the difference between this last value and the density matrix as obtained from the superposition of atomic orbitals. In this way differences of the chemical environment of the molecules can be observed. For nitromethane, we see that there is still a region of electrostatic potential from one of the terminal methyl hydrogen and the neighboring nitro- oxygen from another nitromethane molecule. We have used a logarithmic scale to exaggerate the difference in the potential values.

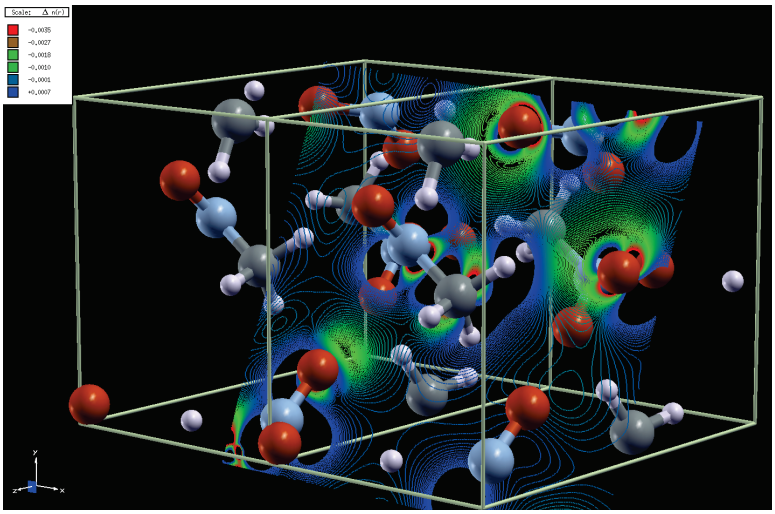

Figure 2.24 Difference map, NM.

If we let the molecular fragments stand apart a large distance, while keeping the translational symmetry of the system intact, and perform a SCF calculation, we can obtain the electron density of the non-interacting system. In Figure 2.24 we can observe the difference density map between the electron density of this non-interacting density, and charge density obtained from the optimized structure of nitromethane. In this case we have used a linear scale, since the difference in the two charge densities is expected to be small. As we shall see in the discussion, the degree and number of hydrogen bonds can play also a role in the stability and sensitivity of each type of system.

The integration path over the reciprocal space is done along high symmetry directions; this can be observed in Figure 2.25. The electronic band-structure, obtained at a 8x symmetric k-space Monkhorst-Pack integration grid, can be shown in the following Figure 2.26, we have included the Fermi energy level as a dotted line, to facilitate comparison of the energy levels with the atom projected density of states.

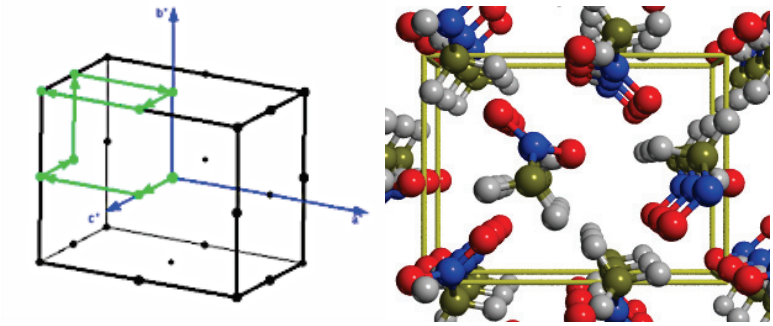

Figure 2.25 Reciprocal space construct for NM, left. NM unit cell, view from the [100] plane (right).

The calculated energy band gap at Gamma is 1.898e-1 A.U. or 5.24 eV, a large gap characteristic of an insulating crystal. There is a larger amount of population coming from oxygen states near the valence band, while the first conduction or exited state band is mostly populated from oxygen and nitrogen states. This indicates the activity the nitrogen and oxygen atoms, which for nitromethane arises only from the nitro groups, in the valence and conduction states.

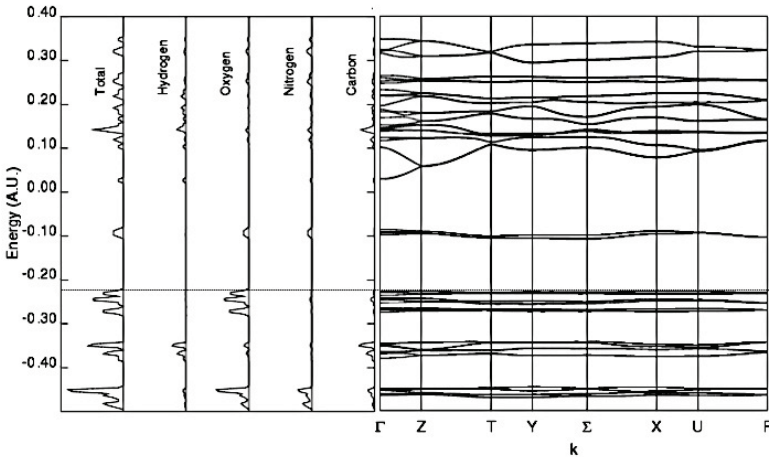

Figure 2.26 DOS (left) and band structure of NM (right).

For PETN, can observe the band structure and DOS in Figure 2.27.

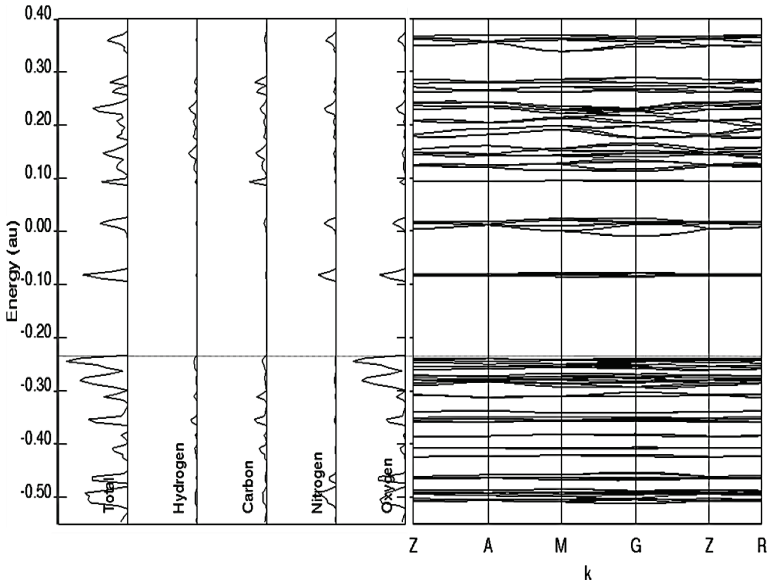

Figure 2.27 DOS (left) and band structure of PETN (right).

For the here studied system, there is a characteristic band gap. As opposed to the previously studied metal nitride systems, assignment of each band to particular molecular orbital states is not as straightforward.

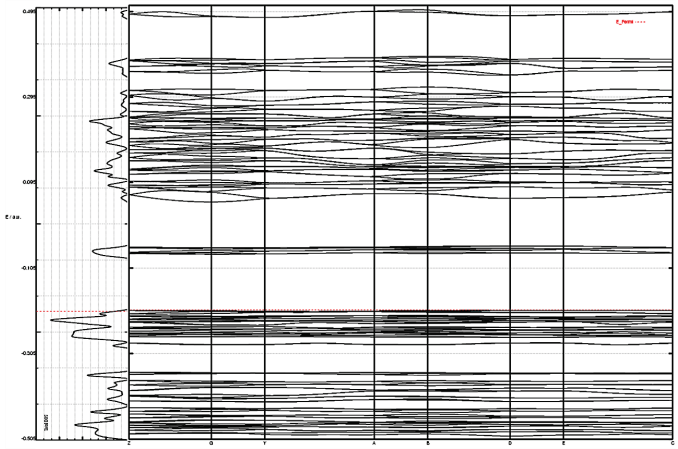

Figure 2.28 DOS (left) and band structure of β-BHMX (right).

For β-HMX we also see a band gap larger than 5 eV, and low-lying conduction state above the Fermi level (Figure 2.28). We will see in forthcoming chapters the effects of particular shears or strains and their effects in the electronic structures of molecular crystals; EM in particular. Since the variation of the mechanical properties is of relevance in these strained states, we shall proceed now with the study of the calculation of elastic properties, from DFT methods.

CHAPTER III

FINITE ELASTICITY

Issues in the Use of Ab Initio Methods

Since the introduction of the first stress-strain calculations[238,239] within the first principles density functional theory[97,240] (DFT), there has been an increase in the number of publications reporting the calculations of elastic constants[181,187,200,241-253]. However, with this increase, a large variation in the reported value of elastic constants arises. The variation in reported values can be attributed to convergence in the calculation parameters, the type of strains employed to obtain an elastic response, or the thermodynamic reference state used. Most reported values are obtained from "Cauchy" type or "engineering" strains ("E"), which fail to account for a tensor description of the crystal's deformation, thus the chance of finding a discrepancy due to the type of elastic strain approximation cannot be ruled out.

Neutron diffraction studies of the elastic constants of binary nitrides have been reported by Chen et al.[249]. Trends in elasticity for nitride systems were analysed by comparison with neutron diffraction data by Cohen[181] and Wu[254]. The mechanical properties for the semiconductor e-FeSi are of relevance in understanding the Earth's core and mantle[255]. This system has a small band gap[256 257]; close to 50 meV. Recently, its bulk modulus has been measured[258-261] while high temperature elastic constant of ranging values have been reported[256,262]. Although other DFT calculations on e-FeSi have been reported[261], there are yet any results on its low temperature elastic properties,

beyond interpolation. To the best of our knowledge, third order elastic constants values have yet to be reported for HfN and ε-FeSi.

In the following, we would like to convey the implications of the type of deformation applied to obtain an elastic response, and study the effect of specific computation parameters that can influence calculated elasticity values. The set of systems under study is composed by; hafnium nitride (HfN), aluminium (Al) and ferrosilicon (ε-FeSi). HfN is a binary nitride with large stiffness caused by its covalent interactions, while Al is a softer metal. Both materials are of use by the microelectronic industry[184] and as structural materials, amongst other applications. Representation of the atom's positions in the cubic HfN and Al systems is determined by the symmetry of the crystalline unit cell. As means of comparison, ε-FeSi is included[263], for whose internal degrees of freedom are not set by symmetry. Its use in our study will allow for a comparison of the previous systems with those in which change in the internal structural is expected.

To account for the factors essential in the calculation of elastic constants, we will start by discussing the importance of a proper representation of the electronic structure. An effect of convergence in the calculation parameters (e.g.; kinetic energy cut-off and size of the integration mesh) is then analysed. The elastic stiffness constants represent the change in energy required for an infinitesimal change in strain, from the initial or 'zero stress' reference state; 'V_0'. The effect of the zero stress structure and validity of this reference when applying a strain will be further explored. Parameters like strain amplitude are also systematically studied. Comparison of values obtained by volume

conserving strains and linear response theory will follow. We then compare the type of strain used when calculating higher order (3rd) elastic constants. Particle displacement in a strained solid can expressed as the difference of its final to initial position[264]:

$$u_i = x_i - X_i, i = 1..3 \quad (2)$$

The material displacement gradient can be expressed as a difference in coordinates:

$$\frac{\partial u_i}{\partial X_j} = \frac{\partial x_i}{\partial X_j} - \delta_{ij} \quad (3)$$

We can express the finite strain tensor or *Lagrangian* in terms of the displacement gradients[265]:

$$L_{ij} = \frac{1}{2}\left(\frac{\partial u_k}{\partial X_j}\frac{\partial u_k}{\partial X_i} + \frac{\partial u_j}{\partial X_i} + \frac{\partial u_i}{\partial X_j}\right) \quad (4)$$

For an infinitesimal strain, in which the displacement gradient is smaller than one, we can neglect the first term inside the parentheses. For a rigid displacement, the lagrangian strain is then:

$$\epsilon_{ij} = \frac{1}{2}\left(\frac{\partial u_j}{\partial X_i} + \frac{\partial u_i}{\partial X_j}\right) \quad (5)$$

In relationship to a periodic solid, in which its basis vectors can be expressed in terms of an h matrix, an applied strain will transform the original matrix h_0 as:

$$h = (1+\epsilon)h_0 \quad (6)$$

And its transpose:

$$h^T = {h_0}^T(1+\epsilon)^T \quad (7)$$

The product of '$h^T h$' is know as 'G' matrix[266]

$$G = h^T h \tag{8}$$

In terms of the unstrained matrix, this expression can be expanded as:

$$G = {h_0}^T(1 + 2 \in + \in^2)h_0 \tag{9}$$

Since ϵ<<1, we disregard the squared term, and obtain:

$$G = {h_0}^T(1 + 2 \in)h_0 \tag{10}$$

The use of G, facilitates obtaining the value of the cell parameters, for systems of arbitrary symmetry. We have omitted the tensor notation, to emphasize the difference between strained and unstrained states. The convention of centering of the 'h' matrix is of relevance here. If choosing an upper diagonal 'h' matrix, with the C lattice vector aligned with the Z axis, B in the y-z plane and A arbitrary, the lower diagonal elements will be zeros. For the rest of the components, we can solve a system of linear algebraic equations, in terms of the elements of 'G', to find each component of 'h'. For example, for a non volume conserving strain, the first element in fractional coordinates of 'h' to find C11, will be, within the linear engineering or 'Cauchy'approximation; 1+e. By applying small strains to the crystallographic unit cell, a change from the original, optimized cell energy is obtained. This difference in energy can then be compared in terms of polynomial expansion, to the strain energy;

$$E_0 - E = V_o C_i \eta_j + \frac{V_o}{2} C_{ij} \eta_i \eta_j + \ldots \tag{11}$$

Where V_o is the initial unstrained cell volume, and η_i and η_j are the applied elastic strains. Since we are interested only on the symmetric part of the strain tensor, we can

employ the contracted or "Voigt" notation. C_{ij} are then the second order elastic constants.

$$C_{ij} = \frac{1}{V_0}\frac{\partial^2 E}{\partial e_i \partial e_j} \qquad (12)$$

If we realize that the initial reference cell is subject to no additional forces, this is, in its "zero stress" state, the first term in the expansions is ignored. Comparison to a second or higher order polynomial fit will enable us to obtain the corresponding second order elastic constants. The resulting second and higher order elastic constants can in turn be related to the anisotropic response of the crystal to deformation. By choosing of the right set of parameters[267], we can find the appropriate second order elastic constantsThe set of lattice vectors that are used to describe the crystal system at it reference state are called 'h_0'. They transform to the state 'h' upon deformation. The use of 'engineering' type of strains, in which 'h' is obtained by approximating it to $h_{0*}(1+e)$, has been used by most authors [242-247,254,268-270], to predict the elastic properties of crystals of high symmetry. In this case 'e' represents the deformation to which we will compare the initial stress and energy of the system. The systematic study of the elastic properties of the aforementioned systems is initially achieved by performing full relaxation of the forces for a set of 23 strained states. Volume conserving and non-volume conserving strains, with engineering 'E' type of approach are used. We have labelled the applied strains as 'dx' where x is a numeral. Due to the symmetry of this tensor, the number of independent elastic stiffness constants is reduced to 21. Lattice symmetry causes the number of independent, non-zero elastic constants can be further reduced; three, for the

case of cubic systems. In our consideration for the Lagrangian strain, we can neglect the higher order elements of the strain tensor. Notice that this should not be de case when studying bodies subjected to non-linear loading. Furthermore, 'h_0' can then be transformed to the strained state either in a finite elastic deformation, or 'G', or as in a Cauchy-type linear elastic strain approximation, or 'E'. We have used both non-volume conserving and volume conserving strains. Taking as example strain 'd_1', and using vector notation:

$$d1 = \left[\lambda, -\lambda, \frac{\lambda^2}{1-\lambda^2}, 0, 0, 0\right] \tag{13}$$

Here,'l' refers to the applied strain percent variation; 0.005 to 0.08 in our case.

The relevance of volume conserving strain lies in the fact that the energy expression is changed as;

$$\frac{(\Phi - \Phi_0)}{V_0} = (C_{11} - C_{12})\lambda^2 + O[\lambda^4] \tag{14}$$

Thus the error in the calculated elastic constant error in the calculated elastic constant is in the order of $0[d]^4$. In addition, we will used another strain commonly used[271,272], we call it 'd_{1B}' strain;

$$d1 - B = \left[\lambda, \lambda, \frac{1}{(1+\lambda)^2} - 1, 0, 0, 0\right] \tag{15}$$

And the energy expression will be changed to:

$$\Phi = \Phi_0 + 3V(C_{11} - C_{12})\lambda^2 + O(\lambda^3) \tag{16}$$

For volume conserving "engineering" strains, we have chosen the following strain matrices, centered on the 'a' axis:

$$\begin{bmatrix} \lambda & 0 & 0 \\ 0 & -\lambda & 0 \\ 0 & 0 & -\frac{\lambda^2}{\lambda^2-1} \end{bmatrix} \begin{bmatrix} \lambda & 0 & 0 \\ 0 & \lambda & 0 \\ 0 & 0 & \frac{1}{(1+\lambda)^2}-1 \end{bmatrix} \begin{bmatrix} 0 & \lambda & 0 \\ \lambda & 0 & 0 \\ 0 & 0 & \frac{\lambda^2}{(1-\lambda)^2} \end{bmatrix}$$

‘d1’ ‘d1-B’ ‘Monoclinic’

The finite elastic strains obtained from ‘G’ are then:

$$\begin{bmatrix} \sqrt{2\lambda+1} & 0 & 0 \\ 0 & \sqrt{-2\lambda+1} & 0 \\ 0 & 0 & \sqrt{-\frac{2\lambda^2}{\lambda^2-1}+1} \end{bmatrix} \begin{bmatrix} \sqrt{2\lambda+1} & 0 & 0 \\ 0 & \sqrt{2\lambda+1} & 0 \\ 0 & 0 & \sqrt{-\frac{2\lambda^2}{\lambda^2-1}+1} \end{bmatrix} \begin{bmatrix} \sqrt{1-4\lambda^2} & 2\lambda & 0 \\ 0 & 1 & 0 \\ 0 & 0 & \sqrt{-\frac{2\lambda^2}{\lambda^2-1}+1} \end{bmatrix}$$

From which the first upper two strains are used to obtain C_{11}-C_{12} (‘d1’and‘$d1_B$’). The last one can be used to extract C_{44}. The determinant of the strained ‘h’ matrix is equal to the initial volume of the system. If volume conservation is not required, the corresponding ‘E’ and ‘G’ strains used are;

$$\begin{bmatrix} \lambda & 0 & 0 \\ 0 & 0 & 0 \\ 0 & 0 & 0 \end{bmatrix} \begin{bmatrix} \lambda & 0 & 0 \\ 0 & \lambda & 0 \\ 0 & 0 & 0 \end{bmatrix} \begin{bmatrix} 0 & 0 & 0 \\ 0 & 0 & \lambda \\ 0 & \lambda & 0 \end{bmatrix}$$

‘d1’ ‘d2’ ‘d3’

And;

$$\begin{bmatrix} \sqrt{2\lambda+1} & 0 & 0 \\ 0 & 1 & 0 \\ 0 & 0 & 1 \end{bmatrix} \begin{bmatrix} \sqrt{2\lambda+1} & 0 & 0 \\ 0 & \sqrt{2\lambda+1} & 0 \\ 0 & 0 & 1 \end{bmatrix} \begin{bmatrix} 1 & 0 & 0 \\ 0 & \sqrt{1-4\lambda^2} & 0 \\ 0 & 2\lambda & 1 \end{bmatrix}$$

Since the cell choosing is non-unique, we can set the requirement for a symmetric cell centering, and solve the corresponding set of linear equations. The resulting strain matrices are:

$$\begin{bmatrix} \frac{1}{2}\sqrt{1+2\lambda}+\frac{1}{2}\sqrt{1-2\lambda} & \frac{1}{2}\sqrt{1+2\lambda}-\frac{1}{2}\sqrt{1-2\lambda} & 0 \\ \frac{1}{2}\sqrt{1+2\lambda}-\frac{1}{2}\sqrt{1-2\lambda} & \frac{1}{2}\sqrt{1+2\lambda}+\frac{1}{2}\sqrt{1-2\lambda} & 0 \\ 0 & 0 & \sqrt{\frac{2\lambda^2}{1-\lambda^2}+1} \end{bmatrix}$$

$$\begin{bmatrix} 1 & 0 & 0 \\ 0 & \frac{1}{2}\sqrt{1+2\lambda}+\frac{1}{2}\sqrt{1-2\lambda} & \frac{1}{2}\sqrt{1+2\lambda}-\frac{1}{2}\sqrt{1-2\lambda} \\ 0 & \frac{1}{2}\sqrt{1+2\lambda}-\frac{1}{2}\sqrt{1-2\lambda} & \frac{1}{2}\sqrt{1+2\lambda}+\frac{1}{2}\sqrt{1-2\lambda} \end{bmatrix}$$

‘d4’

For the non-volume conserving and volume conserving cases, correspondingly. In order to compare the effect of higher order contributions to the strain energy, we have adopted some of the commonly used strains.

$$\begin{bmatrix} \lambda & 0 & 0 \\ 0 & 0 & \lambda \\ 0 & \lambda & 0 \end{bmatrix} \begin{bmatrix} \lambda & 0 & \lambda \\ 0 & 0 & 0 \\ \lambda & 0 & 0 \end{bmatrix} \begin{bmatrix} \lambda & 0 & 0 \\ 0 & \lambda & 0 \\ 0 & 0 & \lambda \end{bmatrix} \begin{bmatrix} 0 & \lambda & \lambda \\ \lambda & 0 & \lambda \\ \lambda & \lambda & 0 \end{bmatrix}$$

‘d_2,’ ‘d_3,’ ‘d_4,’ ‘d_5,’

The corresponding energy change can be found in the following table:

Strain	Energy Change
“d_1”	$V_o(\frac{C_{111}}{6})$
“d_2”	$V_o(\frac{C_{111}}{3}+C_{112})$
“d_2,”	$V_o(\frac{C_{111}}{6}+2C_{114})$
“d_3,”	$V_o(\frac{C_{111}}{6}+2C_{155})$
“d_4,”	$V_o(\frac{C_{111}}{2}+3C_{112}+C_{123})$
“d_5,”	$V_o(C_{456})$

Below the value of one percent strain, we chose 1/6, 1/3 and 1/5 percent strain values. Above this, the strain changes sequentially from 1%, 2% up to an 8% maximum

strain value. Including the zero stress energy of the system ("E_0"), both tensile and compressive strain energy values are obtained. The result is seven data points obtained at half percent strain, 9 data points at one percent, and so on. In the maximum strain value, a total of 23 data points are used to obtain a second order polynomial fit, equated to the strain energy expression. From this polynomial, the value of the second order elastic constant is obtained. The effect of the number of strain steps and range of the strain applied is studied later. For this case, equidistant strain steps are taken up to the indicated value.

Total energy calculations have been performed with both the linear density approximation[273] (LDA)and the Perdew-Burke-Ernzerhof formalism[98] of the general gradient correction (GGA) approximation. The projector-augmented wave method[206] (PAW) as implemented in the Vienna *ab initio* package[100-102] is employed. Unless otherwise stated, convergence of the self-consistent electronic cycle is set to $1x10^{-6}$ eV. Plane wave kinetic energy limit and sampling scheme are used for a convergence in the total energy better than 2.7 meV/atom. Values particular for each system are discussed in detail in the coming discussion. Notice the fact that any change in energy smaller than the total energy convergence will be unreliable. Thus, the parameter becomes the "resolution" or an effective limit for measuring changes in strain energy. Linear response theory calculations have been performed both with PAW lists and with the Abinit package[274-277] adopting the use of FHI Pseudo potentials[278].

Electronic Structure Description

The effect of accurate electronic structure representation in metals and its effects in elasticity have been acknowledged from earlier calculations[279-284]. Since account for partial occupancies near the Fermi level is required for metals, different smearing methods have been proposed[285-288]. The addition of an external 'entropy' term is required if accurate forces and structure optimization are to be obtained. However, the value of this term should be small enough, so its contribution is no larger than the resolution of the calculation. With this in mind, and for the case of the metallic systems; HfN and Al, we have use the Methfessel-Paxton scheme[287], and the equivalent methodology of Mazari[288] with the largest energy smearing factor possible, while keeping the energy contribution below the energy resolution of the calculation. For the semiconductor FeSi, we have used the linear tetrahedron method, with Blöchl corrections[289].

Since the exact form of exchange functional is unknown, differences in calculations performed within DFT methods could be expected[289,290]. Two of the most common formulations used are the LDA and GGA type of approximations. There have been reports on the elasticity of transition metals that show comparable values of for calculations performed with both LDA and GGA methods[291]. We would like to explore the difference in the calculations of elastic constants, arising from the use of the aforementioned functionals. We find this difference to be as small as 4%, as in the case of shear constants of HfN, or as large as 18% as in C_{11} for HfN as well (Figure 3.1). A difference of 10% is common for the other constants and systems. Results from Non-Volume conserving 'E' strains.

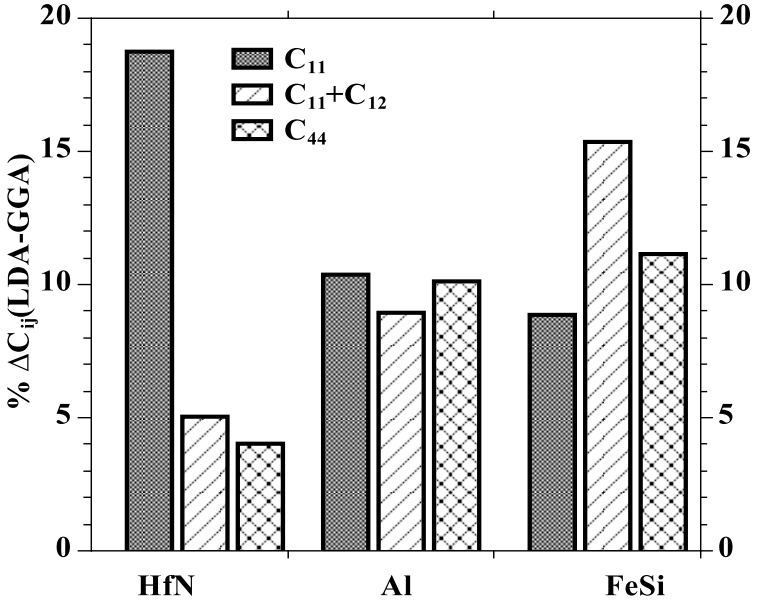

Figure 3.1 Effect of the type of exchange-functional. Difference of "GGA/PBE" calculated values from those obtained through "LDA"

Therefore a systematic difference from LDA and PBE results can be expected, and should be noticed when comparing with experimental values. Since the aim of the study is not to find the best-suited exchange functional, but to systematically resolve the effect of type of strain and computation parameters in a consistent manner, we will try to compare elastic coefficient obtained within the PBE form of GGA functional, unless otherwise stated.

We have used a Gamma point centered symmetric grid, which allows to reduce the number of inverse space sampling mesh points (k-points) by taking into account the symmetry of the system. This is opposed to non-symmetric grids, which requires shifting schemes or a larger density for a convergence in the mechanical properties[247]. In spite of

a convergence to values smaller than 3 meV/atom were obtained with the k-points and energy cut-off parameters, a test of convergence on the mechanical properties is performed (see: Figure 3.2). We observe that for Al, there is a dramatic effect due to the number of k-points, as seen from the value of C_{11}. It is worthy to notice the fast convergence for FeSi, in which the ionic positions are relaxed to minimize the forces. Increase in the K-mesh resulted in an adjustment to a convergence value of 0.70 meV for HfN and 1.63 meV for Al.

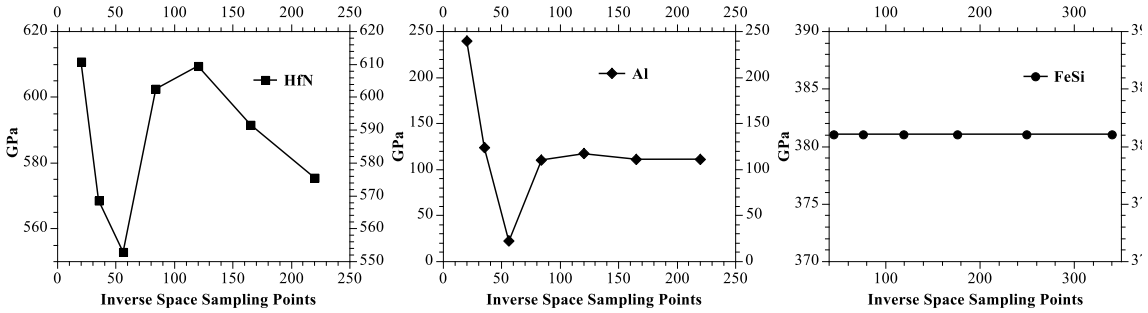

Figure 3.2 Convergence with respect to number of symmetric sampling points. Inverse space, 'C_{11}' results. A value of d=3% strain was used for all cases.

In an addition to the behaviour observed with respect to the density of the inverse space grid, FeSi was found to converge very rapidly with respect to basis set size. This is observed from a kinetic energy cut-off study performed on each system (Figure 3.3). The rest of the studied materials also showed les sensitivity for the limit of the plane wave energy cut-off, as compared to the k-points size.

Reference State

If the crystal structure is not far from the equilibrium volume state, the condition of zero stress can be achieved by relaxing the structure. For this calculation, sources of

error will indeed arise from the energy resolution itself. Another route is to find 'V_0' with the use of an equation of state (EOS), from where thermodynamic information like bulk modulus (B_0) and the first derivative of the bulk modulus (B'_0) can be obtained. We have used the Vinet, the third order Birch-Murnaghan[292] (BM), and the four parameter equation of state[293] (4-param).

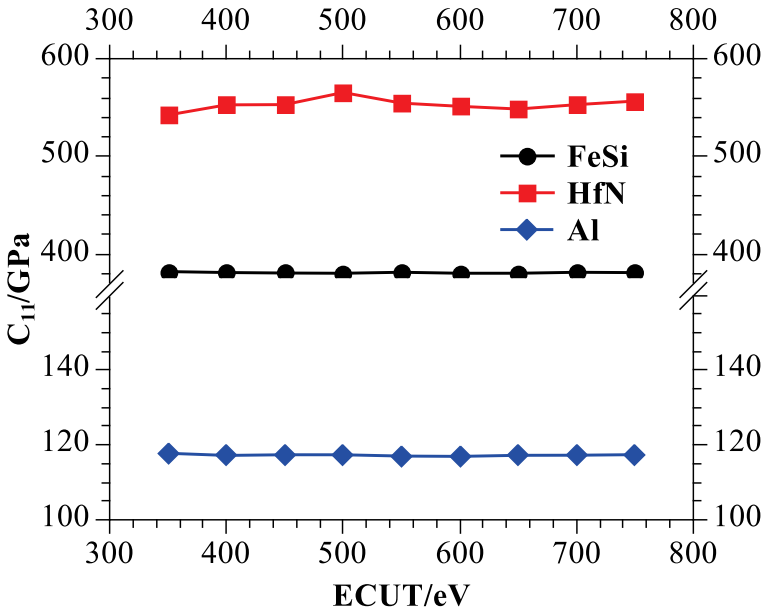

Figure 3.3 Convergence with respect to the maximum plane wave energy cut-off.

For the system: FeSi 'B_0' is ca. 20 GPa smaller as predicted from BM than for Vinet's EOS. For HfN, and Al, the value of 'V_o' predicted from structural relaxation and both EOS are comparably close, whilst B_o is smaller by 65 and 57 GPa, correspondingly, as compared to Vinet's. This accounts for data obtained at both tensile and compressed states (see: supplemental). For further reference, we use the values corresponding to BM. The use of linear response theory to obtain the second order elastic constants can now be

used as means of comparison. In view of a reference state for which forces or stresses on the system should account to zero, we evaluate now the validity of this assumption, by an analysis of the linear term of the strain energy expansion.

Linear Term

The first term in the strain energy expansion refers to the forces acting upon the system. Comparing a polynomial in which the linear term is used explicitly, versus not having an explicit force term, we see that second order contribution to the strain energy, does not change. Nonetheless, a second order fit is worst, as measured from a smaller coefficient of determination (R^2) when the effect of external stress is neglected. To further observe the effect on the full set of applied strain values, we regard changes in the hydrostatic stresses, as seen in Figure 3.4.

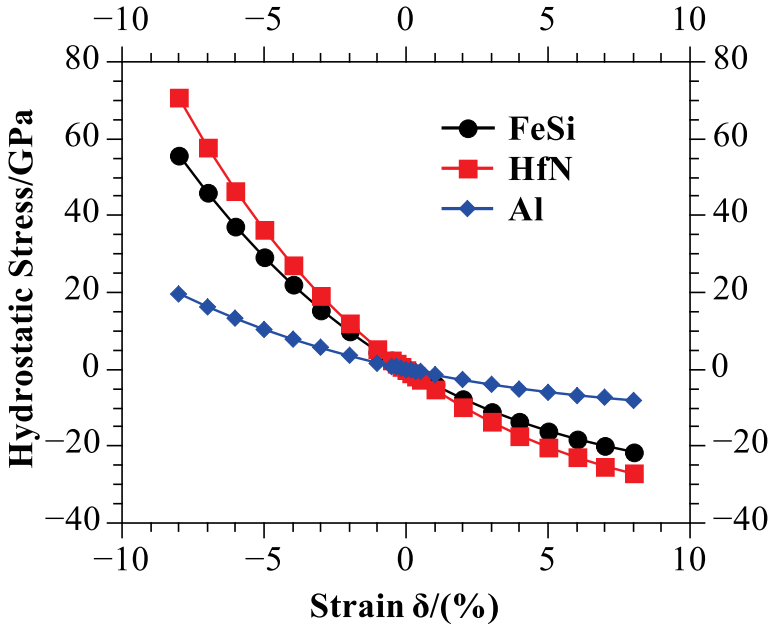

Figure 3.4 Change in the hydrostatic stress. For the strain 'E' non-volume conserving, 'd2', from which $C_{11}+C_{12}$ is obtained.

The zero stress of the 'reference state' required in a second order description of the elastic response is easily attained. The effect is more dramatic for the stiffer system; HfN. The rapid increase in hydrostatic pressure suggests strain amplitudes that cannot be set arbitrarily large. We now proceed to study the effect of the value of the strain amplitudes.

Strain Amplitude

To find energy differences large enough to be reliable is pursued by finding a strain energy difference larger than the minimum measurable due to convergence parameters. The value, from here on referred as 'd_{min}' is shown in Table 3.1, reported in meV. Sequential non-volume conserving 'G' strains corresponding to 'C_{11}' and 'C_{44}' are used for illustration. The minimum strain amplitude value it is driven by the parameters and potentials used, and the strain energy difference. This refers to the smallest strain studied, for which there is a change in energy 'DE' larger than the measurable limit from convergence in total energy. Therefore is system dependent.

Table 3.1 Minimum strain sizes. Labelled here: 'd_{min}', for the studied systems.

C_{11}	Al	HfN	FeSi
δ_{min}	2%	0.33%	0.33%
ΔE	11.4	1.72	1.11

C_{44}	Al	HfN	FeSi
δ_{min}	2%	0.33%	0.33%
ΔE	9.64	1.74	186
Limit	1.63	0.7	0.25

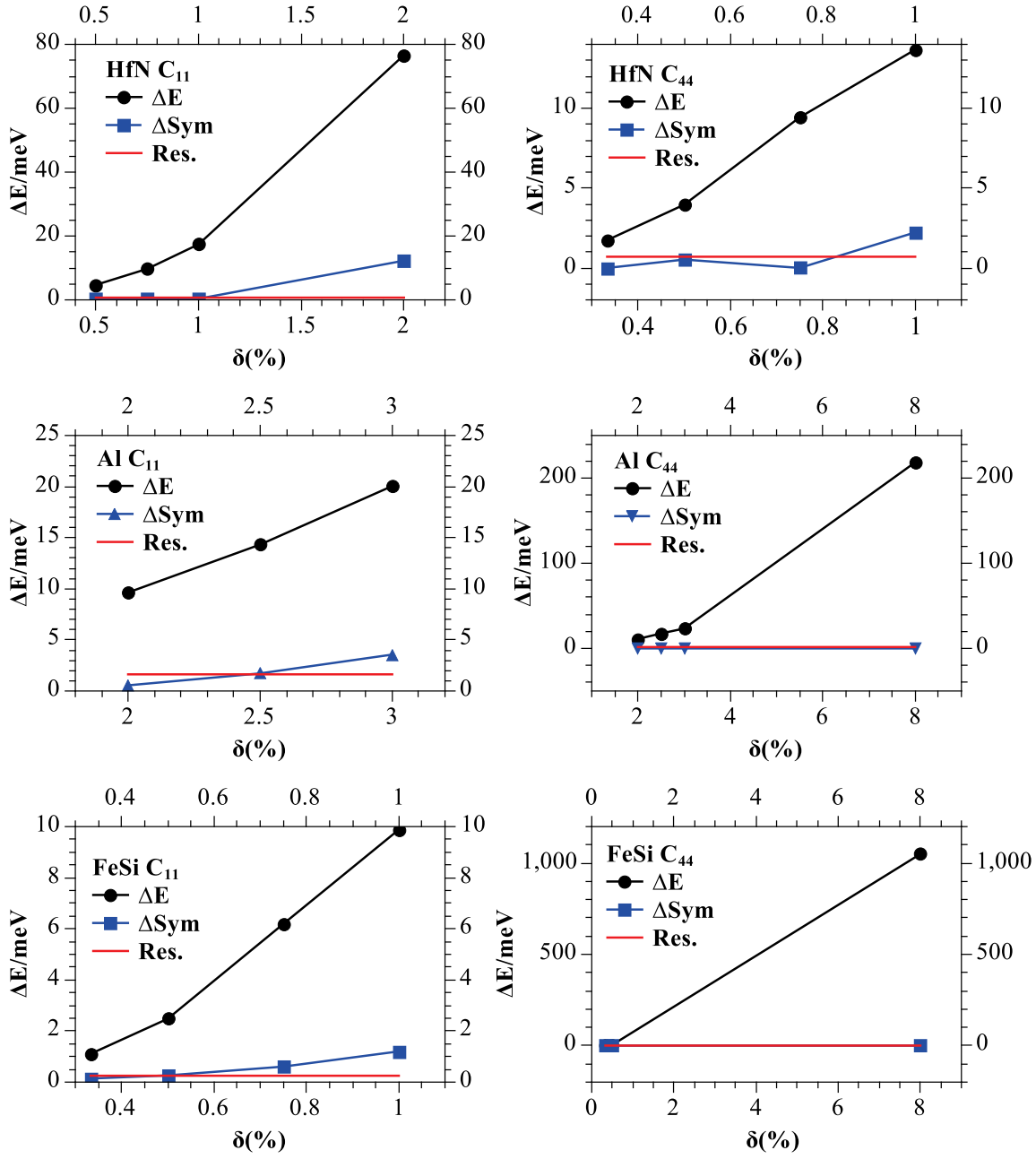

Figure 3.5 Change in the strain energy, (ΔE). Comparison to the change between tensile and compressive strain for each applied strain;"ΔSym". Deformations corresponding to the calculation of C_{11} and C_{44} Results observed for HfN (Top), Al (middle row) and FeSi (bottom).Strain energy: "Res.".

The contribution from higher order terms can be an additional limiting factor in determining the maximum strain amplitude, for measurements related to second order

elasticity. In a perfectly elastic deformation, the strain energy difference is symmetric. Thus, any applied deformation should be small enough to avoid non-elastic behavior, or contributions from third and higher order terms. The difference in energy versus the maximum strain ‘d’, as well as the difference from tensile to compressive energy, is shown in Figure 3.5. Results from Non-volume conserving, finite elastic, ‘G’ type of strains shown; δ(%) refers to the maximum strain amplitude. The resolution in strain energy change from convergence parameters can be seen as a baseline in each Figure, labelled: “Res.”. An increase in non-linear contributions, from the change of the term ‘ΔSym’ is observed. The calculation can be assumed accurate with an energy difference at least an order of magnitude larger than the measurable value. The value of ‘ΔSym’ is no longer negligible if compares to the order of magnitude of the resolution. The ‘optimum’ strain amplitude is thus found where the difference in energy is at least twice the accuracy error, and the third order contribution is kept small. Attention should be now drawn to the use of strain step values with an energy difference below this limit value. This could be expected for HfN, which requires large energy for a displacement to occur.

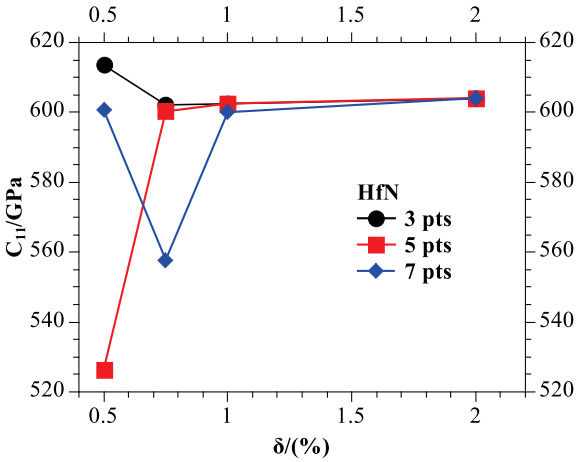

Figure 3.6 Variation of 'C_{11}' with respect to maximum strain. System: HfN. Equidistant step size, maximum amplitude indicated as δ(%). Each line represents calculations resulting from different number of strain energy data points, including; five (5pts), seven (7 pts.) and nine data points (9 pts.).

In Figure 3.6, we find that use of sequential strain steps with use of strain energy differences close to the zero value will include noise data. Each line represents calculations with different number of strain energy data points used, including; five data points (5 pts.), seven data points (7 pts.) and nine data points (9 pts.). Below the strain value of 1%, we see an erratic behaviour caused by noise in the data. In the case of 5 pts and 7 pts data below accuracy is found for the strain values of 0.75% and 0.5%. Finite elastic, 'G', non-volume conserving type of strain applied. Comparing the use of an equidistant strain step scheme, in which the maximum strain amplitude is divided into an arbitrary number of segments, we find easier to remove the noise data points, and avoid its use in the calculation of the elastic constants.

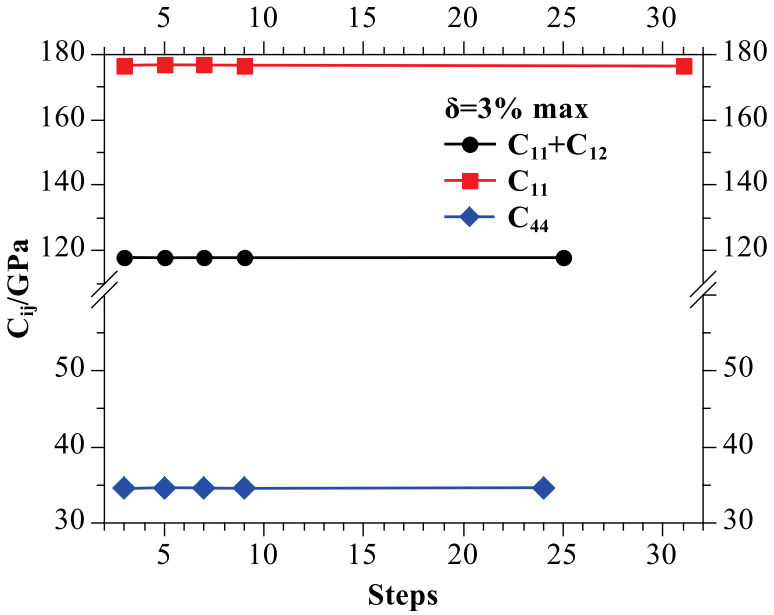

Figure 3.7 Effect of number of strain steps. Aluminium, with a maximum of 3% strain amplitude reported here.

To test the sensitivity of the calculated of the elastic constants to the number of strain steps, we have removed data with an energy change smaller than twice the accuracy of the calculation. It can be observed that the value of the calculated constant is almost invariant with respect to the number of data points employed. Even with the denser data sampling (see: Figure 3.7) the calculated values do not change; i.e. the optimum parameters are still the ones obtained from the previous point, at larger strain step size. As expected, the fit of the strain energy expression in terms of strains, gave a better R^2 values, as opposed to the use of very large strains or the use of noise data values. From this set of calculation parameters, we can find the optimum maximum applied strain.

Strain Approximation

We will now compare the effect of the type of linear strain approximation employed. We can use the metric tensor; $G = \tilde{h}h$, where $\tilde{h}$ is the transpose of the strained crystal lattice vectors, to define the strain tensor $\in_{ij}$ as[294]:

$$\in_{ij} = \frac{(h_0^{-1}Gh_0 - 1)_{ij}}{2} \qquad (17)$$

Solving for 'G' we can find the value of 'h' or the lattice vectors of the strained cell. This is called the linear finite elastic strain approximation. The tensor method, further referred here as 'finite elastic' strain method, or 'G', has been used previously to study the mechanical properties of polymers with molecular dynamics methods[266]. For a total of five strain points, we obtain the following values (Table 3.2).

Table 3.2 Second order elastic constants in GPa. Maximum strain value 'Strain' reported as percent (%).

Al	Exp[295]	Exp[296]	'G'	'E'	Strain
C_{11}	123.0	114.3	118.03	114.94	2.5/2
C_{12}	64.8	61.92	62.34	60.13	2.5/2
C_{44}	30.9	31.61	34.64	34.42	3

FeSi	Exp[256]	Exp[262]	'G'	'E'	Strain
C_{11}	338	327.5	380.21	380.02	0.5
C_{12}	112	30	135.31	135.23	0.5
C_{44}	136	145	152.42	152.16	0.75/0.5

HfN	Exp[249]	'G'	'E'	Strain
C_{11}	679	602.54	603.96	0.75%
C_{12}	119	103.32	100.23	1%
C_{44}	150	119.97	117.47	0.75%

Worth notice are the systematically smaller values for the 'E' strain as compared to 'G'. We choose the strain value limits that are at least twice the value of our minimum convergence vale, and its asymmetry is comparable to this convergence limit. Data

points that lie below this detection limit are treated as 'noise' and removed from the polynomial fit. In order for a comparison we have reported available data for Al[262,295,296]. The value obtained from 'E' is slightly smaller than for the case of 'G', for all but the case of HfN C_{11}. In particular for Al, the softer material, the C_{11} obtained from 'G' strains is closer to the experimental value of Sutton.

The rest of the constants are closer when calculated from 'G' for the other two reported. For the case of FeSi, there is a large discrepancy from the value of C_{12} reported by Serrao and the indirect value of C_{12} of Zinoveva, the later obtained indirectly from transverse wave experiments. It is interesting to observe that when the system can relax to its optimum ionic positions, both engineering and finite elastic strain give comparable results. This being valid only if proper converge parameters and accuracy values are considered.

Elasticity through Linear Responses

Formulations of the metric of the strain tensor have been proposed for density functional perturbation theory [250]. Linear response theory calculations predict the change in energy with respect to strain evaluated by finite differences from the thermodynamic reference configuration. As such, their values can be used as a benchmark calculation to which we can compare the finite strain calculations, where the unstrained reference state of the crystal is not preserved. Energy responses with respect to infinitesimal displacements are considered; therefore they require a very well converged wave function and more constraining tolerances.

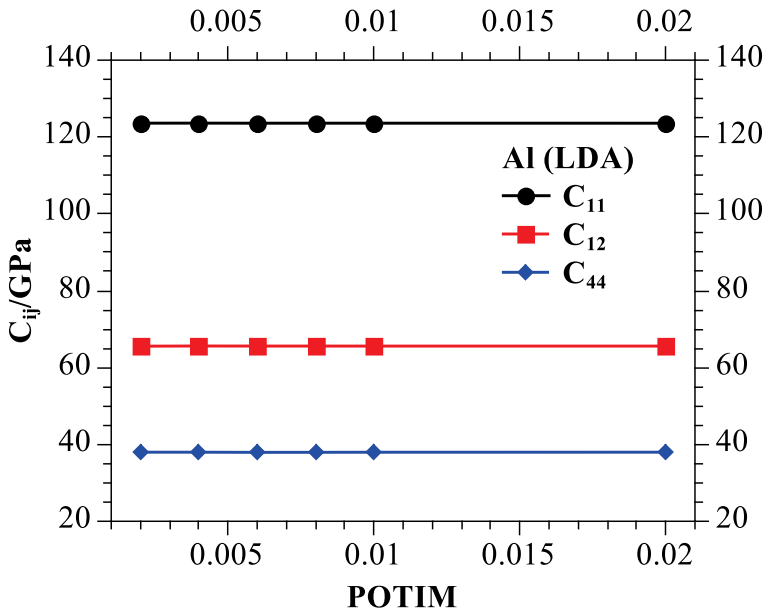

Figure 3.8 Change in the values of the calculated elastic constant for Al (LDA). Different strain steps. Notice how convergence is rapidly attained; even at the extended parameters of 585 eV e-cut and 16 KPT, the change in elastic constants is smaller than $1x10^{-3}$ Kbar with respect to the largest values.

For the case of HfN, a value 30% larger than the one found from equation of state calculations reproduces results in close agreement with converged values for all calculated elastic constants. This energy cutoff criterion was adopted for the rest of the studied systems. The electronic self-consistent cycle tolerance is set to $1x10^{-10}$ eV. With respect to the number of sampling points in reciprocal space, we found that an increase to the next K-mesh size (14x mesh is increased to 16x) gives values closer to the experimental ones. The difference is reduced after increasing the energy cut-off threshold value and increase in the size and the integration mesh density. In relation to the convergence of the calculation with respect to the displacements (Figure 3.8), we find all systems to converge rapidly, if the appropriate electronic structure parameters are previously set to reflect the demands of the calculation.

Table 3.3 Values from linear response calculations. Labelled here as: 'LRT', compared to, volume conserving strains (V) and non-volume conserving strain (non-V) results shown in columns; 'lrt-V, and 'lrt-nV'. Cij's reported in GPa, while differences (Δ) with respect to LRT results are reported as percent.

HfN

	LRT	non-V	V	Δ(V)	Δ(non-V)	lrt-V	lrt-nV
C_{11}	597.22	602.54	593.87	12.54	11.26	0.56	0.89
C_{12}	106.41	103.32	105.89	11.02	13.18	0.49	2.91
C_{44}	118.48	119.97	117.45	21.70	20.02	0.87	1.26
B_o	270.01	269.72	268.55				

Al

	LRT	non-V	V	Δ (V)	Δ(non-V)	lrt-V	lrt-nV
C_{11}	112.92	118.03	113.38	0.81	1.48	0.41	4.53
C_{12}	61.07	62.34	59.32	4.31	0.56	2.87	2.07
C_{44}	34.41	34.64	34.60	9.47	9.60	0.57	0.69
B_o	78.35	80.90	77.34				

FeSi

	LRT	non-V	V	Δ (V)	Δ (non-V)	lrt-V	lrt-nV
C_{11}	384.12	380.21	379.58	12.30	16.10	1.18	1.02
C_{12}	136.61	135.31	134.08	346.95	351.04	1.85	0.95
C_{44}	152.52	152.42	152.35	5.07	-5.12	0.11	0.07
B_o	219.11	216.95	215.92				

* C_{12} is obtained from the bulk modulus fitted to the EOS of each particular system

Volume Conserving Strains

In volume conserving strains the 'h_0' matrix remains constant after deformation. For all but the 'd1' type of strain, the error in the polynomial expansion goes to the fourth order term. Therefore, the effect of third order contributions in the calculation of second order elastic coefficients is removed. We now evaluate the effect of this type of strains, and compare them with results obtained from linear response methods. From the tabulated values (Table 3.3) is indeed found that the second order constants obtained from volume conserving strains, compare to the values obtained from linear response calculations.

Table 3.4 Third order elastic constants. Results for both 'G' and 'E' type of strains reported. Experimentally found values for Aluminium included. Values in GPa.

Al	E	G	Exp[297]	Exp[298]
C_{111}	-880.56	-1248.77	-1224	-1076
C_{112}	-212.15	-466.52	-373	-315
C_{114}	0.27	-1.95	250	360
C_{155}	-175.87	-134.74	-640	-230
C_{123}	-227.89	284.02	-368	-340
C_{456}	14.32	29.30	-270	-300

FeSi	G	E
C_{111}	-4928.96	-3641.24
C_{112}	-792.36	-616.06
C_{114}	-102.82	-58.86
C_{155}	-232.22	-315.76
C_{123}	-188.44	-187.87
C_{456}	-149.10	-89.58

HfN	G	E
C_{111}	-9673.56	-7488.83
C_{112}	-336.42	-213.49
C_{114}	100.63	68.61
C_{155}	-183.64	-236.10
C_{123}	229.75	214.92
C_{456}	-89.08	28.78

By contrast with results from non-volume conserving strains; FeSi is less sensitive to the type of strain. Values from symmetric shear strains, or 'd4', (see: appendix), do not show any significant difference. The use of "d4" allows very small asymmetric energy difference, i.e.; more accurate values (higher signal/noise ratio). Solving the linear system of equations required to obtain the energy expression after a given strain is applied, becomes restrictive with systems of lower symmetry than cubic, due to indetermination. Driven by this limitation, we now explore the effect of higher order contributions through third order elastic coefficients that can be obtained from non-volume conserving strains.

Introduction of Higher Order Terms

Third order coefficients are obtained through both engineering and finite elastic strains. We have removed noise data points, and, used the largest strain amplitude available. This is done aiming at maximizing the contribution from third order terms (Table 3.4).

The only directly calculated point is C_{111}, and C_{456}, while the rest are calculated indirectly from the value of C_{111}, C_{112}, C_{123}, or C_{144}. We can see that for the only system which available experimental data is obtained, Al, the finite elastic strain methods give results comparably close to those reported by Thomas[297], this is true also for C_{112}. In general, the values for FeSi, as it was the case for the second order constants, are closer to the value compared by each method. The effect of storage of strain energy, through molecular rearrangements, will be explored by comparing the effect of affine transformations.

Strain through Affine Transformations

In order to elucidate the effect of the straining and the relaxation of the internal structure with the elastic response, we have studied the difference in the 'E' d1 strain amongst optimized and single point (no relaxation) energy structures of FeSi. Comparing the effect of relaxation of the structure to minimum forces, we found a difference of 50 meV between the two structures. The optimized structure had a lower energy of -7.346 eV/atom. The effect of applying a non-linear elastic ('E') strain results in an increased Fe-Si distance, on the average larger than the 'G' strain (2.342 Å vs. 2.339 Å). The biggest difference in optimized energy at 8% strain was found for the

volume conserving, d1-B strain, with 5.43 meV/atom. In the optimized structure, we see that the upper atoms from the 'XZ' plane moves further away from the origin along the z axis, and the lower atoms shift closer to the origin along the x axis in the [10-1] direction. The larger distance between silicon atoms here is between the silicon atoms closer to the [111] corner (further away from the origin) in the unit cell. There is a distance of 0.867 Å. The smaller distance difference is of .3404 Å, from the silicon atoms closer to the origin along the 'Y' axis. For Fe atoms, the largest separation amongst optimized and unrelaxed coordinates is 0.7173 Å. For the LDA exchange functional, the largest energy difference between optimized and single point energy calculation was also in the d1-B volume conserving strain. This indicates that a relation with the type of strain itself, which adds a contribution to the third order to the total elastic strain energy. It also indicates that a better representative of an elastic response in reference to a zero stress state; in this case, d1 (vs. d1-B). Upon optimization, there is an increase in the average bond distance between Si-Fe within the unit cell from 2.426 Å to 2.455 Å. The Fe-Fe interatomic distance increases from 2.855 Å to 2.874 Å. In the same fashion, we found that the acute angles formed by Silicon centres with neighbouring Fe atoms relax from 68° to 64° The structure rearranges to store the extra strain energy caused by the elastic deformation We can ascribe the difference in energy from the un-relaxed and relaxed system to the change in the internal parameters for this covalently bonded system, namely the bond lengths and angles. This could explain the apparent diminished sensitivity of the systems to different calculation parameters and type of strain approximation employed.

Observations

Since the tensor nature of the applied strain is found to be commonly absent in literature, we embark in systematically studying the effect of both the engineering type and finite elastic strains. For the calculation of second order elastic constants, the difference between the two types of applied strains increases with strain amplitude, but give comparable results when optimized calculation parameters are found. In the system in which there is no internal degrees of freedom, the difference between the finite elastic strain and engineering type of strains are smaller values for the later strain. The difference is more noticeable in the case of shear coefficients. Use of particular volume conserving strains is assessed with values obtained from linear response theory calculations, which show to be in closer agreement as compared to non-volume conserving strains. For all but the strain labeled 'd1', the use of volume-conserving strains gives second order elastic constants, which have no contribution of higher order terms, up to fourth order. Values from volume conserving strains were found to agree closely to values obtained from linear responses.

As indicated in other studies[247,299], preference to a denser k-space grid should be given against the size of the basis set, when the demand of the calculation asks for a particular choosing, with the selection of special symmetric points to reduce unnecessary computation demands. Since the elastic response of the system is measured with respect of a strain free or 'reference' state, care should be taken when the size of the strain amplitude is chosen. We have found that the zero stress state is violated rapidly when the size of the strain value is increased. The minimum strain value is based on convergence

parameters and the elastic response of the system. As such, this value is found to be dependent on the material under study, being smallest for the stiffer material. For the particular studied cases, this value was similar for both shear and axial strains, but there is no reason to imply that this behaviour is to be found systems with different stiffness. In general, the minimum strain value should be assumed strain dependent also. In general, the strain energy difference should be large to be easily measured, but higher order contributions, should be kept minimum. Third and higher order terms can be negligible, until a large strain is applied. This prevents a reliable calculation of second order constants when very large strains are employed. If noise data is used, erratic behavior of the calculated values can be found. The effect of higher other contributions to the strain energy expression and the limit of minimum energy difference, indicates an optimum strain amplitude value. This value is found to be system dependent. We have found that calculation of third order elastic constants from 'G' strains give results comparable to experimental data, when the largest (d=8%) was used.

In general, the system e-FeSi with internal degrees of freedom, showed the least sensitivity to parameters related to the accuracy of the calculation. Relating experimentally obtained values with the value of obtained coefficients, we find that a deviation exists with increasing stiffness. The effect of affine transformations was studied for the system with internal degrees of freedom FeSi. Analysis of the internal parameters of FeSi show that this covalently bonded system have different means of storing elastic energy, namely in the form of bond angles and bond lengths, which could

explain the apparent diminished sensitivity of the systems to different calculation parameters and type of strain approximation employed.

We can envision a methodology, where accuracy parameters based on the electronic structure of each system are obtained, as a starting step. This enables finding the reference state. From here, appropriate choosing of optimum strain parameters is performed, and C_{ij} coefficients are determined. For the fit to the strain energy expression, data points that lie below the accuracy of the calculation can then be removed. Beyond a re-evaluation of previous *ab initio* studies on elasticity previously reported, the proposed methodology should set precedent for studying other type of materials and systems (e.g.; molecular crystals, polymers, etc.) with ranging values of elasticity. We can foresee the cases when the strain energy values are largely asymmetric. Here, choosing of maximum strain energy value is of particular relevance. Automation of these types of calculations should be then based on the particular type of systems and strains under study. The proposed methodology can be further be used to help in understanding the effect of other type (i.e.; non-linear) type of strains, where the effect of higher order contributions can also be expected. Beyond a re-evaluation of previous *ab initio* studies reported, the proposed methodology should help set a precedent for studying materials of ranging stiffness, e.g.; molecular crystals, polymers, etc., and help understand the effect of other type (i.e.; non-linear) of strains.

A relevant observation is the fact that the mechanical stability of the system can be observed from the mechanical properties of the system. The AlN B2 phase, does not comply with the requirement of a positive determinant for the second order elastic

tensor. This can be observed from the results found in Table 3.5. In this case the C_{33} value is almost an order of magnitude larger than C_{11}, but negative.

Table 3.5 Second order elastic constants for the 'B2' structure.

AlN	**B2**
C_{11}	477.69
C_{12}	40.13
C_{33}	-1852.15
Bo	185.99
V_0	17.86

The instability is confirmed from analysis of the phonon band structure (Figure 3.9). Negative branches depart from the value of 0 frequency, in the long-wavelength limit, near the Γ point.

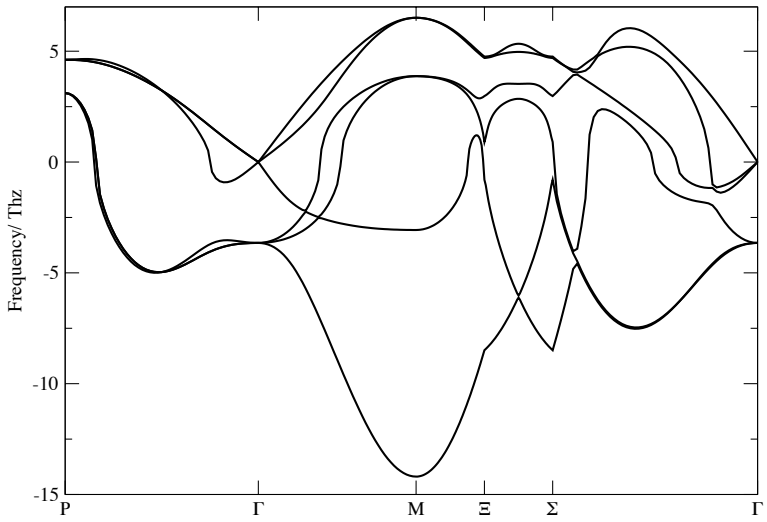

Figure 3.9 Phonon dispersion frequencies for AlN (B2).

Even in the limit of 0K, without kinetic energy and stress contributions found at higher temperatures, the elastic coefficients can be a property of valuable information when understanding the behaviour of materials in different thermodynamic conditions.

We will now proceed to study the particular issues found when trying to model the behaviour of other thermodynamic equilibrium properties of energetic materials.

CHAPTER IV

THERMODYNAMIC EQUILIBRIUM VALUES

Thermodynamic Limit

Since the initial timescales are so short (in the order of picoseconds) and the characteristic length-scales associated with detonation are so short, the first attempt to study detonation phenomena was achieved with the application of principles of conservation. The set of all points f(V,P,T) that can be accessed through a single point is called the material's Hugoniot line[300]. A block of material that is subject to a sudden compression, or shock, will increase its pressure, as the unit volume, or density reduces drastically. The initial state is depicted by 'a' in Figure 4.1 (below).

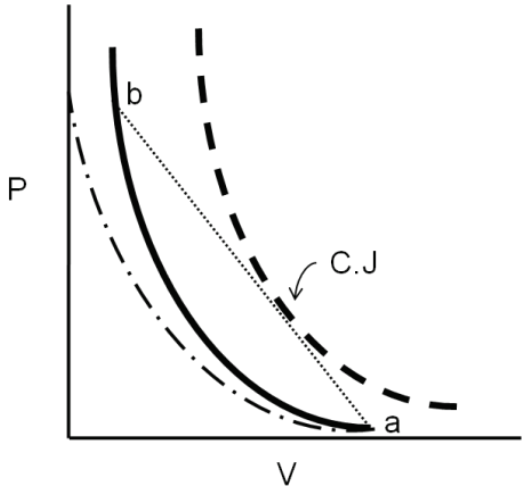

Figure 4.1 Initial conditions at (P_0,V_0). Hugoniot of the unreacted material (solid curve), Reactive State b(P_1,V_1), Hugoniot of the detonation products (dashed), Raleigh Line (dotted). The Chapman Jouguet Point is tangent to the Hugoniot of the detonation products. Cold compression curve (dash-dotted line)

Upon Reaction, at the state ‘b’, the detonation will cause departure towards the Hugoniot line of the products, until the final state is reached. Here, C.J, is the Chapman Jouguet tangential point, which is collinear to ‘a’ and ‘b’. It indicates the maximum pressure that can be achieved by the detonation front in conditions of steady state. The line that crosses these three points is called the Raleigh line. As opposed to a sudden compression, a reversible compression requires less energy, as observed from the area under the dash-dotted line, and it follows an isotherm.

Under a specific state in volume or pressure, the corresponding energy for each system can be describe through the use of a proper equation of state(EOS). At each state, relaxation of the atomic positions is achieved through optimization of the ionic degrees of freedom; cell shape is optimized through the corresponding cell parameters. For materials in which cohesive forces in the crystal unit cell are mostly covalent, (as opposed to weaker dispersion forces), usually the equation of state is sufficient to predict phase changes and their relative stability. For the case of molecular crystals, the equations of state are the initial step in understanding how different changes in structure can alter the sensitivity of the material. As mentioned before, conservation laws can describe the steady state between the initial and shocked states[17];

$$u_a \rho_a = \rho_b u_b \tag{18}$$

$$P_a + u_a^2 \rho_a = P_b + u_b^2 \rho_b \tag{19}$$

$$e_a + \frac{p_a}{\rho_a} + \frac{u_a^2}{2} = e_b + \frac{p_b}{\rho_b} + \frac{u_b^2}{2} \tag{20}$$

Common nomenclature use ‘D’ for the speed of propagation of the shock, and ‘u’ for the jump in velocity in the undisturbed medium. Here, u_a denotes the particle velocity at the material an u_b denotes the shock velocity, r and P, denote density and volume, correspondingly. In this way;

$$D = -u_a \tag{21}$$

Aknowledgment of the specific volume as the inverse of the density, a third relationship, known as the Hugoniot equation, is obtained, in which the velocities are no longer used;

$$e_b - e_b = \frac{1}{2}P(V_a - V_b) \tag{22}$$

This type of plots can be obtained from single shot experiments, and are reported in terms of particle velocity, and shock plate velocity. Similarly, the velocity of the shock wave (D) is obtained by the following relationship:

$$D = v_0\sqrt{\frac{p_1 - p_0}{v_0 - v_1}} \tag{23}$$

Since all engineering models depart from fundamental thermodynamic relations, obtained from the equation of state, we will continue with their study. An accurate representation of our system will enable us to pursue other type of information, like second order elasticity, and anisotropic properties at elevated temperatures and pressures.

Errors in Equilibrium Properties

For the calculations of the equations of state, projector augmented plane wave type of potentials[205] with Perdew-Berke-Ernzerhof exchange correlation functionals [206] (hard version) were employed with the intention of obtaining energy-volume and energy pressure characteristics at the optimized (relaxed) structural parameters (e.g. c/a ratio) for two prototype EM compounds, NM and PETN.

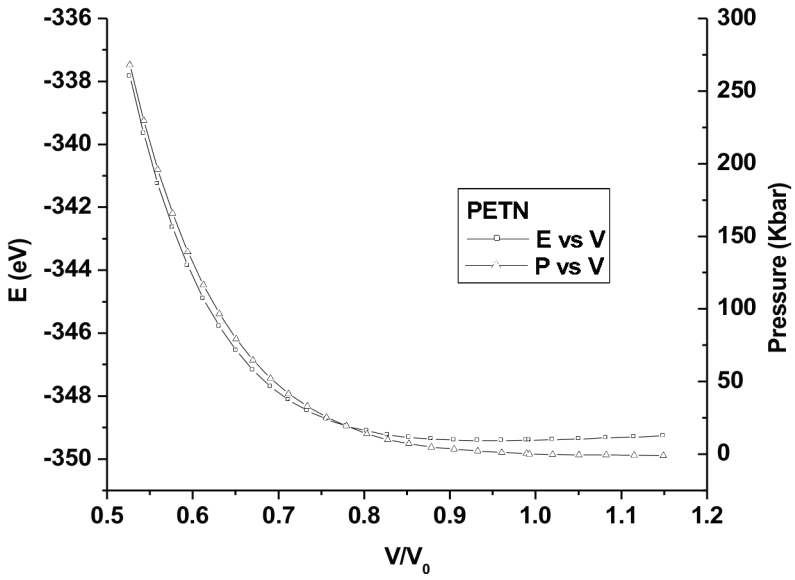

Figure 4.2 Equation of state for PETN. PAW/PBE.

In Figure 4.2 we can find the obtained equation of state from plane wave approximation of PETN, with limit of 1 keV cutoff energy, in a 2x2x2x symmetric inverse space mesh. The equation of state represents the difference from their equilibrium structure (ordinate axis, left) and the change in pressure (right). Fraction from the equilibrium volume can be found in the abscissa. The pressure curve continues its decrease below 0 Kbar, at larger V/Vo values.

The zero stress "a" lattice for PETN was found to be at 8.15% larger than the experimental value. Multiple intermolecular rearrangements and the effect of softer van der Waals and hydrogen bonding forces are suspect to create this deviation from experimental value.

Table 4.1 Model for PETN. Equilibrium properties.

PETN MODEL	$A+B1*X+B2*X^2+B3*X^3+B4*X^4$
A	5960.207189
B1	-33.59131542
B2	0.071293452
B3	-6.7367E-05
B4	2.39E-08
Vo=	737.20 A^3
K=	51.08 Kbar

From a fourth order model (Table 4.1), the obtained bulk modulus value fails to compares to the experimentally reported (ca 9 GPa[301]) even though PAW type of potentials have shown some disagreement with experimental values with these type of compounds[302]. The equation of state obtained for NM and β-HMX are in no better agreement with experiment than PETN. A summary of the found results within plane wave approximations and a comparison with experimental values is found in table 4.2.

Table 4.2 Comparison with experiment values. Stiffness coefficients.

System	Vo	Bo(Gpa)	B(exp)
β-HMX	601.068	4.94	12.1662
PETN-i	688.393	3.65	12.7763
NM	333.839	3.84	8.50933

As opposed to LCAO methods, and compared to what is commonly found in studies of metals and metal nitrides[303], effects of dispersion ar poorly aquainted by current plane-wave methods. We shall report our current findings, and confirm that, evne though empirical methods can be of use for the comparison with experimental data of certain systems, there are still further refinment necessary, wich is mostly noticeable form the calculation of the elastic properties.

Dispersion Corrections

Besides being a requirement for developing engineering models and to understand the behavior of the material in the conditions of its envisioned applications, a proper description of the potential energy surface bears further implications when determining thermodynamic properties of solids. Despite its successful application in many strongly bound systems, current approximations employed within Density Functional Theory[97] (DFT) methodologies have been unable to correctly predict interactions that are significant to various biological and biochemical molecules[304] and neutral molecule crystals like those of rare-gas dimmers[305,306], polycyclic and aromatic hydrocarbons[307-309], and energetic materials[162,310,311] (EM). This is of specific relevance when calculating properties like bulk modulus, and second and higher order elastic constants, even for qualitative purposes. It has been suggested in literature that the lack of a proper description of the equilibrium volumes in these molecular systems[104,205,312-316] can be attributed to the lack of a proper description of the long range induced dipoles by neighboring molecules. To overcome this hurdle, some recent efforts have been directed towards developing methodologies to target specific type of systems, like polymers[317] or

rare-gas dimers. Some attempts to improve the current description of intermolecular forces at a higher level of theory include the choosing of a better description of the exchange functional, with some success mostly from parameterized generalized gradient approximations[306] and "hybrid" functional (X3LYP)[318], the use of orbital-dependent functionals[319], optimized effective potentials[320] or the addition of an external correction to the total ground state energy[314,321,322]. Even the use of perturbation methods, like the spin-component-scaled MP2, have been estimated as inadequate for common pi-stacking and hydrogen bonded interactions[323]. We have decided to test the idea of correcting the total energy of the equations of state for some energetic materials and other molecular crystals, by introducing a damped Buckingham type of potential[324,325] that accounts for dispersion forces. The implemented empirical term for the dispersion energy was developed by Elstner and Le Sar[325,326]:

$$E_{vdW} = \sum_{ij} \frac{c_6^{\alpha\beta}}{R_{ij}^{\alpha\beta 6}} f(R) \tag{24}$$

The damping function used here allows a decay to zero at a value ca. 3 Angstrom, to avoid over counting of bonding energy:

$$f(R) = \left(1 - e^{-d\left(\frac{R_{ij}^{\alpha\beta}}{R_0^{\alpha\beta}}\right)^7} \right)^4 \tag{25}$$

For ease of comparison, the inner and outer exponents are constantly kept as 7 and 4, to allow for a similar behavior of the decay distance as previously reported results. The parameter "d", called the decay factor, is related to the value at which the damped

function will experience an inflexion (viz. $1/r^6$), a value of 3 is chosen for the present calculations. The form of the functional is important since evaluation of fist and higher order derivatives (e.g gradients, polarization, etc…) is necessary for calculation of other system properties. In this way, correction of the total energy determined from the Kohn-Sham Hamiltonian is corrected with the addition of an E_{vdw} term:

$$E_{total} = E_{KS} + E_{vdw} \tag{26}$$

Using polarizability values obtained at the MP2 level, Williams and Malhorta[327] have obtained C6 coefficients that can be used in calculations with the 6-21G(**) basis sets used to reproduced the energetic behavior of 24 hydrogen bonding and Van der Waals molecular interaction. These were obtained from scaling DFT energies to values calculated at the MP2/cc-pVQZ level, for dimmers like ethane, formaldehyde, benzene, water, etc. We would like to address the use of this correction[328] by systematically studying its effect on energetic materials, as well as in other molecular systems. This method can be less computational intensive as compared to other type of procedures (like those that encompass basis set optimization and the inclusion of thermodynamic data[49]. There are some systems, like for PETN-i in which two different type of oxygen atoms are present; one bridging and a pair sharing a resonant bond in the nitro group. Evidently, the chemical states of the nitrogen atoms bonding these two different types of oxygen atoms are different. Two different coefficients for nitrogen have been utilized. For those interactions whose coefficients were not reported, Van der Waals radii and coefficients have been obtained as described previously[327], based on hybridization or chemical environment of the atomic species. We have followed the same nomenclature

used by Miller, e.g; a tetrahedral sp3 carbon is labeled (CTE), a sp3 hybridized oxygen is named OTE and so forth. By means of atomic polarizability values (p_a), coefficients can then be scaled using also the number of effective electrons (N_a);

$$C_6^{\alpha} = 0.75\sqrt{N_a p_{\alpha}^3} \tag{27}$$

N_a is obtained as proposed by Halgreen[329]:

$$N_{\alpha} = 1.17 + 0.33 n_v^{\alpha} \tag{28}$$

The C6 coefficient is then obtained by means of the Slater-Kirkwood approximation[330]:

$$C_6^{\alpha\beta} = \frac{2C_6^{\alpha}C_6^{\beta}p_{\alpha}p_{\beta}}{C_6^{\alpha}p_{\alpha}^2 + C_6^{\beta}p_{\beta}^2} \tag{29}$$

As an example we show the values of the coefficients used for β-HMX is shown in the Table 4.3. Since R^{-6} interactions should have an effect at long enough distances[331], we have considered summation of the E_{vdw} interactions in a super-cell considering 4x4x4 primitive cells. Troullier-Martin pseudopotentials[99], with the PBE exchange and correlation functional[98] were employed. Although the recommended values for Troullier-Martins pseudopotentials[99] is 60-100 Ry. as cut-off, we found that 200 Ry, was necessary to converge the system's energy of a sample NM crystal, composed of 1 molecule. Geometry and wave function optimization was achieved using a linear scaling limited memory BGF algorithm[332], as implemented by the CPMD[333] code. The use of plane-wave type of functions as basis for this type of calculations precludes the effects of basis set superposition errors (BSSE).

Table 4.3 Employed C6 coefficients for β-HMX.

Hybridizations	C6:	R_o:
(1) H–H	-2.29	3.538
(2) CTE–CTE	-18.394	5.14
(3) NPI2-NPI2	-2.882	4.535
(4) NTE–NTE	-19.489	4.535
(5) OTR4–OTR4	-8.123	4.233
Interaction:	C6:	R_o:
1 - 1	-2.29	3.583
1 - 2	-1.644	4.625
1 - 3	-1.371	4.158
1 - 4	-1.805	4.158
1 - 5	-2.756	3.947
2 - 2	-18.394	5.14
2 - 3	-19.305	4.875
2 - 4	-18.9272	4.8752
2 - 5	-7.731	4.773
3 - 3	-2.882	4.535
3 - 4	-1.5934	4.5350
3 - 5	-3.494	4.395
4 - 4	-19.489	4.535
4 - 5	-7.7968	4.3944
5 - 5	-8.123	4.233

Small tolerances on the wavefunction gradients ($1x10^{-7}$ Hartree) and relative a small tolerance on the relative energy difference for the optimization cycle to another ($1x10^{-6}$ Hartree) was found to be required for the calculations. Although tried initially, no fixed space group assignment was done to the crystalline lattice, keeping the ionic degrees of freedom as variable. Unless stated explicitly, the experimental lattice ratios (c/a, b/a, etc…) and angles have been keep fixed throughout the calculations.

Effects on Energetic Materials

The correction through Grimme's parameters to molecular crystals was completed. For the case of EM's, we were able to obtained, through an in-house code, the optimized lattice parameters for PETN and NM. We see that in general, the correction of LeSar is in closer agreement with experimentally found data.

Table 4.4 Summary of equilibrium parameters. Grimme and LeSar corrections.

NM	P	a	b/a	c/a	E
Exp	0.00	5.1832	1.2031	1.6434	
Grimme	-13.68	4.1327	1.5870	2.4573	-197.639474
Elstner	-0.38	4.0907	1.6757	2.4004	-197.609316
NoV	9.07	4.1090	1.6833	2.3578	-197.552109
V=	275.31				

PETN	P	a	c/a	E
Exp	0.00	9.3027	0.7138	
Grimme	-6.08	9.2808	0.7189	-529.595417
Elstner	4.08	9.2766	0.7199	-529.538830
NoV	15.96	9.2964	0.7153	-529.383679
V=	574.65			

Experimental reference unit cell volume have been obtained for the energetic materiasl: β-hmx[146-148], fox-7[149-153], tatb[154-157], nm[158-160],petn[161-164] and 2-4-6-trinitrotoluene[165-168]. As a fist set of comparison, we obtained the EOS of PETN without any type of parameterized correction. In this case the only the internal degrees of freedom (ionic positions) were optimized, keeping the experimental c/a ratio[163]. Change in volume through an expansion coefficient 1, 2, 4, 8 and 16% from the lattice parameter were employed. Although output of the optimized coordinates is given in Cartesian coordinates, conversion to direct (fractional) coordinates for the successive run using the

strained lattice parameters was perform via a home-made code. This in turn decreased the computation time required for the ionic optimizations

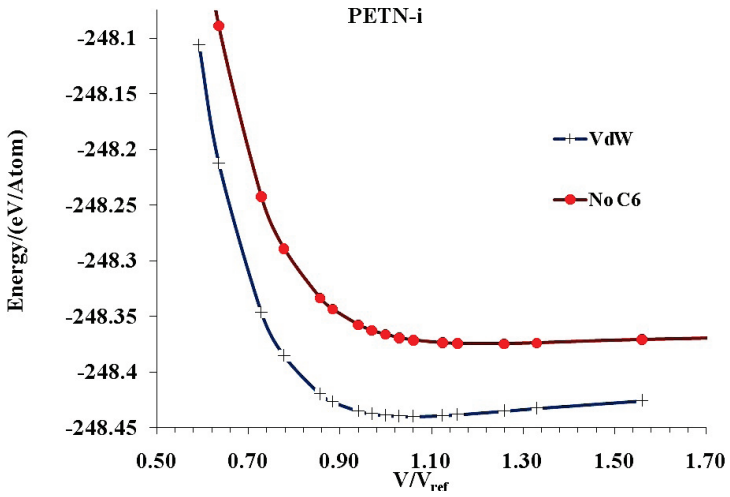

Figure 4.3 VdW (blue) and non-corrected (No C6) EOS of PETN.

In the Figure 4.3, we can observe an overlay of the equations of state for PETN. The curves lower in energy are the ones obtained with the use of C6 coefficients. The dark blue colored curve has been obtained from the end coordinates of the equation of state in which the crystalline space group has been fixed. We can find the equilibrium properties for the VdW corrected equation of state in Table 4.5:

Table 4.5 Summary of equilibrium energies. PETN, bulk modulus value included.

	V_0 (Å^3)	B_0 (GPa)	B'
Exp[163]	574.6735		
Exp[161]	591.5713	8.8	9.9
Exp[162]	590.8	11.7,9.4,12.2	6.8,11.3,6,4
No C6	695.23	3.2	13.67
VdW	607.67	7.85	10.11

There is a notably large array of results that can be obtained in literature, particularly from the group of Ollinger and Cady, indicating the sensitivity of the quality of the crystals obtained to experimental parameters. Our results seem to be comparable to the value of 590.1 (large by ca. 3%). The bulk modulus is smaller by 2%. A tetragonal system, nitromethane is found in condensed liquid state at ambient condition. Although some groups have reported the non-existence of hydrogen bonding[334] in liquid nitromethane, through CPMD simulations (weakness in their simulation; 25 Ry cutoff, no VDW us=100,) Winey and Gupta proposed based on Pressure-Raman experimental vibrational spectroscopy that its decomposition could proceeded via head to tail collision[335]. This system is used commonly as a "benchmark" molecule due to its small number of atoms per unit cell (28). We can see from Table 4.5 the reported equilibrium values. There is a reduction on the overestimation of the equilibrium volume. Although still large, an increase in 3.5% is comparable to the results obtained by Olinger and Cady[161]. In the same fashion, correction by means of the description of C6 coefficients for NM were used to compare the between uncorrected EOS. Values for the bulk modules, and its first and second order pressure derivatives have been obtained for both C6 and non C6 coefficient corrected curves. The bulk modulus is still smaller than the experimentally obtained by Cromer[159], this results compares to the ones obtained previously with PAW pseudopotentials for other systems, although the equilibrium volume has been overestimated ca. 4.5%, agrees better with the experiment. After performing calculations with the parameterized Van der Waals corrections to the free energy, the system show an overall decrease in the zero stress, or minimum energy

volume. Calculations with optimization of the cell parameters show an increase in the agreement between the experimental results and the calculations, both in terms of equilibrium volumes, and bulk modulus. More data points are required for the correct calculation of the pressure derivative of the bulk modulus.

For 1,1-diamino-2,2-dinitroethylene, also known as Fox-7 is an energetic material that has the particularity of entail an electron withdrawing group (head) on one side of the molecule, and an electron donor amino group (tail) in the other. These molecules arrange head to tail along the longitudinal axis, with a non-planar configuration. Dispersive forces between layers of molecules can be expected. Hydrogen bonds between layers and within the molecule itself increases the stability of the system, which is also reflected in a lowered enthalpy of formation[336], 2.48 eV. as compared to other energetic materials of the same elementary ratio. Due to the presence of seven resonance hybrids[337] , reported bond distances between C-N and N-O distances be comparable to a bond order of 1.5. The presence of a torsion angle along the layer of the molecule, has suggested that initiation can be due to hindered in different planes. In particular Kuklja[336] et al have found that relaxation occurs due to NO_2 rearrangement, and slips occurs preferentially through the [101] plane. They have inferred that electrical and thermal transport properties should then be highly anisotropic. The presence of competing reaction pathways, namely C-NO_2 fission and CONO rearrangement, is used to explained the particular low sensitivity of the system. Moreover, the presence of exited states and electron localization in any of the functional groups can induce intermolecular rearrangements that promote exothermal reactions. Experimental[338]

values from diamond anvil compression experiments as well as the equilibrium values obtained from the corrected and uncorrected fits to a 4th order B.M. EOS are found in the next Table 4.6.

Table 4.6 Equilibrium values for α-Fox-7. A^3 and GPa used.

	Exp	C6	No-C6
V_o	522.32/511.2	534.25	586.44
B_o	17.9	15.1	8.76
B'	6.6	7.92	9.18
B"		-2.3	-3.73

Agreement could be established between the calculations and the latest low temperature experiments, in that the discrepancy with the reference cell used for this EOS is ca. 5%.

With a triclinic unit cell[154] structure, 1,3,5-triamino-2,4,6-trinitrobenzene is regarded as one of the insensitive energetic materials[339], and is currently used as initiator for nuclear charges, and as desensitizer in different plastic bonded compositions. This molecule exhibits also intermolecular and intermolecular hydrogen bonding. Some of its unusual insensitivity has been ascribed to the presence of a glide plane between the layered molecular arrangement in the crystal unit cell[340], and an unusually large rotational barrier of the nitro group.[341] Dobratz has reported a sound speed value for TATB of 1.46 Km/s.

$$c = \left(\frac{B_0}{\rho} \right)^{\frac{1}{2}} \qquad (30)$$

From the above thermodynamic relation, we can find the estimated bulk modulus of TATB (r= 1.87 g/cm^3) to be ca. 4 GPa. This result contrast with the bulk modulus

obtained from MD simulations; 15.2 GPa. For comparison we have used both values as a reference. The summary of the calculated equilibrium parameters can be found in the next Table 4.7:

Table 4.7 Equilibrium properties for TATB. 3rd and 4th denote the order of the fit used.

	Reference	No-C6	VdW
V_o	442.52	542.74	480.54
B_o	4/15.2	4.40	11.03

The equilibrium volumes of the corrected and corrected systems vary by 8.6% and 22.6 % as compared with the experimental study, conducted at room temperature. A recent DFT study reports a value[342] 31.7% larger for the equilibrium volume, for an EOS obtained with DFT-GGA.

For the polymorph found at ambient conditions of HMX, this is; a monoclinic system with the beta angle close to 120°. There are 56 atoms per unit cell. A summary of the equilibrium parameters found, and other reported previously in literature can be found in the following Table 4.8:

Table 4.8 Equilibrium properties for β-HMX.

	Yoo/Cynn	Eckhardt	VdW	No-C6
V_o	528.40	517.16	524.46	595.47
B_o	12.40	9.90	12.60	6.12
B'	10.40	-	9.70	9.22
$V_{o\ Ref}$	519.42			

Eckhardt has reported by means of Brillouin scattering the value for the Voigt-Reuss-Hill corrected bulk modulus. Yoo and Cynn have reported the results on anvil-diamond experiments from XRD experiments from synchrotron radiation at pressures up to 27 GPa. We have used as initial reference structure the one reported Choi and Putin obtained from neutron diffraction experiments.[343] The VdW corrected b-HMX equilibrium value is comparable to the equilibrium structure obtained by Cynn et al. The non-corrected system gave a value of 595 $Å^3$is comparable to the expected behavior of equilibrium properties of molecular crystals as predicted by DFT. For TNT One of the energetic materials of most wide use in non-military applications, 2-4-6 trinitrotoluene, has 168 atoms per unit cell. Equilibrium values are shown in the following Table 4.9:

Table 4.9 Equilibrium values for 2,4,6-TNT. Experimental bulk modulus from ref[166].

	no-C6	c6	ref
Vo	2147.15	1884.87	1770.57
Bo	2.87	5.66	10.64
B'	15.15	16.91	
B"	-8964.36	-6307.13	

Optimization with the steepest descent method was not possible with the VdW-corrected unit cell of b-hmx, as in all instances proceeded to an expansion of the lattice. Comparison of the molecular structure can be made with the values reported at 4.2 K from Trevino et al[158]. The reported bonds lengths for the C-N bond, and each of the N-O bonds in the resonant nitro group are are 1.48 Å and 1.223 Å and 1.209 Å. The methyl group has three bond measuring 1.079 Å on the average. The non-vdw corrected optimized structure had the largest discrepancy with the experimentally reported one.

The relative error in volume is ca. 21%, and the error in the lattice parameters a, b, and c, are 21.5%, -34.44 and -14.6, with c in the non-vdw optimized structure being 1.2676 Å larger than the 4.2K structure. The distance in the c-n sp3 bond is 1.424 Å. There is reduction of the nitro resonant bond angle, as compared with the experimental structure, which causes an increase in the 'b' lattice vector length. Along the 'c' direction, the shortest intermolecular oxygen-hydrogen length is 2.592 Å, and 3.2 Å on average; as compared to a short interaction of 2.412 Å in the experimental structure, for an average of 2.643 Å. This difference in intermolecular distances is observed as a drastic increase in the 'c' direction. This packing, in addition to the difference in nitro angles, drastically reduces de length of the 'a' vector, as compared to the experimental structure. The orientation of the methyl group with respect to the oxygen atoms has a phase of 26° from the equilibrium structure position. In order to describe earlier low temperature neutron diffraction experiments, Cavagnat[344] et al used a double well potential of the type $\cos(n\theta)$, with a barrier height of 10 meV. The rotation of the methyl angle at the ground state, without any temperature effects, could explain the observation in the VdW structure.

Lattice Parameter Optimization

As opposed to strongly bound systems, like metals, molecular crystals can have, due to the flexible character of the sp3 bond, many different conformations which minimize their overall energy. In particular for nitromethane, we faced many optimization steps, at a given constant volume in which small variations in the c/a ratio and b/a ratio (e.g.; 2.0019 vs. 2.0014 and 2.4519 vs. 2.4514) gave energies comparable in the mHartree

range. This just testifies for the complex potential energy surface that one has to sample to arrive at a local minimum. In order to obtain the lattice parameters that most reliably describe our systems at different thermodynamic states along the EOS, we have employed a method that optimizes the lattice parameters utilizing the difference of the axial components of the stress tensor, as calculated from the Hellman-Feynman theorem, from the hydrostatic pressure.

$$a = a_o\left(1 + \frac{(\sigma_{xx} - P)}{B_0}\right) \tag{31}$$

Here 'a' and 'a_o' are the optimized and original cell parameter, 'P' is the hydrostatic pressure and B_o is the 0 K bulk modulus of the system. The cell symmetry is such that the relative angles are kept at 90º. Usually 50 to 60 steps were required to converge the value of cell parameters to less than $1x10^{-4}$ Å, the maximum cell length precision used by the code. We have found that a smaller change step, using the bulk modulus larger by a factor of 5 or 10 is usually required to avoid missing any lower energy minima in the crystal's energy surface.

Table 4.10 Effect of VdW correction to DFT. Calculation of elastic constants. Values are in GPa. Volume in A^3. Adapted with permission from[284].

	C_{11}	C_{33}	C_{22}	V
PETN-NOV	17.67	5.51	-	696.05
PETN-VDW	33.32	11.90	-	609.84
PETN-EXP	23.11	17.35	-	574.64
NM-NOV	58.68	5.25	2.36	254.11
NM-VDW	71.92	9.42	6.06	297.19
Resorcinol-VdW	26.68	57.23	41.96	490.61
Resorcinol-exp	8.60	19.50	28.80	534.70

By means of finite strain method, we have calculated the diagonal elements of the elasticity tensor for the orthorhombic systems nitromethane, urea, resorcinol, and for the tetragonal systems PETN, (resorcinol, petn-nonv calculating). Nitromethane, as expected for a liquid system in normal conditions, was the lengthiest to calculate, due to the large number of local minima found after expanding or contracting the lattice parameters in each direction. The elastic behavior was found at the reported volume. There is a drastic effect on the results obtained from VdW as opposed to neglect of dispersion. Although the difference in the bulk modulus is still bigger than 18%, the small discrepancy (below 5%) between the predicted equilibrium volume and the one used for reference in the initial calculations, indicates that an empirical correction can be further refined to yield values closer to experimental ones, without sacrificing computational time[345].

Table 4.11 Effect of corrections in NM.

	A	B	C	V	NO2 (°)	N-O (Å)	C-N	C-H
Exp	5.1832	6.2357	8.5181	275.3125	123.252	1.216	1.480	1.079
VdW	4.0912	6.9393	9.8685	280.1669	121.593	1.249	1.423	1.107
Error(%)	21.07	-11.28	-15.85	-1.76	1.35	-2.71	3.85	-2.63
Non-VdW	4.1043	8.4602	9.9316	344.8527	121.593	1.249	1.423	1.075
Error(%)	20.82	-35.67	-16.59	-25.26	1.35	-2.71	3.85	0.37

An essential requirment for any correction method, we see that the effect of correction to dispersion forces are negligible, when comparing the qeuilibrium structure paramters of NM with the experimentally obtained structure (table 4.11).

Table 4.12 Equilibrium parameters for molecular crystals.

	Calculated						Experimental		
		VdW		Non-Vdw					
System	V	Bo	B'	Vo	Bo	B'	Vo	Bo	B'
β-hmx	524.46	6.73	10.03	588.87	12.49	8.80	528.4/517.16	12.4,9.9	
tatb	485.31	10.31	9.23	539.01	5.13	11.73	442.52,443.1	4/15.2	
petn	606.50	9.54	9.24	689.87	4.84	9.03	574.67/591.57	8.8,12	
tnt	1877.35	7.84	9.26	2141.59	3.07	12.75	1770.57,1830.4	10.64	8.00
fox-7	534.25	15.10	7.92	586.44	8.76	9.18	522.32/511.2	17.90	6.60
α-glycine	344.63	23.79	9.20	376.13	31.32	1.70	310.07	14.28	10.6
γ-glycine	242.53	21.93	7.65	265.07	11.35	12.75	234.43	25.28	5.39
n-benz	931.07	4.90	6.44	1038.96	3.06	6.78	708.8/679.8	7.24	
ethanol	257.14	11.77	6.59	302.00	6.53	7.97	194.90	1.03	
β-glycine	154.27	10.47	7.48	178.25	19.32	6.89	158.17		
urea	136.71	18.72	6.53	146.41	12.58	7.14	145.06	14.93/20	
durene	359.45	18.21	5.45	417.92	6.35	8.35	432.23	6.24	
Res.	505.97	16.14	5.97	551.20	12.22	8.07	534.70	14.34	
p-quin	230.25	16.36	7.07	257.84	10.04	7.59	248.29	14.84	3.49
benzene	406.94	12.00	7.36	579.76	2.82	7.87	462.514,465.62	5.85	
nm	254.11	10.97	8.28	297.19	5.40	8.10	275.312,292.7	7,8.5	
biphenyl	334.46	21.34	9.20	456.00	4.08	11.05	432.78	5.85	

Effects on other Molecular Crystals

As a mean to systematically study the effect of the inclusion of the c6 coefficients in the total energy of molecular systems, we have extended our study to the molecular systems: biphenyl[346], m-dinitrobenzene[347-349], ethanol[169], benzene[170-172],urea[173-175], cyclohexa-2,5-diene-1,4-dione[176](p-quinone), Benzene-1,3-diol (resorcinol)[177] and a-,b-, and g-glycine[178].Incorporation of the C6 coefficients had a direct effect in the equilibrium parameters as predicted from the equation of state. The bulk modulus for al

systems increased from 3.2 GPa to 17.3 GPa. The predicted equilibrium volume is smaller when the effect of VdW corrections is considered.

In general, there is a reduction in the error of the equilibrium volume, ranging from 6.63%, in the case of urea, to the most drastic case, that of benzene, in which the decrease in terms of volume is 29.8 % (Table 4.12)

The smaller reduction in the case of urea is expected, since most of the intermolecular interactions are dominated by electrostatic hydrogen bonding, while most of the intermolecular interactions in benzene are dominated by dispersion interactions of non polar molecules. However, for urea, the additional use of C6 coefficients, clearly overestimated the binding in the equilibrium volume observed in the condensed phase. After closer inspection, we can see that related to energetic materials, there is an increased agreement in equilibrium parameters for all systems, without an over-binding, but in the case of nitromethane. As in urea, the addition of C6 parameters, overestimated the intermolecular binding. For the rest of the molecular crystals, the used parameters clearly overestimated the cohesive energy in the unit cell. Only the cases of ethanol, dinitrobenzene and g-glycine do not fall in this category. For dinitrobenzene, a material exhibits an unusual short intermolecular O-O distance[347] with large oscillations in nitro group caused by temperature. It is of useful optical applications due to its non-linear properties. We have used the structure resulting at 100K from Mo ka radiation. It has an orthorhombic structure with P n a 21 symmetry (point group mm2). The equilibrium volume of the space group fixed, VdW corrected system is 755.9 $Å^3$ as compared to the value of 679.8 $Å^3$ of the reference crystal. For both cases, the equilibrium volumes will

be found above 15% of the initial reference volume. The symmetry of the molecule seems to account for the reduction in predicted equilibrium volume, without an overestimation in cohesive forces. The best agreement for both bulk modulus and equilibrium volume is found for the case of b-hmx, fox-7 and g-glycine. In both cases non aromatic carbon type of interactions are used. Stiffnes, as measured from the bulk modulus at equilibrium, is also the biggest for the aromatic systems, and artificially high for a-glycine. (31 GPa. vs. 14.3 experimentally). More than double of what is found experimentally. We have studied the effect of addition of a dispersion term, E_{vdw} to the total energy of two EM systems, PETN and NM. Comparison between "corrected" and "uncorrected" EOS indicates that parameterization of the C_6 coefficients employed can improve prediction of both equilibrium volumes and bulk modulus. We have found comparable equilibrium values for Fox-7. Also the implementation of C6 coefficients seemed to give good results in terms of equilibrium volumes for TATB, a cyclic aromatic system, with the lowest symmetry, and for 246-Trinitritolune, also a cyclic aromatic system and b-HMX, a non-aromatic cyclic system. The best agreement is found for the case of β-hmx, fox-7 and g-glycine. In both cases non aromatic carbon type of interactions are used. In general, systems in which the dominant dispersion interaction originated from aromatic systems, seem to have over-estimated the cohesive forces as observed from the reduced equilibrium volumes. The combine account for dispersion coefficients for the atoms in different chemical environments (e.g, nitro, amino, aromatic and aliphatic carbons) in the case of energetic materials, seem to have prevented an artificial over-binding.

For urea, evaluation of the stress tensor at all volumes showed that the difference in sxx was always bigger thatn syy=szz, indicating that the crystal structure may lose its tetragonal structure upon relaxation. We see, from table 4.10, that for systems in which strong hydrogen bonding interaction exists, there is essentially no noeed to account for dispersion corrections. Urea, an in general, systmes in the lower part of table 4.10, are examples of systems in which the equilibirum volume value shows an artificial overbining. Other anisotropic effect can be found when calculating the elstic constants for PETN and NM. one of the elastic constants was abnormally higher than the other ones. Ultimately, a good test for a proper dispersion description, should be able to reproduce the orthorhombic crystal system of urea, for which both vdw-and non-vdw optimized cell calculations by steepest descent, gave an orthorhombic system (at best), with no tetragonal symmetry kept. This study has shown that with a proper set of parameters are used to account for specific forces within a quantum mechanical framework; steps can be taken towards a predictive modeling of structure and properties of molecular crystals. However a proper optimization of the used parameters is required, due to artificial anisotropic effects and overestimation in the cohesive forces.

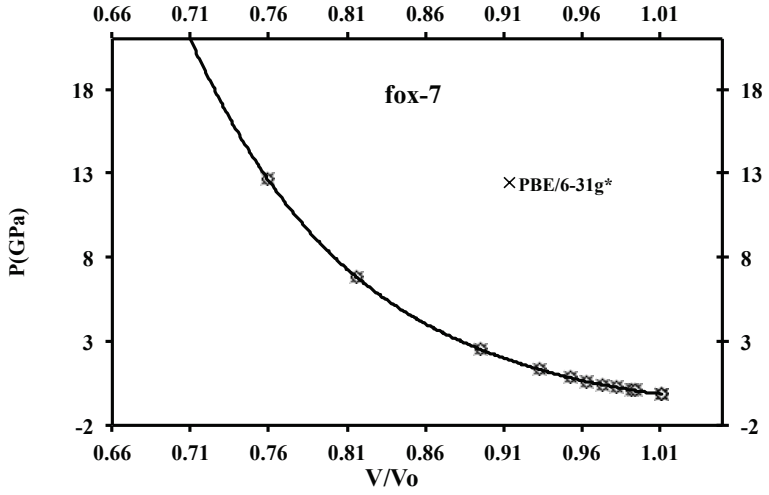

Figure 4.4 Equation of state. System: Fox-7.

Equations of State

We now proceed with the description of equilibrium properties from calculations with atom centerd basis functions. At each state, relaxation of the atomic positions is achieved through optimization of the ionic degrees of freedom; cell shape is optimized through the corresponding cell parameters. The total energies for each system at a given strained volume were used for fitting through the Birch-Murnaghan[292] equation of state [350] from which one can infer the equilibrium volume, V_o, bulk modulus at zero pressure, B_o, and derivative of bulk modulus, B_o', with respect to pressure. Figure 4.4 shows the equation of state for the syste: fox-7.

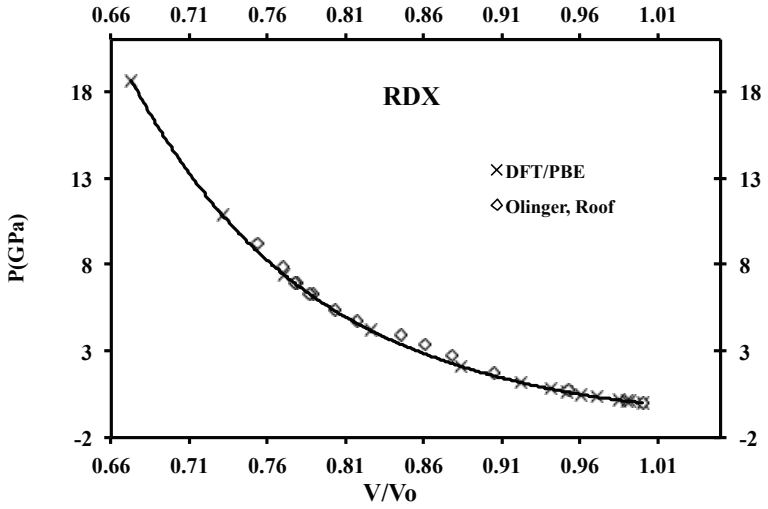

Figure 4.5 Equation of state. System: RDX.

The obtained equilibrium volume, 525 Å^3, compares witht the experimental value of ca. 510 Å^3. For RDX, we find an equation of sate (Figure 4.5) and equilibrium volumes that compares to the previoulsy reported experimental data of Ollinger and Cady. In this case the corresponding equilibrium values are 1699.5 Å^3 vs. 1633.7 Å^3.

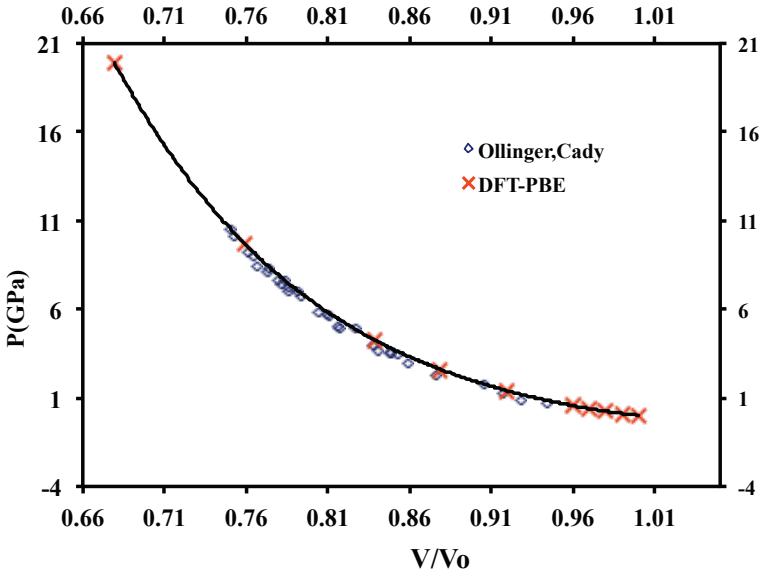

Figure 4.6 Equation of state. System: PETN.

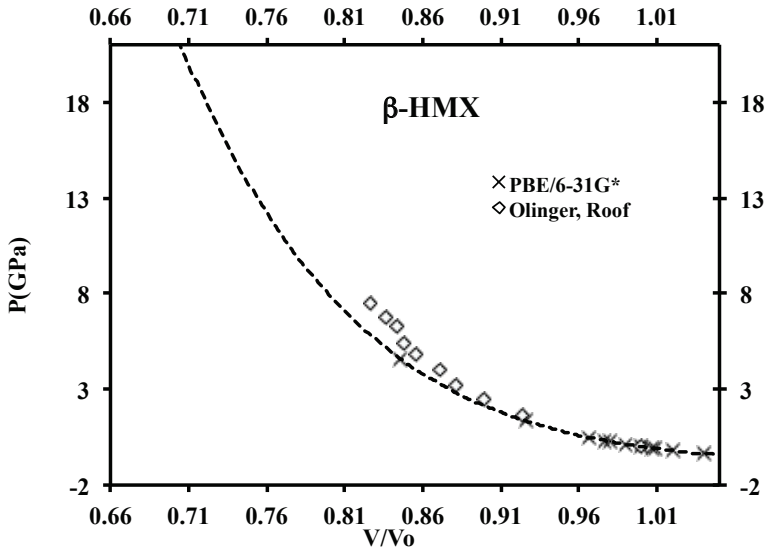

Figure 4.7 Equation of state. System: β-HMX.

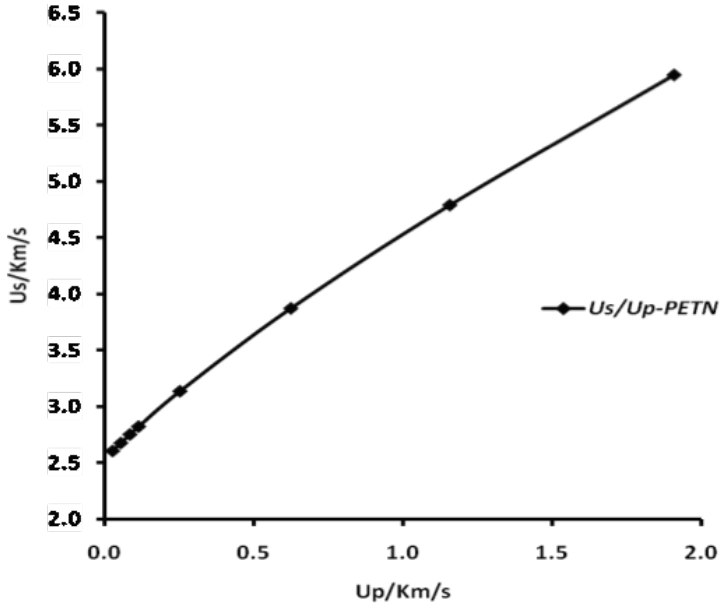

Figure 4.8 Particle/shock velocities behavior. System: PETN.

We have introduced the use of the expansion to the forth order, wich allows for an ample range of volumes to be studied, summarizing the values of the systems: PETN, (Figure 4.6), β-HMX (Figure 4.7), and NM can be seen in Table 4.13

Table 4.13 Equilibrium properties obtained from EOS. Equilibrium volume (Vo), bulk moduli (Bo) and pressure derivative of the bulk moduli (Bo') reported.

	Vo(Å^3)	Bo(GPa)	Bo'
NM	290.83	8.22	8.44
PETN	595.46	11.26	10.28
β-HMX	530.51	10.81	8.44

Since the data is obtained at a constant temperature, we can call the coordinate axis isothermal shock velocity and isothermal particle velocity. A fit to the data, can give information about the sound speed in the system, and from there, we can obtain the particular bulk modulus. For the particular case of PETN, we have calculated a value of 11.26 GPa (Figure 4.8), which compares to the experimental value of 9.4 by Cady, et al[162].

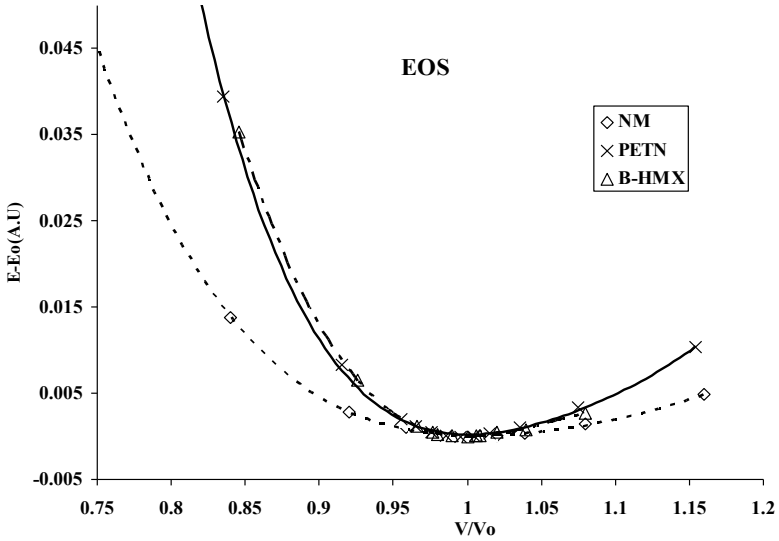

Figure 4.9 Energy versus strained volume parameter for some EM.

Since we have found good correlation between the equilibrium data found experimentally, and the values obtained from our model[284], we can further proceed to use for the calculation of other relevat information.

For materials in which cohesive forces in the crystal unit cell are mostly covalent, (as opposed to weaker dispersion forces), usually the equation of state is sufficient to predict phase changes and their relative stability (Figure 4.9). We will now embark to understand the effect of temperature and extreme conditions on the sensitivity of energetic materials.

CHAPTER V

SENSITIVITY AND ANISOTROPY*

The Advantage of Modeling

Applications for secondary energetic materials (EM) range from initiators in safety bags to detonation charges, propellants and secondary explosives. It has been found experimentally that these materials may undergo detonation by un-planned stimuli. It is well known that high EM's display anisotropic sensitivity to heat and/or mechanical shock [4-6]. Naturally, this has raised serious issues associated with safety, logistics, and time burdens related to handling of these materials, as well as the cost associated with these issues. To understand their behavior, various physical and chemical correlations have been proposed [351,352]. Properties like the number and positions of the substituents, bond length, and partial charges of the molecular constituents in the gas phase, have been used to correlate the trends in sensitivity of these mostly nitro group containing molecular crystals [353].

For processing of plastic bonded explosives, crystals of EM's are fragmented and compressed with a polymer matrix binder. Initiation is usually achieved by means of adjacent primary energetic materials. Thus, localization of strain energy on the EM's has been the suspect of the formation of reaction zones[23], or "hot-spots". A clear understanding of the relevant mechanical properties is essential. In addition to this, compression along a given plane can act as energy barriers and hinder a complete

*Adapted from: Ojeda, O.; T. Cagin, "Anisotropic Behavior Of Energetic Materials At Elevated Pressure And Temperature" *Journal of Loss Prevention in the Process Industries* **2011**, DOI: 10.1016/j.jlp.2011.06.006. Copyright by Elsevier Science.

reaction, causing runaway reactions and unexpected behavior[354]. In this sense, observed reactivity and sensitivity of an explosive is influenced by interplay between mechanical, chemical, and thermodynamic conditions. The prerequisite for the prevention of unexpected behavior while processing of EM's is to understand the phenomena at the molecular level, which requires assessment beyond empirical correlations.

Before any bond breaks and reactions occur, an orbital has to get polarized and charge localization increases at certain group atoms or chemical groups. Molecules interacting with each other, as in condensed phase, can give rise to charge localization not observable for the same isolated molecule. Even though there are numerous attempts to correlate the electronic properties as calculated from gas-phase and quantum chemical studies [49,75,77,84,139,266,355-357], studies that relates charges in molecular crystal at different conditions are scarce [310,358,359]. In case if only the gas phase studies used in correlations, the results will be in contradiction with observed experimental trends[139].

First principles based computational methods (ab initio quantum chemistry, density functional theory, molecular dynamics with accurate interaction potentials) are shown to be suitable to study different thermodynamic properties [360,361] at multiple length and time scales. This enables researchers to employ 'virtual experiments' to study the energetic behavior and crystallographic phase changes at elevated temperatures and pressures without the risk of exposure to unsafe conditions. For instance one can study the highly reactive molecular crystals at the ground state through the use of density functional theory (DFT)[97] . One can include the effect of temperature and pressure through the use of molecular dynamics (MD), employing time averages over the trajectory to determine

thermodynamic properties. More specifically, DFT can also be used to determine pressure dependence of second order elastic constants, variation in charge localization under the influence of applied pressure or anisotropic mechanical loads, such as in response to uniaxial compression or applied shear stresses. More specifically MD is valuable to obtain molecular level information under extreme conditions such as shock or hypervelocity impact where fast evolution of thermodynamic states need to be observed and assessed within short time scales [362].

Herein, we present a systematic study of the mechanical properties as a function of external pressure for nitromethane (NM) and pentaerythritol tetranitrate (PETN), which have distinct impact and shock sensitivities [8,363]. For example, PETN has a reported impact sensitivity which ranges between 12 cm and 27 cm (height for 50% chance of detonation) in drop hammer tests [8], as compared to a value higher than 320 cm for NM. PETN is known to be moderately sensitive to shock compression, while NM is sensitive to shock detonation. We will attempt to correlate these properties with overall thermodynamic behavior using DFT and MD methods. The main objective is to find information at the different level of theories employed, and compare and contrast system related information on the processes that could lead to unsafe behavior. By means of localized basis sets that are used to represent all-electron systems, we performed first principles calculations on the crystals of PETN and NM. These calculations are conducted within DFT[97] level, with gradient corrected Perdew-Burke-Ernzerhof (PBE) functional for exchange and correlation[98]. For these calculations we use extended basis sets[105] for carbon, hydrogen, nitrogen and oxygen, as implemented in the crystal06

package[106]. Initial structures for these crystals are obtained from the Cambridge Crystallographic Database[107]. Energy convergence was found for a mesh of 4x4x4 grid size used for inverse space sampling. Analytical gradients are used to relax the ionic degrees of freedom[364,365] at different strained states.

An important part of the model used to represent properties and processes in nature lies in the level of accuracy and precision of the employed methods. The most common Gaussian or atom-localized basis sets of current use are the split valence basis sets [366-368]. Quality of our basis sets have been validated by a set of calculations on the molecular crystal of urea[369] and other molecular crystal with known binding energy (BE) or sublimation enthalpy. One has to avoid the use of too few functions, which leads to drastic errors in reproducing experimental properties. Another effect to consider is the superposition of basis sets from neighboring atoms (BSSE); this is reduced if a large enough basis is used. We have employed three different type of sets; Ahlrichs' triple-split valence (TZP) basis set[370], the 6-21G basis and our modified 6-31G* basis. For the latter two basis functions, the first digit indicates the number of Gaussian functions that represent core atomic orbitals, and the last two indicate the number of functions used for the valence orbitals. The TZP basis set is the largest one of the three sets employed here.

Table 5.1 Formation energies from different basis sets. Urea crystal. Total energy reported in atomic units. (A.U.).

Basis Set	Energy/A.U.	V_0/Å^3	BSSE/KJ/mol	BE/KJ/mol
6-21G*	-449.7130153	136.345	97.05	-96.94
6-31G*M	-450.2513153	145.137	41.00	-98.48
Ahlrichs	-450.0698772	156.486	7.94	-88.38

Full optimization with the different basis sets was performed. The results summarized in Table 5.1. Energies are reported to the last digit of the imposed tolerance for each self-consistent cycle ($1x10^{-7}$). V_0 stands for the equilibrium unit cell volume in $Å^3$, as calculated by relaxing all the cell and ionic degrees of freedom. The BE of the urea crystal was estimated to be -98.48 KJ/mol, which compares well with the experimental[371] sublimation enthalpy of -94.3 KJ/mol. From BE values, we see a basis set that reproduces qualitatively the experimental result. The BSSE lies between that of a contracted 6-21G* basis, and the more expensive Ahlrichs basis set.

For calculations with localized basis sets, the effective pressure values corresponding to each compression value is obtained by fitting the results to a widely used Birch-Murnaghan (BM) equation of state [372]. The fourth order BM equation of state has the following form;

$$P / B_o = 3f(1+2f)^{\frac{5}{2}}[1-\frac{1}{2}(\frac{\delta_3}{\delta_2})f+\frac{1}{6}(\frac{\delta_4}{\delta_2})f^2+....] \quad (32)$$

Where;

$$V / V_o = (1+2f)^{-\frac{3}{2}} \quad (33)$$

And;

$$\frac{\delta_3}{\delta_2} = 12 - 3B_o^{'} \quad (34)$$

$$\frac{\delta_4}{\delta_2} = 9B_oB_o^{''} + 9(B_o)^2 - 63B_o^{'} + 143 \quad (35)$$

This equation of state allows for larger range of volumes, pressures and other thermodynamic properties to be correctly predicted. Here, V is the unit cell volume at a given thermodynamic state, B_0 stands for the equilibrium bulk modulus at zero pressure, while B_0' and B_0'' represents the first and second derivative of the bulk modulus.

In order to obtain the anisotropic mechanical properties (namely the second order elastic constants) for NM and PETN, we use the finite strain method. By applying finite strains to the crystallographic unit cell, a new cell structure (representing the strained form) is obtained. The difference in energy (strain energy) can then be computed in terms of a polynomial expansion in strain tensor [373];

$$E - E_o = V_o s_{ij} e_{ij} + \frac{V_o}{2} c_{ijkl} e_{ij} e_{kl} + \ldots \qquad (36)$$

In this case, E_0 is the reference ground state energy, or the energy of zero-strain state; e_{ij} and e_{jk} are the Cartesian strain tensor components. The stress tensor components are s_{ij}, and c_{ijkl} is the elastic constants tensor. The first term vanishes in a zero-strain state. We can determine the corresponding elastic constants c_{ijkl}, by applying specific strain states to the reference system. Owing to the symmetry of the elasticity tensor[374], and to simplify, we employ the contracted "Voigt" notation; replacing the Cartesian tensor indices by Voigt indices: 11=1, 22=2, 33=3, 23=4, 31=5, and 12=6, for stress, strain and elastic constants. The second order elastic constants, C_{IJ} are then given by the second derivative of the strain energy with respect to the total energy as:

$$C_{IJ} = \frac{1}{V_0} \frac{\partial^2 E}{\partial \eta_I \partial \eta_J} \qquad (37)$$

In this expression the symmetric finite strain tensor components are now replaced by the 6-dimensional vectors: h_i and h_j. Fitting the strain energy calculated for each applied strain to a second or higher order polynomial then enables us to obtain the corresponding second order elastic constants. The number of independent elastic constants is determined by the symmetry of the crystallographic system. The resulting elastic constants represent the anisotropic response of the crystal to mechanical stimuli. We obtain them by using a total of 6 equally spaced strain values, in addition to the reference or 'unstrained' state, and up to a value of 3% of maximum tensile and compressive strain. For the case of empirical corrections to the DFT energy we employed an estimation of dispersion or 'C6' coefficients through a parametrization based on atomic polarizabilities (D-DFT). We refer the reader to specialized literature [304,315,325,326,375].

Additionally, MD calculations have also been performed. Whenever force field assigned atomic charges were not available, the charges are determined from the Charge Equilibration (QEq) method[131]. For these simulations with the Isothermal Isobaric ensemble (NPT), the codes LAMMPS[133], Cerius2, and Materials Studio have been used. An equilibration time of at least 400 picoseconds (ps) is required for all the runs, with the averages taken over 200 ps long samples of a MD simulation with an integration step size of 1 femtosecond (fs). Nosé-Hoover thermostats and barostats are employed [376,377]. Information at the different simulation scales approached here will be correlated with experimental data, when available.

Mechanical Properties

Here, we analyze in detail the energy vs. volume behavior of primitive unit cells of NM and PETN, composed of 4 and 2 molecules, correspondingly. A discontinuity in the energy-volume curve of NM is observed in the corresponding pressure value of 3.5 GPa, or 220 $Å^3$, see Figure 5.1. Upon transition to this state, there is a change in volume close to 20 $Å^3$ or 10% reduction. Additionally, a change in the point group symmetry to $P2_1$ (Table #4) from P_{212121}, after the transition at 3.4 GPa is found. The pressure behavior of the elastic coefficients was obtained. We still observe a transition with a larger inverse space integration grid of 6x6x6 rather than the earlier 4X4X4 grid. The discontinuity is found close to a hydrostatic pressure value of 3 GPa (Figure 5.2). The predicted bulk modulus and equilibrium volume for NM, as obtained from localized basis set calculations, are found to be 288.6 $Å^3$ and 9.95 GPa. They compare to the experimental values[363] of 285 $Å^3$ and 10 GPa.

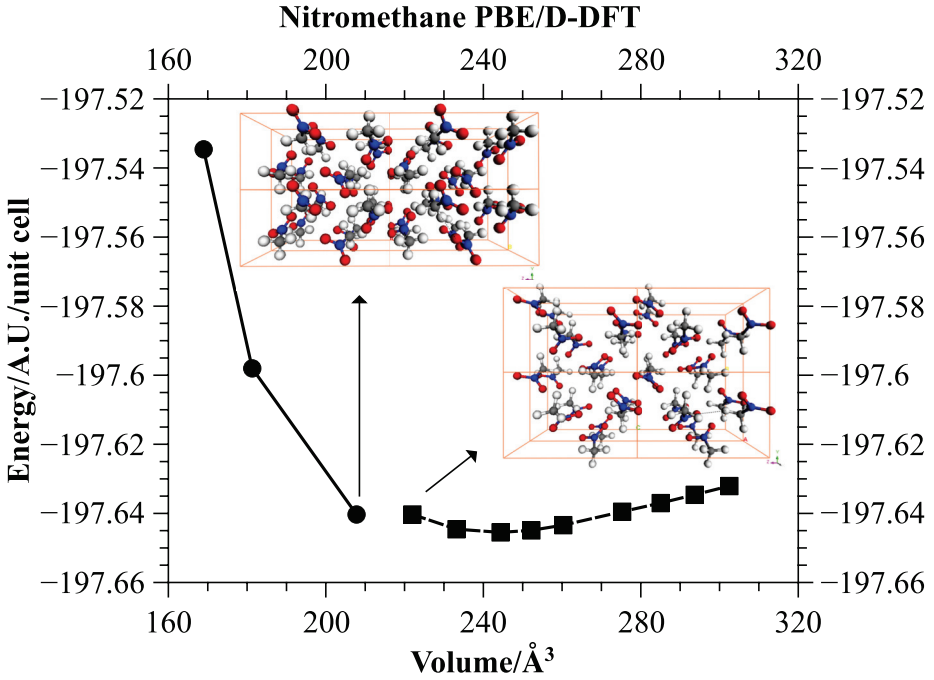

Figure 5.1 Energy vs. volume curve for NM.

The bulk modulus of PETN is in agreement with the ones found experimentally by Ollinger and Cady[162], with values of 11.36 GPa vs. 9.4GPa. We found good agreement with their calculated values, as well as in the V_o (592.73 Å^3 vs. 574.64 Å^3).

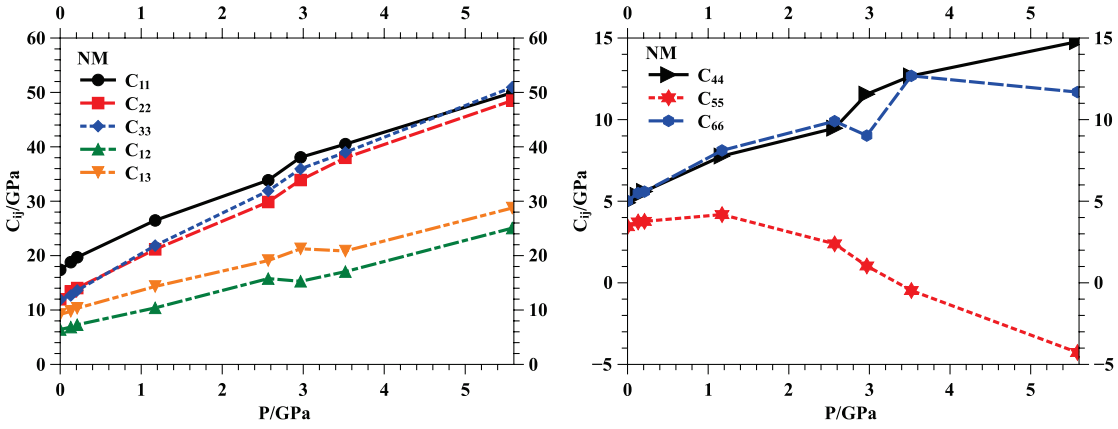

Figure 5.2 Elastic stiffness coefficients of NM. The observed discontinuity ca. 3 GPa can be observed in elements C_{11}-C_{13} (left), as well as in the shear constants C_{44}, C_{55}, C_{66} (right).

As opposed to NM, PETN does not show any mechanical instability, as observed from its behavior for compressions up to 6 GPa. This is shown in Figure 5.3. Considering, the typical impact tests pressures in the 1 GPa range, and shock or flyer plate test expriment pressures of 3 to 7 GPa, the discontinuity would be obseved close to a shock compresion. The bulk modulus as obtained from the Voigt average of the individual anisotropic elastic coefficients (11.79 GPa) in very close agreement with the one obtained from our 4th order BM equation of state (11.36 GPa).

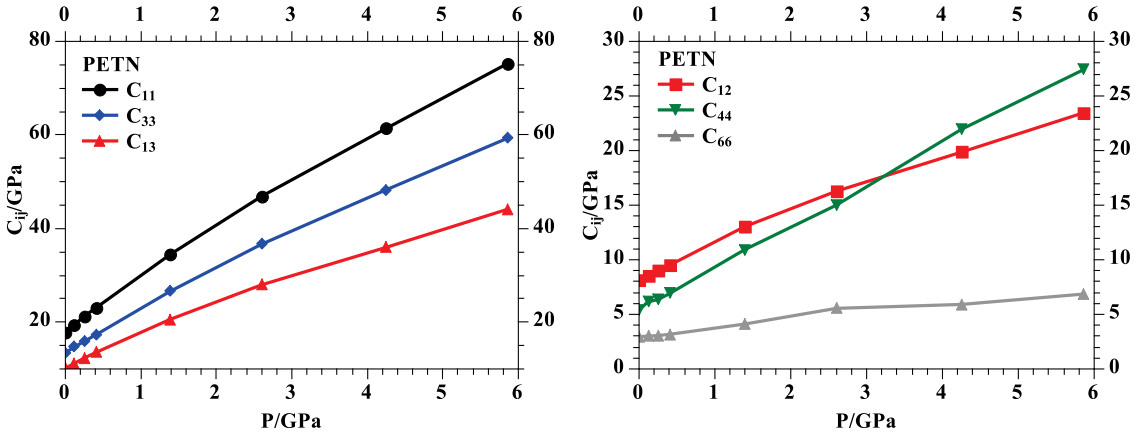

Figure 5.3 Changes in the elastic stiffness coefficients of PETN.

The particular behavior of a system, as it relates to directionality in its properties, are referred as anisotropic properties. Understanding the mechanical properties is required, since localization of strain energy has long been the suspect of the formation of reaction zones[23], or “hot-spots”.

Table 5.2 Second order elastic constants of fox-7. Values are in GPa. Volume in A^3.

C_{ij}	Fox-7
C_{11}	37.56
C_{22}	19.79
C_{33}	46.60
C_{44}	0.5
C_{55}	27.01
C_{66}	4.19
C_{46}	-0.31
C_{35}	12.83
C_{25}	-1.29
C_{15}	-3.15
C_{23}	7.01
C_{13}	11.92
C_{12}	14.24
V_o	510.817

Uniaxial Compression, Ground State

Localization of energy and the corresponding formation of hot spots by compression along particular crystallographic planes can be estimated by the changes in energy observed under uniaxial compressions. Further more, a Mie-Gruneissen type[17] of relationship, (eq. 38), can help understand the exponentail dependance on the rate of a reaction, as observed from the changes in energy in a partucular direction of compression[17].

$$P - P_1 = \frac{\gamma(V)}{V}[E - E_1(V)] \tag{38}$$

$$T = T_0 \exp\left(\int_{p_0}^{p} \frac{dP}{\frac{\partial E}{\partial V} + p}\right) \tag{39}$$

At elevated temperatures, we have mapped out the stress-strain behavior of the energetic material PETN, for which a phase change ca. 8GPa has been reported. The deviation from a continuous or monotonic change indicates a highly an-harmonic behavior. These results can be observed in molecular crystals, since molecular packing and geometry changes are possible through changes in bonding, torsion and dihedral angles for attaining the lowest enthalpy state of the crystal under applied pressure/stress unlike other materials like metals or ceramics.

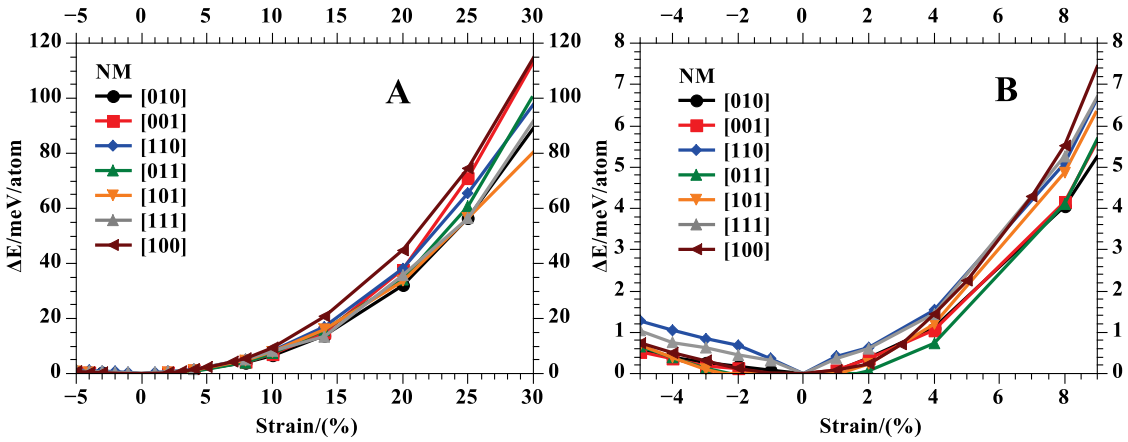

Figure 5.4 Uniaxial compression of NM. Complete range of anisotropic strains studied (A). Results of strain comparable to values smaller than 10 GPa (B).

For both systems, we found a drastic change in the energy of the system when compressed to 25% of its original volume. Notice the anisotropy found by comparing energy difference at the maximum strain values in Figure 5.4 and Figure 5.5, we observe the uniaxial compression of NM and PETN, within quantum level DFT calculations. For both systems, there is a region of steep energy change, below 1% strain values. After

this, different planes behave differently, in terms of the energy required for compression. This is also an indication of the energy that will be released when a relaxation to initial conditions occur.

At the highest strain value studied here, for NM (Figure 5.4), the <001> and <100> show the largest energy change, by almost 10 meV per atom, when compared to the other planes. Below 9% strain, the <111>, <110> and <101> directions show higher energy differences when compared to the other planes. For this strain level the largest energy differences found between the [100] plane and the [010] plane, which is now smaller than 2 meV/atom. For PETN (Figure 5.5), the [010] plane has a higher energy difference of ca. 50 meV/atom as compared to the [001] plane.

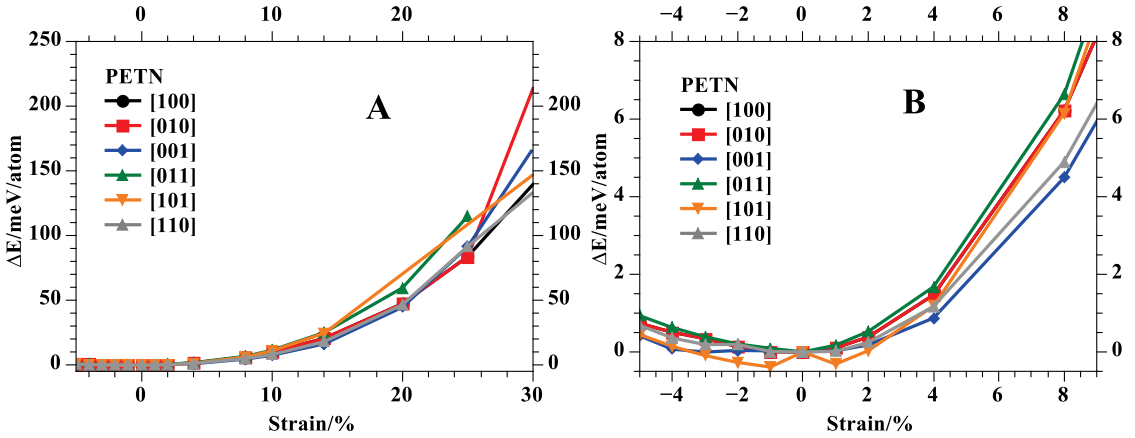

Figure 5.5 Uniaxial compression of PETN. Complete range of anisotropic strains studied, (A). Results of strain comparable to values smaller than 10 GPa, (B).

In contrast, at a compression value close to 8%, the <110> and <001> uniaxial compressions energy differences are below ca. 1 meV/atom, as compared to the rest of the high symmetry directions.

We have previously shown the electronic structure for PETN, b-HMX, and NM, including the corresponding adiabatic uniaxial compression energetic behavior in the ground. We found a marked anisotropy, in particular for β-HMX [303].

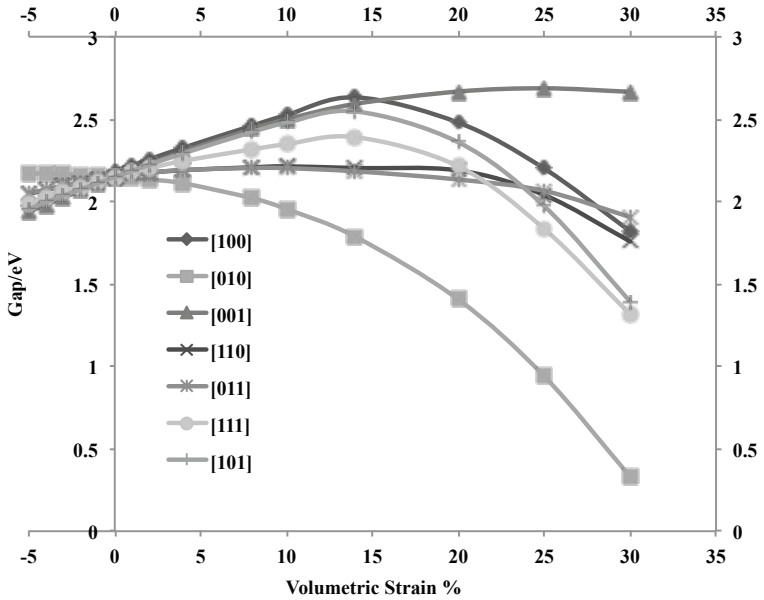

Figure 5.6 Uniaxial compression of Fox-7. Compression along <111> ,<101>, <100>, and <001> show an initial increase in the band gap value, for adiabatic compresions. Compression along <010> indicates a marked reduction of the band gap value upon compression.

With regard to Fox-7, Kimmel and Kuklja have reported the effects of exited states and hydrogen transfer[54,378] in the decomposition of Fox-7, We have found that there is indeed a marked anisotropy upon compression through high symmetry planes of Fox-7 (Figure 5.6). Upon closer inspection to the structures in the compressed states along [010] plane, shows closer contact among molecules. Near-Fermi conduction bands are

observed, from the electronic band structure calculation at the most compressed (30% Vol) state (Figure 5.7). A characteristic observed in quasi-metallic systems. This indicates a metallization upon compression for this system cannot be ruled out.

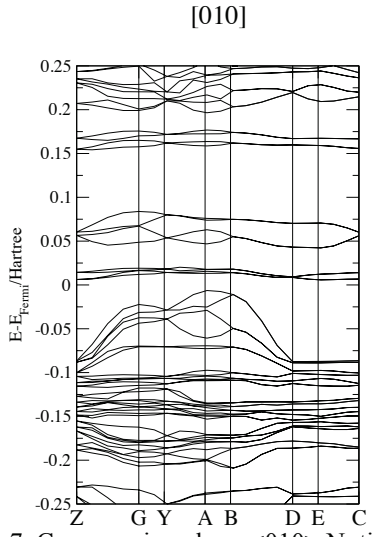

Figure 5.7 Band structure of Fox-7. Compression along <010> Notice the band Gap closening at 'B'.

Charge Behavior

Since it is commonly assumed that the first step in the initiation of the nitro aliphatic and ester nitrates through the bond breaking (homolitic) of the R-NO and RO-NO_2 groups, we investigate the changes in formal charges measured from Mulliken charges using overpopulation analysis. The formal charge, as obtained from the atomic number minus the overpopulation in the particular atom, is calculated for the systems under consideration (Figure 5.8, Figure 5.9). We observe that the behavior is highly anisotropic, with the values of initial charges differing in the highest compressed state. For the nitro group of the PETN crystal, the largest change in polarization can be observed for <111>, at the maximum strain value of 30%. The polarization for this

family of planes is also observed from the ester oxygen atom and the ester carbon atom, with a maximum close to 20 % strain.

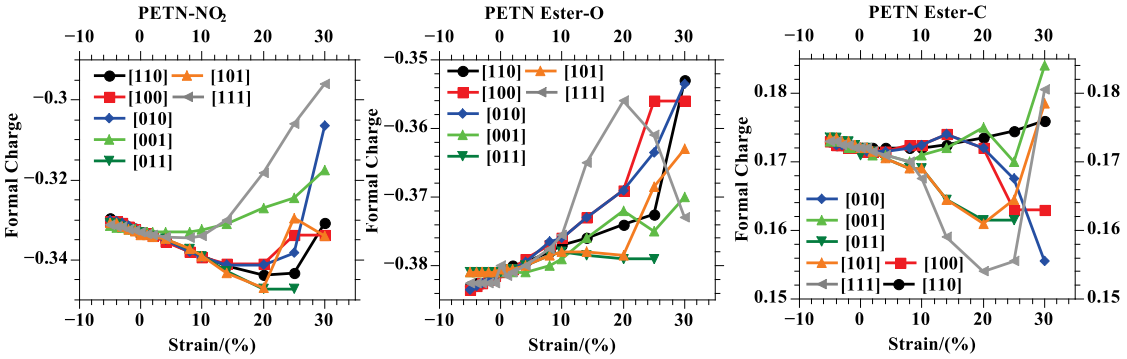

Figure 5.8 Change in formal charge of PETN. Nitro group, top left. Ester oxygen, center. Ester carbon, right.

For NM, we observe an interesting behavior for the charge of the nitro groups, as the crystal is strained along the [111] direction (Figure 5.9). In this case, the maximum occurs at strain values close to 15%. The charge of the nitrogen atom, shows the largest change in formal charge, when compressed along the [001] plane, for values larger than 25% strain.

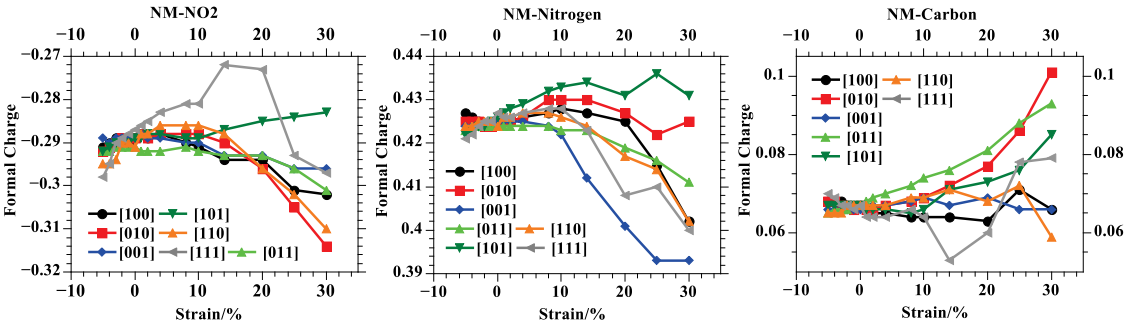

Figure 5.9 Change in formal charge of NM. NO_2 group, left. Nitrogen, center and carbon, right.

Effects of Temperature and Pressure

At elevated temperatures, we have mapped out the stress-strain behavior of the energetic material PETN (for which a phase change ca. 8 GPa has been reported). This is done by generating data on a multidimensional grid of stress values along unique strain directions, based on crystal symmetries. Starting from a slow heating of a 4X4X6 super-cell from 50 K to 300 K, where we equilibrated the system for over 10 ns. The Molecular Dynamics simulations show curves that differ drastically from an expected uniform/isotropic behavior. From finite temperature evaluation of the equilibrium volumes, we obtain a unit cell of 289.90 $Å^3$ at 150 K for NM, and a value of 657 $Å^3$ at 300 K for PETN. Although our model over-estimates V_o for both NM and PETN, they are comparable to reported values ca. 285 $Å^3$ and 630 $Å^3$ correspondingly [164,379].

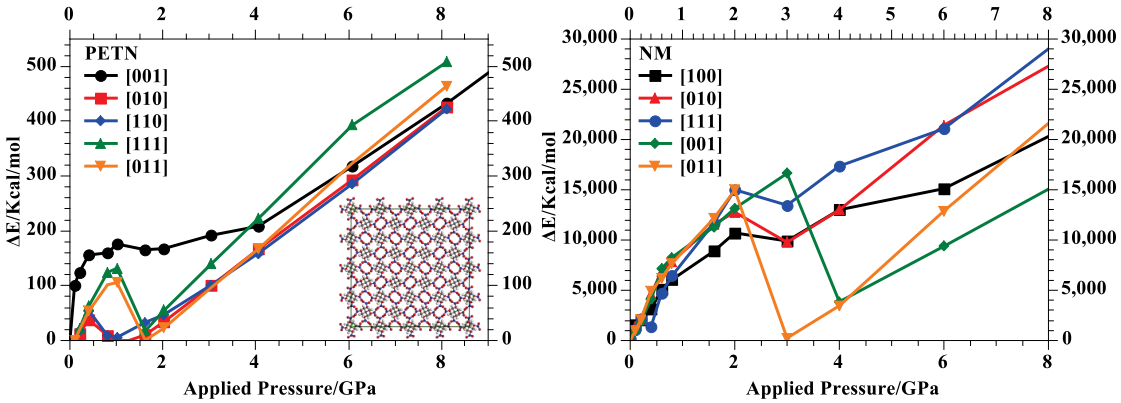

Figure 5.10 Changes in the total energy for the PETN supercell (inset, left). Enthalpy changes for NM (right).

In Figure 5.10, we present the changes in enthalpy and internal energy, at different applied external stresses for the studied systems**.** In both cases we see a change in the

slope of the energy change, along particular directions. For the case of PETN, we observe that the <001> direction shows an interesting behaviour since it reaches a plateau after 0.4 GPa, in which there is a small change in energy up to 1 GPa. In contrast, the changes in energy in the <010> and <110> directions show a change in curvature after the vaule of 0.4 GPa. A changes in the structure of the PETN molecules along this crystallographic plane is expected. For NM, this ocurrs near pressures of 2 GPa, while for PETN this occurs for pressures close to 1 GPa and smaller.

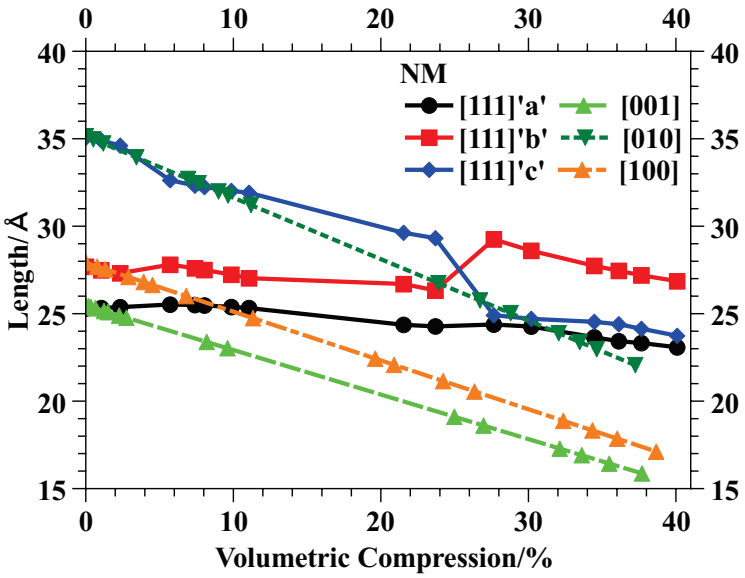

Figure 5.11 Changes in lattice parameters for NM.

For NM, the most dramatic changes in enthalpy occur for the <111> and <001> directions. In addition to this, there is a discontinuity, in both enthalpy behavior and lattice parameters upon compression for the <111> direction (Figure 5.11). Volume change is larger for this unaxial compression.

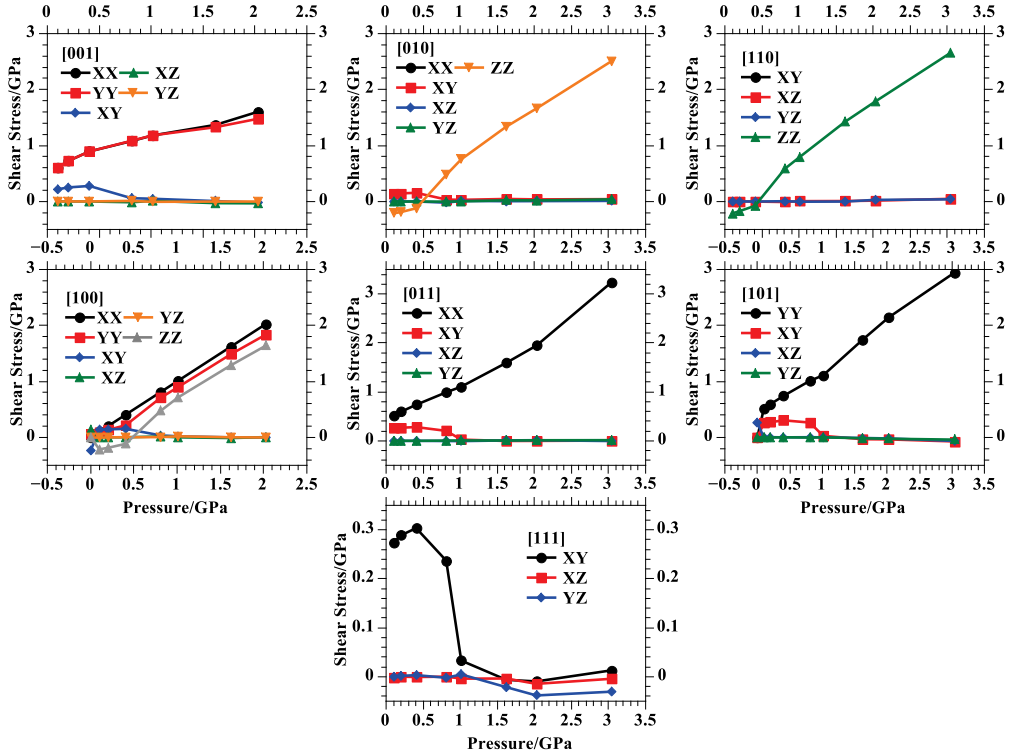

Figure5.12 Shear stress for different applied uniaxial compressions on PETN. Values up to 3 GPa.

Applied uniaxial stresses could lead to localization of stress, in the form of shear stresses that develop upon compresison for the PETN system (Figure 5.12). The <111> direction shows no increase in shear stresses upon application of uniaxial loads in this compression direction, for PETN. We notice that for this insensitive 111-direction, there is almost no stress increase. In the case of <010> this strain is not symmetric, indicating that the original point group of the system is not favored upon compression. There are tensile shear stresses in <010> and <110> directions. The total increase of stress is larger along 'c' axis when the system is compress in the sensitive [110] plane. For NM, asymmetric buildup of shear stress is found for [001] and [100] planes, which also show the largest change in enthalpy upon axial compression (Figure 5.13). We find shear

components in XX, and YY for the case of <001>, and components in XX, YY and ZZ for <100>. Interestingly enough, there is almost no shear build up for the system when is uniaxially compressed in the [111] direction. The fact that the system undergoes mechanical instabilities after 3 GPa could indicate a difference in the mechanism for the impact and shock sensitivities in NM.

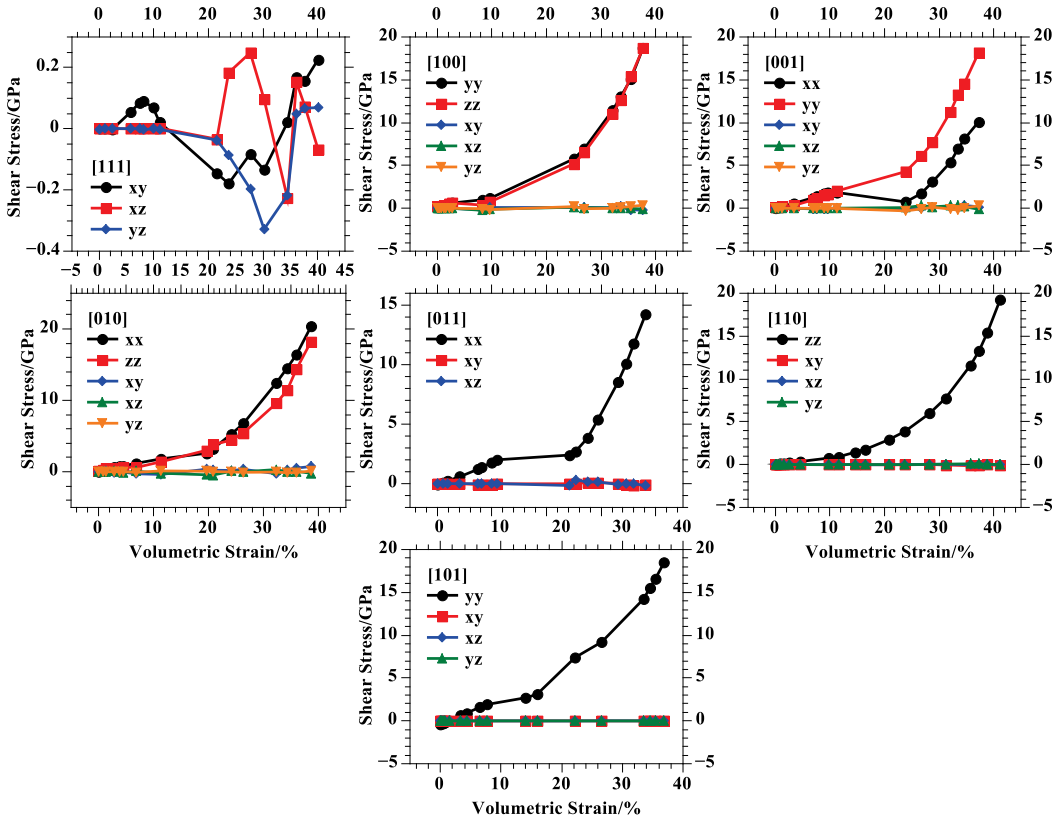

Figure 5.13. Shear stresses for different applied uniaxial compression: NM.

Cortecuisse[380] proposed four solid phase transformations in NM up to 25 GPa. Citroni[381] found a phase change after 6.5 GPa, where he cited an increased hydrogen bonding interactions, and a predominant eclipsed conformation of the nitro group with respect to the methyl group. From our calculations, changes in both symmetry and

elastic coefficients indicate that for pressures below 5 GPa, there is phase transformation. This can also be supported by the observed changes in the lattice parameters at elevated temperatures. From a closer inspection of the structure before and after the transition, we find a change in the oxygen interaction of the nitro group with the adjacent molecular hydrogen.

We observed a discontinuity from the pressure dependence behavior of the elastic properties above 3GPa. Nonetheless noted for the uniaxial compression in the [111] plane direction[382], and in earlier diamond anvil-cell (DAC) studies [159], this type of behavior has not been reported in other MD simulations or hydrostatic compression studies. Departing from normal conditions, we observe that there is a discontinuity in the enthalpy pressure curves for NM, a system that is sensitive to shocks but insensitive to impact. Dick[5] has proposed the [001] direction is the most sensitive, although no uniaxial DAC was possible. Piermani [383] reported sensitivities at 3 GPa with the <111>,<100> and <001> directions. White[382]found greater shear stresses in the <111>, <001> and <011> directions. Although indications of sensitivity for the [100], [111] and [001] planes for NM have already been reported [159,381,382,384,385], our results give insight as to what is the mechanism for sensitivity for each crystallographic direction. Although no available data on the elastic constants were available, the higher sensitivity along the [001] direction[5], is supported by the changes in enthalpy observed from the uniaxial compression runs at 150 K, and from the larger change in total energy from calculations in the limit of 0 K. As expected, due to its low impact sensitivity, the NM system can undergo a monotonic change in enthalpy at low pressures/compressive uniaxial strains.

At higher pressures, the shock sensitivity can be observed by the drastic change in enthalpy for the [111] direction, and increase shear pressure for the <001> direction, below 4 GPa. Furthermore, the changes in mechanical properties and phase transition, could explain the difference observed between shock and impact sensitivities found from different studies.

For PETN, Soulard[386] observed reactive wave profiles in <001> and <111> crystals up to 5 and 11 GPa. Dick[4] Classified the <001> and <110> as sensitive based on wedge experiments. At higher compressions, we see a change in the electronic structure, as measured from the formal charges of the atoms involved in the initiation step for homolytic bond rupture. The formal charge of the nitro group and carbon atoms varies dramatically for the highest compressed state. This indicates that for the extreme compressed states, initiation can me more easily achieved in preferential directions.

DFT calculations of uniaxial compression along the [010] direction showed the largest energy difference, in the highest strain values studied here. When the effects of temperature are considered, this plane and the [001] plane has displayed non-monotonic behavior. In spite of the anisotropic behavior with the applied external stress, the mechanical properties of PETN show no discontinuity or a drop to negative values up to pressures ca. 6 GPa. In comparison with NM, we can expect a PETN system to be mechanically stable after the pressure of 4 GPa is reached, either by processing or in a controlled application, whilst NM will not. Planes along [111] and [011] showed an inflexion at pressures as small as 1 GPa, which is in line with the observed impact sensitivity. As expected for both cases there are a larger polarization in initiation bonds,

at different pressures, and directions. Changes in the formal charge can be observed for different values of uniaxial strain, which indicates that at different compressions (impact, vs. shock) the chemical environment of the strained system is highly anisotropic. In addition to the reduction of associated cost and safety issues on particular processes that are difficult to study experimentally, we present computational methods than can be used to predict the behavior of materials exposed to extreme conditions. Here we claim that these methods can give an intrinsic advantage, when effort for appropriate parameters and accuracy are met. We have observed that NM, which shows a crystallographic phase transformation and a drastic behavior of its elastic coefficients, as opposed to PETN, which is observed to be mechanically stable in the studied pressure range. Nonetheless, the effect of elevated temperatures and pressures might provide more insight into their behavior under compression. These studies further have revealed the anisotropic behavior of the studied systems. Further studies that gather information at the chemical, mechanical and thermodynamic level can be applied to the understanding of other type of systems, of lower sensitivity, or even materials, for which unknown sensitivities are of concern. We will focus our attention now to TATB, an insensitive material, to reveal the molecular properties and structural changes that can indicate a source of its observed experimental behavior.

CHAPTER VI

PECULIAR BEHAVIOUR OF TATB UPON COMPRESSION

Structural Changes

TATB, 1, 3, 5-triamino-2, 4, 6-trinitrobenzene, is an insensitive secondary energetic material (EM)[339,387,388] due to its weak response to impact. This arene substituted molecule has both electron withdrawing and donor groups[389], favors packing in a lamellar arrangement. Experiments indicate changes in its non-linear optical response[390] and microstructure properties of TATB, under thermal or mechanical treatment[110], and an irreversible thermal expansion[391,392]. Besides a general interest for its use in various technological applications[184,353,393-403], a detailed understanding of these changes in terms of molecular level structure and orientations upon compression is of significant relevance. Subtle structural differences can have implications in the stability and properties of the molecules as subjected to external stimuli, such as heat[404] or compression[405]. Therefore, related molecular and atomistic level information[392,406] and its behavior as compared[404] to other type of EM's[284] could also provide hints to the unusual properties[407-409] of this material.

At ambient conditions, the experimental crystal structure reported by Cady[154] has (P-1) symmetry. The unit cell contains two molecules for a total of 48 atoms. Later reports of the structure of TATB from x-ray diffraction studies (XRD) indicated a lack of phase transition when subjected to compression[410]. In line with this observation, some atomistic models[411,412], and other theoretical and *ab initio* calculations[310,413], have also reported

stable planar molecular conformations, with no phase changes in crystal structure. Still, the molecular behavior of the system under pressure has been the subject of debate since earlier studies[414], which have implied the presence of polymorphism[415]. Catalano and Rolon, discussed the difficulties in settling the existence of TATB polymorphs, and reported the presence of a number of solid state products prior its decomposition[416], while Foltz, reported an irreversible change in optical properties of TATB upon compression[417] in a diamond-anvil cell (DAC). More recently, experimental vibrational studies of the system under hydrostatic compression have been reported[388,418], for vibration modes in the range of 100 cm^{-1} to 800 cm^{-1}. These low frequency modes have been proposed as the doorway modes, which correlate with the impact sensitivity[419] of some EM's.

To clarify if any such crystal or molecular transformation upon compression exists, we have performed a systematic study of the crystalline system with pressures up to 30 GPa. In the following, we will present the results our extensive studies on the changes in molecular structure and re-arrangements within this triclinic unit cell under compression.

After a brief introduction of the methods employed, we will describe the observed structural change, its influence on the vibrational spectra[420]. In order to further relating this observation to experiments, we also present calculated x-ray diffraction results. To provide the energetic basis of a simple two state model, we present extensive potential energy surface calculations using *ab initio* quantum chemistry and DFT methods. To reveal the anisotropic response of the model system we also present the calculated elastic stiffness tensor its variation as a function of pressure. We will then conclude by

discussing the implications of our findings and its relation to the behavior of TATB. In order to understand the potential energy landscape of the system under consideration, we have performed *ab initio* quantum chemistry calculations using localized basis sets[108,109] on single TATB molecule and TATB dimer. In these calculations, the Hartree-Fock approximation (HF) and the Möller-Plesset perturbation (MP2) have been employed[111,112]. Density functional theory[97,110] (DFT) calculations with 3-dimensional periodic boundary conditions (PBC) have also been carried out on the TATB single crystal. In this case, the Perdew-Burke-Ernzerhof (PBE) exchange correlation functional[98,100-102] and the projector-augmented-wave (PAW) type potentials are used[103,206]. For securing the accuracy of results an appropriate energy cutoff and inverse space integration scheme[421] with a tolerance for convergence of 0.2 meV per atom were chosen. Furthermore, a tolerance on the convergence of the self-consistent wave function optimization cycle is set to $1x10^{-7}$ eV. In the calculation of elastic properties, we only used the 'Born' term. This is the second derivative of the potential energy with respect to the strain tensor, calculated analytically from the interaction force-fields for organic materials[422]. More specifically, we use the "Dreiding exponential-6" (DREX6) force-field[117], as it has been found to be particularly well suited for the study of molecular systems made up of main group elements. Atomic charges are determined set by the use of the QEq method[130,131], which reliably accounts for the charges as a function of configuration and ionization energies of the particular element. In our X-ray diffraction simulations, we have used an incident radiation of wavelength; 1.54178 Å. Optimization of the cell parameters and fractional coordinates at each applied external stress value is

performed without imposing any restriction on the symmetry of the unit cell. In Figure 6.1, we present the variation of unit cell parameters of single crystal TATB as a function of applied pressure with the values ranging from 0 GPa to 5 GPa. TATB displays a reduction in volume and in three lattice constants (a, b, c), From 0 GPa to approximately 1.5 GPa, all three lattice constants (a, b, and c) decrease with slight differences as expected from the anisotropic elastic response of the crystalline material. However upon further compression, the molecules slightly move from a perfect alignment perpendicular to the 'C' axis, hence reducing the electrostatic repulsion caused by the conjugated π system. This causes a distinct variation in the unit cell parameters; we observe a sharp increase in c- while a- and b- drastically decreases, still leading to a decrease in volume. When the structure before and after this 'transformation' is analyzed; at ambient pressures, perpendicular to the c-axis the hydrogen bonding and in-plane molecular interactions are predominant. As the pressure increased, however, the system responds through a rearrangement by increasing out of plane interactions by establishing a new network of hydrogen bonding (we will further characterize this below). Hence, compared with the original reported ambient pressure structure, there is a "transformation" in the form of a structural rearrangement after a pressure value approximately 1.5 GPa. The molecular layers, originally shifted off the axis, align closer one on top of the other. The net result is a lengthening of the 'c' direction. This is accompanied by reductions in 'a' and 'b' directions, and the total volume of the relaxed unit cell after the transition at a pressure ca. 2 GPa is smaller by 5.1 $Å^3$.

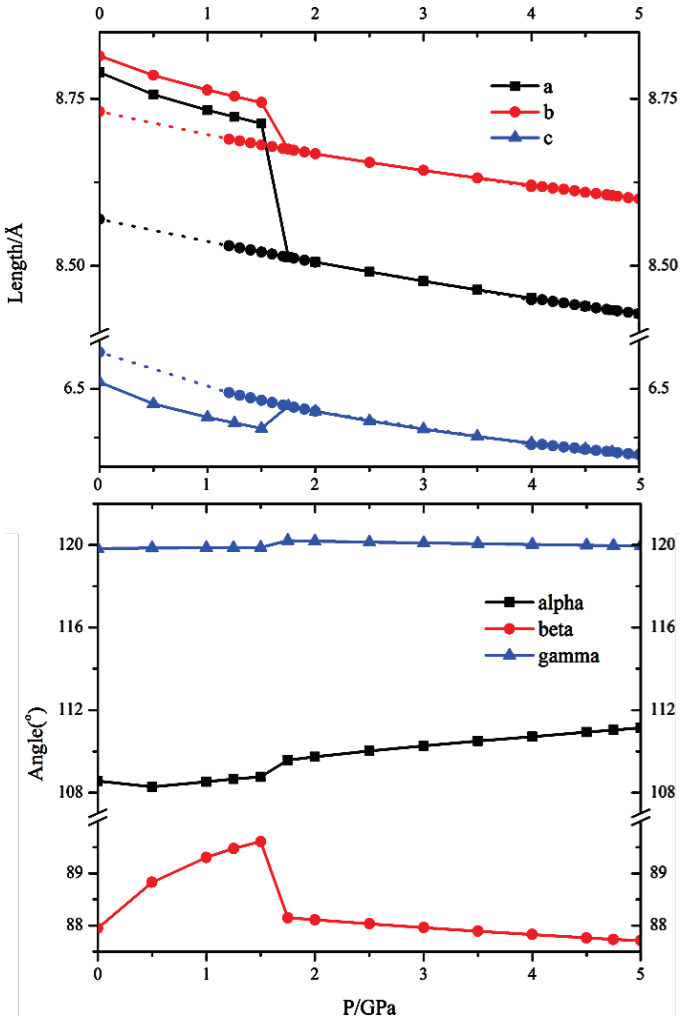

Figure 6.1 Change in lattice parameters upon compression. Compressive loading run (solid line); pressure release run (dotted line).

Vibrational Spectra as a Function of Pressure

To further characterize molecular rearrangement as a function of pressure, we have calculated the vibrational spectra before and after molecular arrangement (focusing between 1.4 GPa and 1.6 GPa). We have evaluated the vibrational frequencies and modes from the hessian matrix.

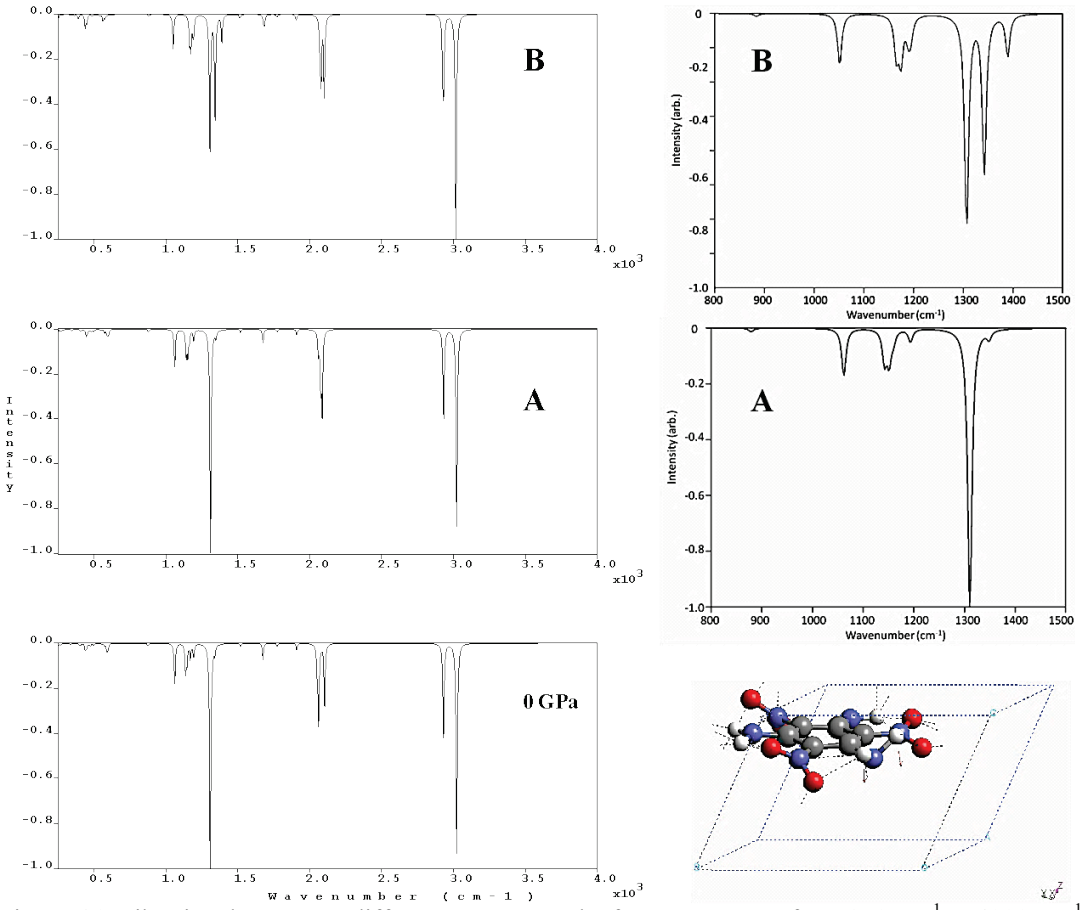

Figure 6.2 Vibrational spectra at different pressures. The frequency range from 250 cm^{-1} to 4000 cm^{-1} is displayed on the left. Range from 800 cm^{-1} to 1500 cm^{-1} is displayed on the right. Spectra at ambient pressure is labeled as '0 GPa'. Spectra before the transition is labeled 'A', while the spectra obtained at a pressure value close to 1.6 GPa, is labeled as 'B'. The bottom right Figure depicts the vibrational mode at 1324 cm^{-1}.

The vibrational spectra of the system under study are displayed in Figure 6.2. In the frequency range from 250 cm^{-1} to 4000 cm^{-1}, we observe differences between the spectra in the range from 0 GPa to 1.4 GPa and 1.6 GPa. There are more notable changes close to the region of 2000 cm^{-1}, and in the region between 800 and 1500 cm^{-1}, (right panel of the Figure 6.2). To narrow down the pressure at which the change occurs, we computed frequencies at 1.5 and 1.55 GPa values. There is noticeable difference in the spectra

obtained at 1.5 GPa, as compared with the spectra at 1.55GPa. In addition to other vibrational maxima appearing, there is clearly a separation of the peak near 1300 cm^{-1}.

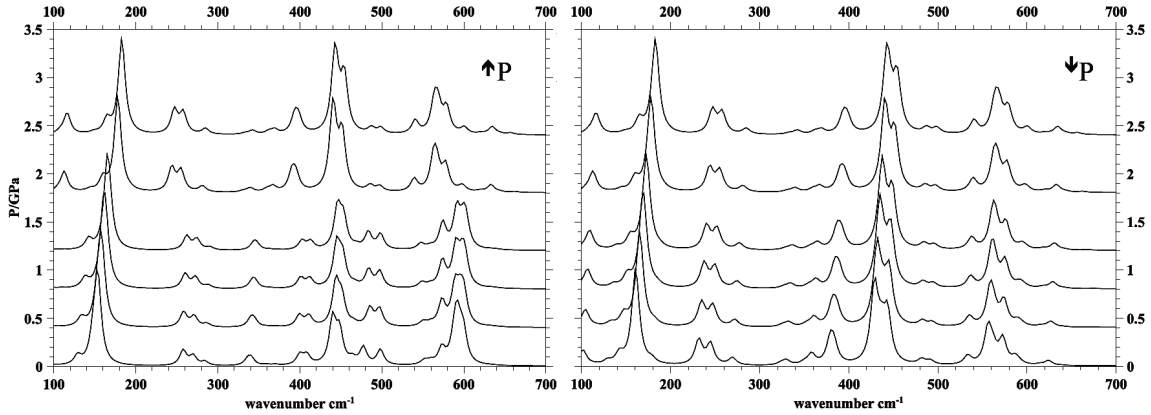

Figure 6.3. Far-infrared section of the spectra. Compression 0 to 5 GPa (left). Notice the irreversible change of different modes, ca. 1.6 GPa. Release 5 to 0 GPa (right). Pressure variation during the simulation depicted as ↑P and ↓P, correspondingly.

As observed from the vibrational eigenmode at 1324 cm^{-1}, the mode is related to vibration of the amino and nitro groups. In the Figure, one of the molecules (i.e.; the inversion image) is not displayed in the unit cell, for the purpose of clarity. At higher frequencies, we observe the splitting of the degenerate mode ca. 2100 cm^{-1} to 2099 cm^{-1} and 2101.5 cm^{-1}. This split is caused by the change in the inter-planar hydrogen bonds due to rotation of NH_2. The peak at 1310 cm^{-1} changes to two peaks at 1342 cm^{-1} and 1336 cm^{-1}. This is caused by the changes in intra-layer hydrogen bonding and inter-layer hydrogen bonding. Lower frequency modes can be influenced by changes in molecular orientation within the unit cell. More specifically, the vibrations related to changes in conformation of the aromatic ring, ring breathing and modes involving both

the ring and its substituents can be observed. We show the results of the region between 100 cm^{-1} and 700 cm^{-1} in Figure 6.3.

Simulated X-ray Diffraction Patterns

We have also calculated the associated X-ray diffraction patterns of the structure before and after the observed molecular rearrangement. Changes in the inter-planar spacing for the (002), (110) and (1-1-1) directions can be seen in Figure 6.4. The dramatic change in the structure and unit cell parameters is revealed through the discontinuity in 'd-' spacing, near the observed 'transformation' at 1.6 GPa.

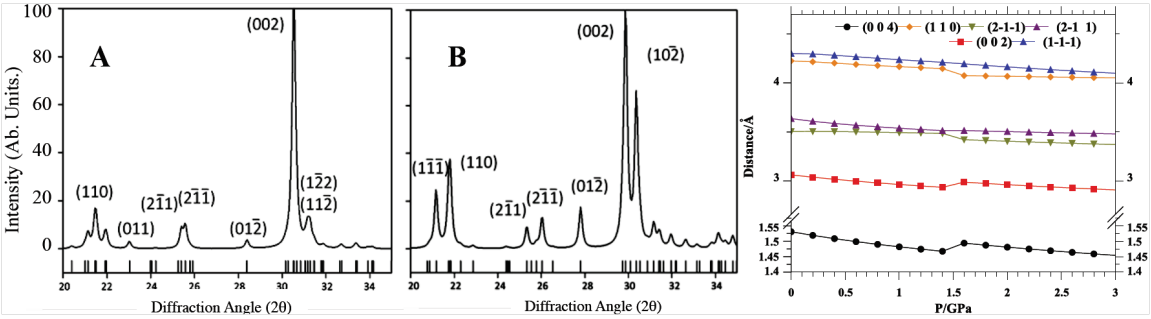

Figure 6.4 Changes in the XRD spectra. TATB molecule, at 1.5 GPa (A) and 1.55 GPa (B). Changes in d spacing for the selected planes (right). An abrupt change around 1.5 GPa can be clearly identified, for the spacing of the reported planes.

Analysis of H-Bonding Network

To understand the changes in the chemical environment of the system, we have embarked into the analysis of the conformations of the amino and nitro substituents, before and after the observed transition (Figure 6.5). From close inspection of the structure before and after the transition, we see that the oxygen atoms from the nitro groups, which were aligned in plane in the ambient pressure structure, have rotated out of plane to increase their interaction with molecules above and below the original plane.

In the ambient pressure structure, there were three hydrogen bonds per amino hydrogen. Two of them bonded within the same molecule, to adjacent nitrogen and oxygen atoms.

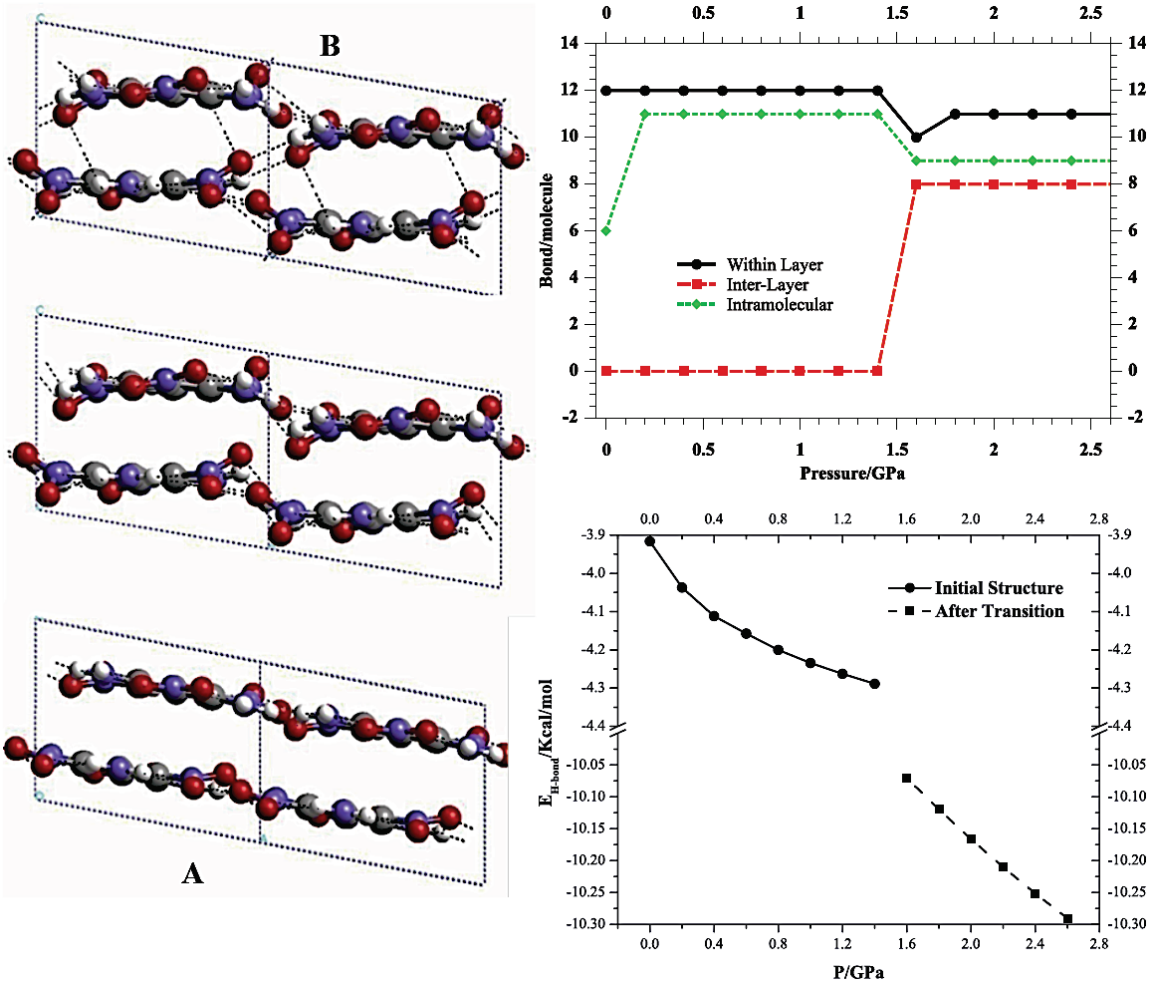

Figure 6.5. Structural rearrangements. TATB unit cell upon compression. View from the [010] plane of the TATB structure labeled "A", at 1.5 GPa (left). View at 1.55 GPa in the middle; and after the transition, at 1.625 GPa ("B"). Internal, and within layer hydrogen bonding is also rearranged (top, right). Total energy contribution from hydrogen bond energy at different applied pressures (right, bottom).

The other bond is formed with the neighboring molecule's nitro group oxygen. The longest hydrogen bond is 2.501 Angstroms. After the transition, adjacent molecules within the crystal field now allow for up to 4 hydrogen bonds per terminal hydrogen in

the amino group. The longest inter-layer hydrogen bond has a distance of 2.483 Angstrom. The amino group closer to the inversion center has interactions via two intra-molecular bonds and two intermolecular bonds; one of them is within the same layer and the other one with a neighboring layer. The total number of hydrogen bonds with neighboring layers along the 'C' axis changes from 0 to 8, after 1.6 GPa. All the amino group hydrogen's are bonded to at least another molecule.

Even though there are no restrictions throughout the calculations, the system keeps the symmetry of the initially minimized unit cell after the observed transition; that is, P-1. As expected from analyzing the changes in the hydrogen-bonding network, its stabilizing contribution to the total energy of the system increases from -4 kcal/mol to more than -9 kcal/mol.

Two State Model

To assess the thermal accessibility of the new state, we use a simple two state model by calculating the energetics of each and compare the kinetic energy required for the conformation "A", or flat dihedral angles, as compared to the 'bent' conformation, or conformation "B". The energy difference from one state to the other can be found from a calculation of the total energy of the structures at the DFT level with periodic boundary conditions. In this case we can obtain the energy difference from the structure under pressure; at volumes of 388.15 $Å^3$ from the pressure-loading run, and at 389.01 $Å^3$, from the pressure release run. The energy difference in this case is ca. 11.48 meV/atom, or $1.83x10^{-21}$ Joules. The probability of finding the system in state 'B' at 300 K can be estimated from the following equation.

$$P_{AB} = \frac{e^{\frac{-\Delta E_A}{k_B T}}}{e^{\frac{-\Delta E_A}{k_B T}} + e^{\frac{-\Delta E_B}{k_B T}}} \qquad (40)$$

The difference in energy would indicate a population of states close to 30%, of the available conformations, as estimated from the DFT calculations (Figure 6.6).

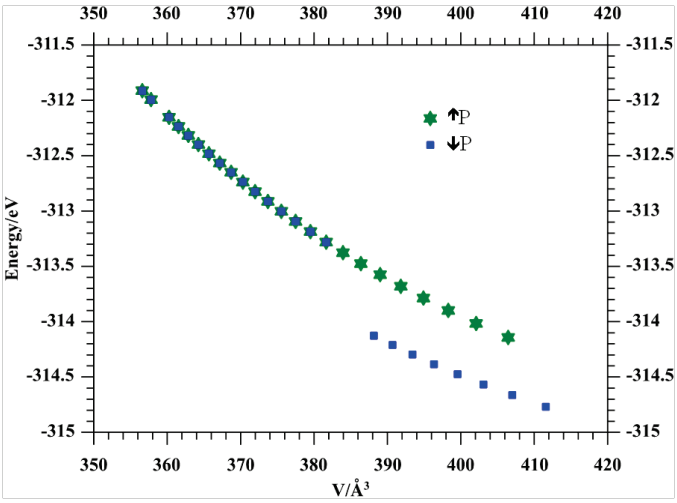

Figure 6.6 Total energy behavior. Calculated at the DFT/PBE level of theory. The energy difference observed from the initial compression run (green stars) and the structure after it recovers its volume upon pressure release (blue squares), can be attributed to the structural changes of the unit cell.

Potential Energy Surface

To further investigate the energy cost associated with the changes in conformation observed with the previous characterization methods, we performed electronic level calculations to study the potential energy surface of TATB molecule and TATB-dimer. Indications of possible local minima with bent dihedral angles within substitutional groups can be found from the potential energy surface (PES) of the single molecule. We

note that the potential barrier is not symmetric around 90°. The second barrier, with the nitro group lying flat, has a barrier of 4.12 Kcal/mol.

We also obtained the potential energy surface for a dimer, starting from the initial configuration; with all the nitro dihedral angles set at ca. 29°. We see a transition into a local configuration minimum, in which the system has one of the nitro dihedral angles rotated to -38° (Figure 6.7).

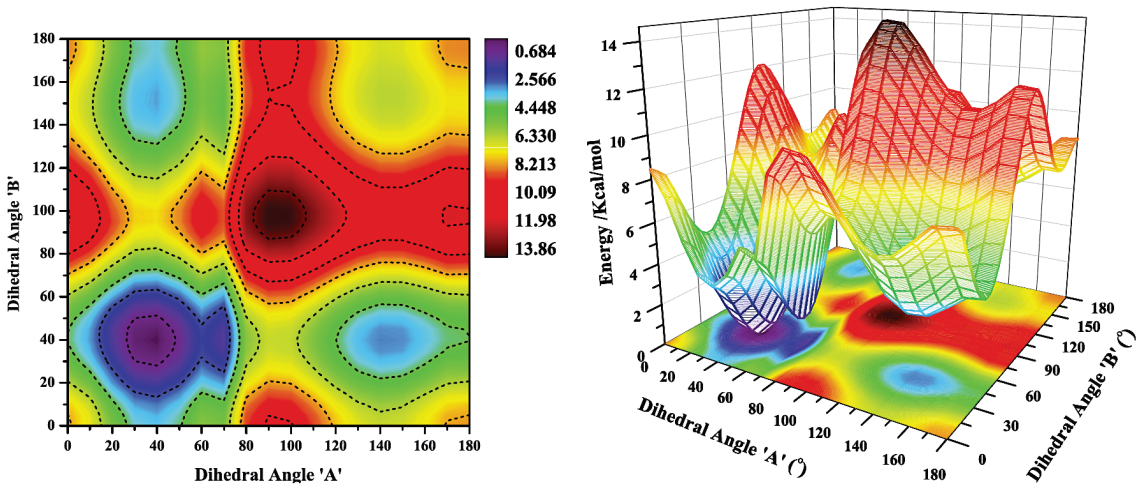

Figure 6.7 Potential energy surface of the TATB dimer. Calculations performed at the mp2/6-311++G level of the theory with an angle scan step of 5°. A local energy minima ca. 40° and 150° rotation can be located. The latter is located 3.32 Kcal/mol above the one at the intersection of 40°.

Effect of Pressure on Elastic Properties

To determine the anisotropic elastic response behavior of the system, we proceed to calculate the elastic stiffness coefficients as a function of increasing pressure. We see an abrupt change in the elastic coefficients of the TATB at around the same pressure (at ca. 1.5 GPa) as the molecular rearrangements occur (Figure 6.8). This is most notable in the stiffness constant C_{11}, and less pronounced for the C_{22} element. In the case of C_{11}, the

magnitude of increase is more than 50 GPa by virtue of increased hydrogen bonding interactions.

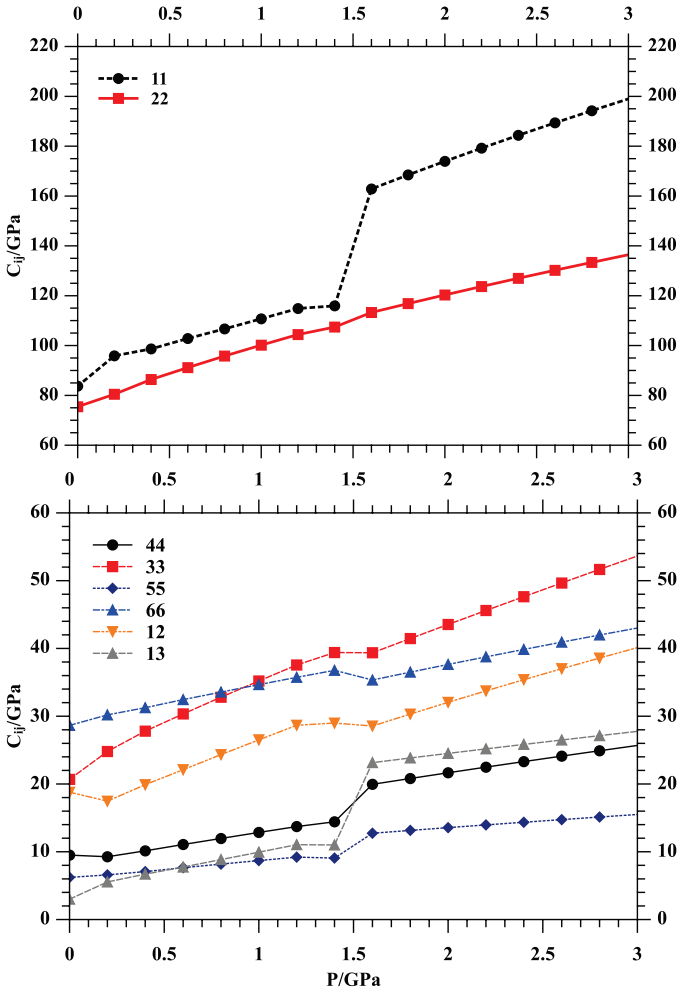

Figure 6.8 Variation of the anisotropic elastic stiffness tensor components. Different applied pressures.

Similar noticeable change behavior is also noted in off-diagonal elements of the stiffness tensor. This is the manifestation of the changes in hydrogen bonding network, hence a drastic increase in the stiffness of material in directions in accord with the new arrangement of the nitro and amine groups increasing the hydrogen bonding between

layers and adding strength to material. As expected by the changes in molecular structure, the coefficient that directly probes the stress-strain relation between the 'a' and 'c' axis, undergoes the largest percent in increase, as the C_{13} constant changes from less than 10 GPa to more than 20 GPa after the transition. This interaction is also reflected in the shear elastic constants, C_{44}, C_{55} and C_{66}.

We have found a peculiar behavior in the hydrogen bonding network and chemical environment of TATB, that manifest in the mechanical response of the crystal. To further understand this behavior, in what follows, a discussion to compare and contrast our results with other experimental findings is presented.

Changes in the vibrational spectra and periodic arrangement of the TATB system, has been the subject of numerous studies. For example, a gradual loss of transparency of TATB single crystals, and the presence of SFG behavior has been reported after thermal treatment up to 320°C. Interestingly enough there was also an indication of changes in the microstructure of thermally treated[390,416] TATB. A loss of the –NH stretching vibration with temperature and a peak increasing at 2320-2340 cm-1 were observed in earlier studies[423]. More recently, Holy[424] has studied the effect of compression in the low frequency Raman spectra of TATB pellets up to 180 MPa and noticed an increase in the hydrogen bonding strength of the material. Assuming a D3h point group symmetry, Deopura and Gupta rationalized the splitting of the degenerate νNO_2 observed in its neutron diffraction studies[425] as caused by a lowering of the point group symmetry due to the crystal environment. Later, Towns assigned the modes[426] as νNH_2 while comparing the electron withdrawing and electron releasing properties of related

compounds. Although the assignment from experimental data can be complicated by the presence of mixed modes and intermodal coupling[427], we can compare each normal mode to reported data. At 0 GPa, the calculated frequency of 1308.9 cm^{-1} compares to the previously reported values of 1229 cm^{-1}, obtained by neutron diffraction; 1221 cm^{-1} from FTIR, and at 1219 cm^{-1} from Raman scattering[428] experiments.

Recent work in the far infrared region at different applied pressures pointed out a strong coupling of the NO_2 NH_2 modes with pressure[388]. An irreversible transition was revealed after release to ambient pressure[418], as seen from the line at 290 cm^{-1}, assigned as a ring twist mode. The observed changes were rationalized as mixing and shifting of modes that translated with modes of lower pressures.

In our simulated spectra, this vibration shows a shift to lower frequencies, after the system is subjected to a pressure of ca. 1.5GPa. Upon release of the applied pressure, there is a noticeable change in both the intensity and the maximum positions of the simulated spectra. This can be noted in the increase in the maxima near 380 cm^{-1}, which involve the oscillation of the NH_2, NO_2 and aromatic ring atoms. This represents a change in the molecular orientation of the system, as observed from this low frequency region.

In relation to diffraction studies, Ollinger and Cady observed the reduction in the number of diffraction peaks at high pressures[429], while the group of Dattelbaum[157] has studied the hydrostatic equation of state for TATB up to 13GPa. They observe some reflections that could not be correctly assigned through the whole pressure range and attribute this to the anisotropy of the crystal, and its preferred orientation within the cell

chamber. Besides the general agreement found at low pressures (below 2GPa) with other studies, they have found a 'cusp' in their P-V curve. Based on previous experimental results on TNT and graphite they postulate a possible phase transition ca. 8 GPa, caused by a dimerization of the TATB molecule. Although we find no dimerization, results from our simulated data, show that most noticeable changes occur in the region close to the (0 0 2) plane. The inter-planar spacing, as obtained from Bragg's equation, shows a reduction in the distance of adjacent planes, after the transition is observed. Close scrutiny of the chemical and structural environment is then conducted.

In relation to the molecular structure of TATB, we note that its nitro groups show a libration angle of ca. 12° that can be deduced from the Debye Weller factors of the reported diffraction pattern[154]. Based on high-level *ab initio* and density functional theory method calculations, its molecular structure has been conjectured to be not co-planar[430,431] to the central ring. Freed, Gee and Manaa[341] had found previously a rotation barrier of 5.6 kcal/mol. Additionally, other studies have argued for the ease of libration up to 30° in favor of hydrogen bonding interactions[389]

We study both the single molecule TATB and its dimer, and found a value of 7.6 kcal/mol for a calculation at the HF/6-311++G//MP2/6-311++G level without any symmetry constrains. We note that the optimized isolated molecule structure has the nitro groups not planar with respect to the aromatic ring, but at a small rotation angle of ca. 15°. For the dimer system, we have found a local minimum that is located with the nitro group rotated to more than 30°. The structure of the dimer in this configuration is similar to the one found for the crystal after rearrangement whilst at high pressure. The

energy barrier to reach the new plateau as measured from our calculations is ca. 6.73 Kcal/mol, and 3.64 Kcal/mol, comparable to the internal rotation barriers of other resonance-assisted hydrogen bonded molecular crystals[432]. This is, there is a stabilization effect, caused by the crystal field, observed from the adiabatic angle rotation. The importance of hydrogen bonding in the series of amino-trinitrobenzene family of series has been acknowledged before[404]. Ledoux hypothesized the absence of inversion symmetry due to a rotation of the TATB molecule around its aromatic center[108]. Furthermore, the presence of sheet-sheet interactions and the breaking of an inversion centered caused by this interactions and defects has been conjectured previously[414]. Our model findings support the hypothesis of a structural re-arrangement induced by pressure that involves not a crystalline symmetry change, but changes in the hydrogen-bonding network of the 2D layers to a 3D structure. We can envision systems with the overall center of symmetry lost in regions interfacing planar and bent molecules, caused by local effects. This could explained how compressed samples with increased SHG signature have been reported[433], with no apparent change in chemical makeup, stoichiometry, and crystal symmetry of the used samples. The observed reordering will have a direct effect in the thermodynamic responses; as we have observed, there is a drastic change in the form of strain-stress relations, or elastic stiffness constants. The effect of the increased stiffness in the velocity of propagation of a compression wave may be better understood as changes in the sound velocity through the bulk system, as we will show next.

The importance of anisotropic properties and elastic coefficients for molecular crystals has been highlighted before[23,148,177,406,434]. Approximations for understanding the

elastic behavior of polycrystalline materials can be done through the use of the Voigt-Reus-Hill relationships[435]. The values of the system before and after the transition can be considered to be the upper and lower limits of the elastic behavior of a polycrystalline system[389]. Here, the subscript V, R, and VRH are used to discern amongst the last names of the authors developing the polycrystalline elasticity approximation.

Table 6.1 Voigt-Reuss-Hill averages. Values in GPa (Voigt, Hill) and GPa^{-1} (Reuss). Here "Δ" represents the difference in percent of before and after values.

	Before	After	Δ/%
K_V	42.99	54.17	26.00
μ_V	25.43	35.70	40.42
Ev	63.72	87.82	37.83
K_V	0.0323	0.0294	-8.78
μ_V	0.1545	0.1164	-24.64
E_V	0.0551	0.0421	-23.61
K_{VRH}	36.99	44.06	19.14
μ_{VRH}	15.95	22.15	38.86
E_{VRH}	40.94	55.79	36.29

The Voigt-Reuss Hill average shows an increase in the observed stiffness of the materials, particularly in the shear constants (Table 6.1) As observed from the difference in the barrier depth of the single molecule TATB obtained from the DREX6 force field and the *ab initio* single molecule and dimer studies, the transition in the real material could be expected to be at a different pressure. As opposed to the behavior of other energetic materials and molecular crystals, in which crystalline phase transitions and mechanical instabilities with increased pressure arises, changes in structure through molecular rearrangement of TATB can help explain the observed experimental behavior

and physical properties. Experimentally, one can further try to characterize the elastic response of the system, or more specifically the C_{11} constant to understand the effect of structural changes, preferably at pressure ranges under, 5GPa, in shock or impact loading experiments.

The molecular and hydrogen bonding rearrangement as induced by pressure for the insensitive energetic material TATB is reported. Systematic study through *ab initio* methods indicates the presence of local minima found for the dimer at this high-pressure configuration. Amongst the different thermodynamic, mechanical and chemical characterization required in understanding a material's response to external stimuli, elastic theory can be used as an important tool in understanding the response to mechanical impact. We have shown that in the static and long wave range limit, the second derivative of the system's energy with respect to position can itself be used as guidance to understand the thermodynamic changes that a known insensitive system (TATB) can have; more significantly, when other energy response functions (heat capacity, etc.) do not seem to have any type of transition. This type of elasticity driven study can further be pursued for other system, e.g.; NM, Fox-7, PETN, HMX, and other molecular crystals, in order to gain insight of the relevance of intra- and intermolecular interactions. The changes in bonding and structure, which should manifest additionally as changes in the observed elastic properties, could indicate the necessary chemical characteristics of other possible insensitive energetic materials.

It has been suggested that grain size more than void concentration can have an effect on the detonation pressure of some energetic materials[436]. We will now pursue

understanding in the role of deformation mechanisms in the initiation of the energetic materials.

CHAPTER VII

EFFECTS OF DEFECTS/GRAIN BOUNDARIES

Description

It has already been shown that defects have an effect on the sensitivity to impact of the energetic materials. We want to explore the effect of crystal defects on the anisotropic mechanical response of the energetic materials under both hydrostatic and axial compression, and with the application of shock. It has been suggested that grain size and orientation more than void concentration can have an effect on the detonation pressure of some energetic materials[436,437]. Compression of Energetic materials (EM) with a polymeric binder facilitates casting and machining. This is usually done with a small weight percent of binder included in the formulation. For example, compsition LX-16 has 96%w PETN and the rest as polymer binder. Heterogeneities in the microstructure of polymer bonded explosives raise difficulties in understanding trends like sensitivity and mechanical properties, as compared to the homogeneous material. Unlike other systems, e.g.; metals, the effect of plasticity in detonation properties of energetic materials remains a nascent topic.

Processing parameters can have an effect in the sensitivity of the energetic materials. Crystals purified with different solvents, e.g.; cyclohexanone or acetone, will produce different number of cavities and voids[438], and become sources of dislocations. Changing from cyclohexanol/ethanol to g-butyrolactone/water change the crystallization morphology of RDX from small crystallites to dendrimers[439]. The effect of the void and

vacancy concentration has been suggested to have an effect in the sensitivity of systems like RDX and HMX[440]. Crystallization conditions will also have an effect on the specific morphology of the grown crystal habit[441]. Understanding the thermodynamic and elastic effects in sensitivity can help tailor some of the applications of EM's to civilian realms[442], and also reduce associated hazard of transporting and handling of the materials. The prepared crystals are usually compressed to achieve high density either with other type of energetic materials, or with a plastic binder. Detonation pressure for a given system will depend[443] on the density of the material; therefore, compression to achieve high density in this binder-energetic material matrix is performed. Since there is a small weight percent of plastic binder, stresses localization caused by the close contact of different crystal faces can be expected, specially under conditions of high stress rate (as in direct impacts) or supersonic shock strains

By means of molecular dynamics simulations, we show the results of the studies on a commonly used secondary explosive; PETN, which has an anisotropic response to shock detonation. The goal is to understand the role of deformation mechanisms in the initiation of the energetic materials.

The slip plane has been suggested as the (110) plane, with possible Burgers vectors in <111>[444], other studies suggest the formation of a slip system in [110](001)[4]. By means of layer projection, we have created large super cells (up to 868 molecules) of the latter, and studied by means of molecular mechanics and molecular dynamics simulations. Creation of the [110]- and [001]- layers with 3-D periodic boundary condition was performed initially on the single crystal system. This layers were then

expanded to a matching length of ca. 35 A per side. Stacking along the z-axis of the [001] was used for alignment. This created the first set of bi-crystals for simulation. After the results of molecular dynamics simulations were obtained, a larger grain system was set up. In this case the z-direction was doubled in size, with the intention of reducing the finite size effects of the stacking fault in the grain system. The crystal packing of PETN facilitates identification of a discrete number of layers on each side of the grain system.

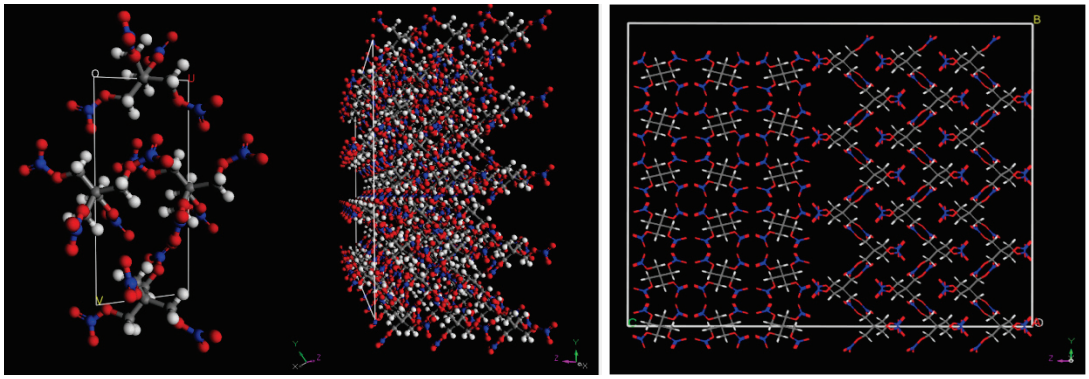

Figure 7.1 Construction of the system under study. [110] plane (left) and [001] layer of PETN. Right: [110][001] Grain boundary system of PETN.

Molecular Dynamic Simulations

In order to assess the quality of the force fields, molecular dynamics simulations have been performed in a large (4x4x6) super cell of PETN. The initial applied temperature (50K) was ramped in increments of 50K up to a value of 550K. Averages were obtained for the last 40 ps from the 60 ps run. Equilibrium volumes at 300K (621 $Å^3$) are comparable to the experimental reported values[164].

From these runs initial structures of obtained for the succeeding molecular dynamics simulations to obtain the relaxed system's energies, at 50, 250 and 300K. The initial 50K

temperature is employed in order increase the temperature gradually of the system to the target value of 300K. There is already a change in the density of the material when prepared along one phase, as compared to the denser packing found in the [110] direction. There is a stacking fault caused by the atom mismatch in the inter-planar spacing of the [110] direction as compared to the [100] direction.

The surface energy is calculated using the following formula:

$$\Delta E = E_1 - nE_0 \qquad (41)$$

Here E_1 indicates the grain system energy, E_o the minimum energy per face (Eo/2) and n is the number of molecules in the system.

From molecular mechanics calculations, which were iterated up to 2000 steps, with a convergence on the energy of 10^{-3} Kcal/mol and a convergence on the forces of 0.5 Kcal/mol/Å., we are able to obtain the energetic of the formation of the system. The first set of results can be observed in the following Figure 7.2.

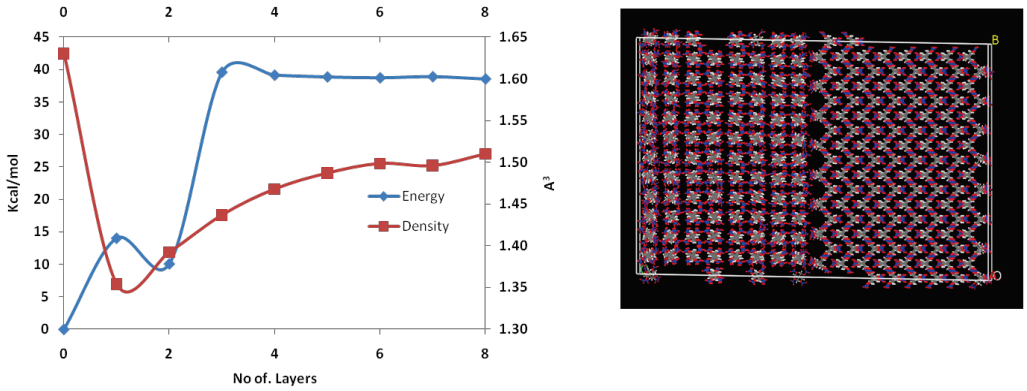

Figure 7.2 Change in energy and density. Effect of number of layers, left. 8 layers system observed from the [001] direction, right.

Molecular Dynamics Simulations show also a positive energy of formation for the interface. In here, we have been able to construct a thicker bi-crystal. We can see a change in the energy profile close to 9. Closer inspection of the structures shows a change in the crystal orientation, caused by the plane mismatch. We see also a reduction in the total energy with respect of temperature.

At the interface, there seems to be a larger number density of nitro groups expanding from the [110] crystal, this could explain the increased reactivity observed for compressions along this direction. Formation of the grain system shows an initial change in the density of material, although the density increases to with the number of layers, it is not expected to reach the value of the defect free system.

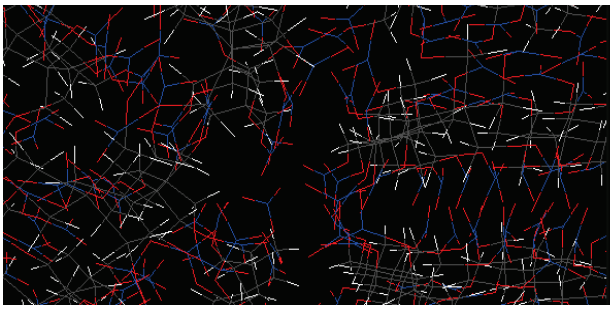

Figure 7.3 Interface of the grain boundary. The [001] direction (left) and the [110] plane(right) shown. Snapshot from the MD simulation at 250K. Oxygen atoms represented in red, nitrogen in blue and carbon as gray (hydrogen is white).

After the initial observation of the effect of crystal orientation and sensitivity found in PETN by Dick[4], a model of steric hindrance was put forward. In this model, it is assumed that sensitivity will be related to the number of intermolecular close contacts that can be found when straining along a particular direction. Based on surface etchings, Sherwood[444] has reported a Burgers vector as b<1,-1,1> and a length of 1.48 nm. Their

study has concluded that for the suggested slip system, steric hindrance would be limited to half as the one observed in our studied system; Although both in the early reports by Dick and Sherwood, acknowledge is made to the high number of intermolecular contacts is made in the (110)(001) grain system, no further discussion is presented. Our simulations indicate that possible smaller Burgers vector can be realized for this type of grain.

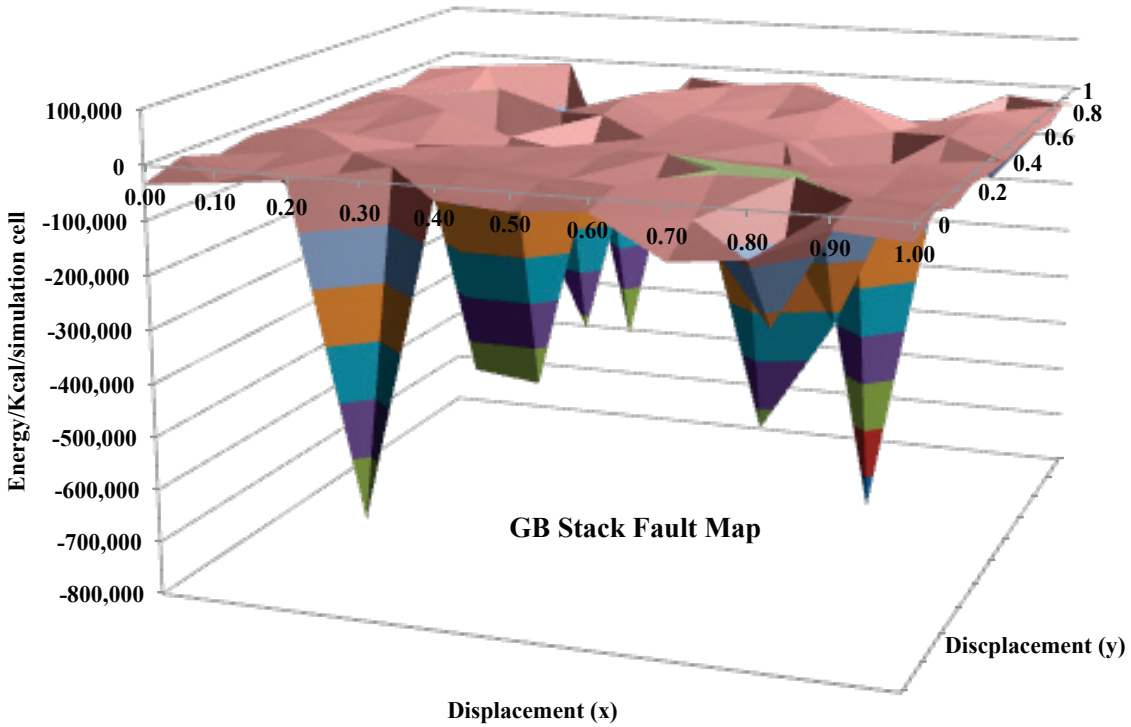

Figure 7.4 Stack fault map.

Further studies on the equilibrium and dynamic gamma surface or interface, can hint to more stable conformations, and be used as basis for shock experiments.

As our exploration through increasing time and lenghtscales bring us the use of larger systems and elevated temperatrues and pressures. The effect of temperature and

energies was related to different reaction rates. We will now focus on one example in wich a particular reaction pathway can be resolved, in specific thermodynamic conditions. This for the case of the system nitroethane.

CHAPTER VIII

IDENTIFICATION OF REACTION PATHWAYS

Initiation Chemistry

The specific properties of high performance and sensitivity have to be considered for stable energetic materials. Higher risk efforts are underway to explore the possibility of meta-stable energetic materials. There has been extensive research to measure the kinetics and elucidate the mechanism of their decomposition for a long time. The study of thermal decomposition mechanism is essential to engineering design and fundamental to the design and optimization of materials. The kinetics of thermal decomposition is expected to illustrate the mechanisms of initiation and stability. In this section, we will focus on the decomposition pathways in gas-phase and investigate their thermodynamic properties in condense phase, from molecular dynamics simulations within a 'first principles' methodology.

C–NO_2 bond rupture is often suggested as an initial step in the thermal decomposition of nitro compounds, because the attachment of nitro groups is relatively weak[356,409]. The C–N bond dissociates without an apparent transition state structure, and affords two radicals. The calculated reaction enthalpy for gas-phase nitroethane to form radicals is 56.1 kcal/mol at the B3LYP/6-31+G(d) level. To better understand the C–NO_2 bond rupture, a detailed reaction profile was calculated as a function of C–NO_2 bond length.

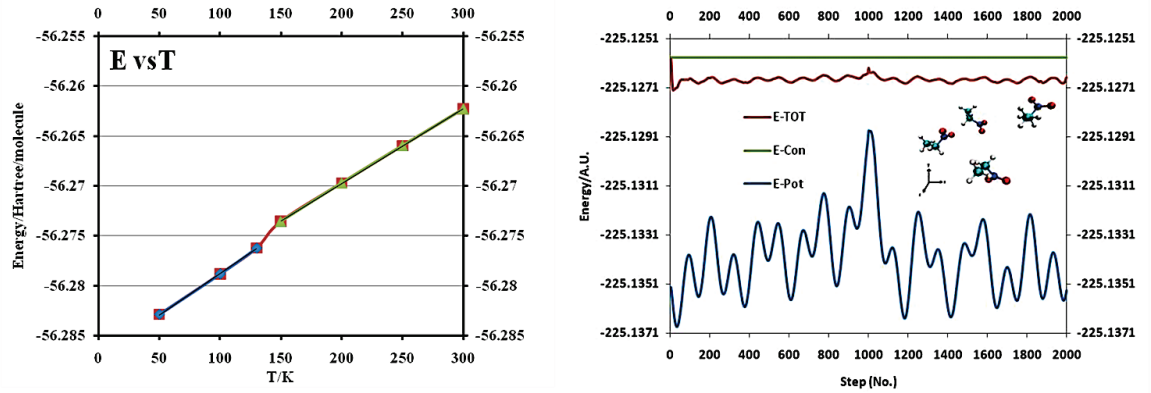

Figure 8.1 Internal energy of NE as a function of temperature. Phase change found (left); Instantaneous values for the components of energy for 2000 steps of MD simulation of Nitroethane.

Ab Initio Molecular Dynamics

The converged (10^{-7} atomic units (au)) wavefunctions from the initial position were used as initial guess for the first Car-Parinello molecular dynamics run. Since the initial gradients can be very large, an initial kinetic energy of 50K was used. Atoms were allowed to move, and then the kinetic energy was slowly removed. From this "annealing" procedure an equilibrium configuration of the electron density and ionic positions was obtained. The electronic density for each atom was used for the Parinello-Rahman microcanonical ensemble simulations that followed the damping run. As seen from Chapter III, these materials hava a large band gap, which allows for small coupling between the electronic and vibrational degrees of freedom in the simulations.

An initial equilibration run of 2000 steps, with a step size of 4 au (1 au= 0.024188843 femtoseconds). Then a longer run of 2000 steps, with velocity scaling of 200 K was realized, All at 50K and doubled initial temperature. We see from the instantaneous values (Figure) that the system is closer to its equilibrium configuration.

The conserved energy (E-con) is in fact stable ca. -225.1261 Hartree. From these simulations we can extract the average value of the electronic (fictitious) kinetic energy, and use as input for constant temperature simulations, with Nose thermostats for the ions and the electrons. This simulation can further be used to obtain equilibrium values and averages at higher temperatures. An upper limit of 300K is proposed, with increments of 50K and averages of 80000 steps.

Results

After the equilibrium volumes were found, a larger Nitroethane cell was constructed, with an approximate density of that of the liquid (1g/cm^3). Here again the challenge was first to obtain an appropriate wavefunction to be used in calculations at higher temperatures. The obtained wavefunction was used as input to perform car-parinello molecular dynamics at constant volume and energy. This procedure applied to explore determining any or which chemical reactions occurring at a given elevated temperature.

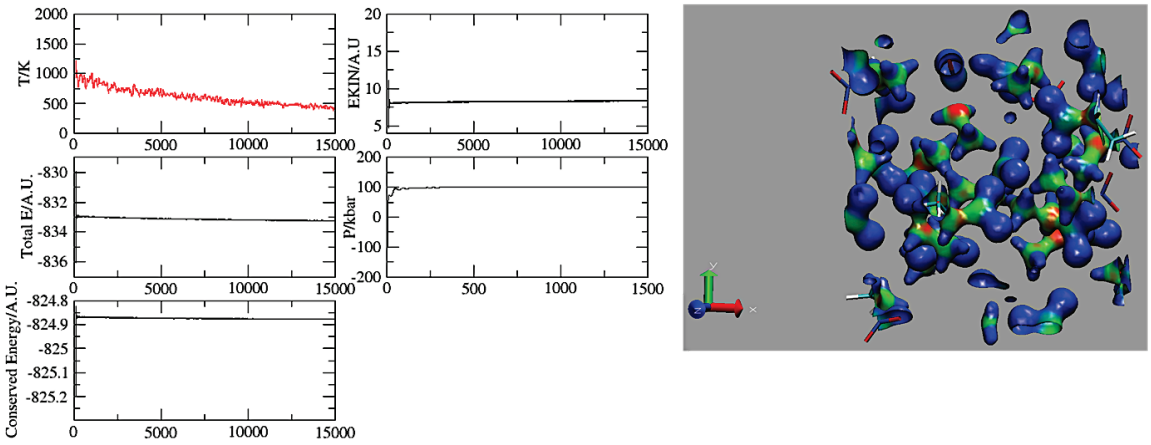

Figure 8.2 Running average of the larger 15 molecule system. NVE Simulation results (left). Electrostatic potential mapped into the molecular charge density isosurface (0.16 Hartree).

From the different snapshots taken at this initial step, we see even at the lower temperature of 1000 K, that the initial bond to break is the NO_2-ethylene bond. Mulliken population analysis shows a large positive charge on nitrogen (0.65) and a large negative charge on the nearest carbon, -0.67. The Mayer bond order for this atom is less than one (0.68), indicating a looser interaction as in a regular sp^3 bond.

At the detonation transition, the temperature of NM has been estimated[445] as 2500K Temperatures in excess of 10^4 K have been found[446] in compressed air inside detonating PETN. In a recent study, Mathews et al[447] analyzed the optimized bond lengths and structures of amino substituted nitroethanes, their equilibrium bond distances were never in excess of 1.7 Å. Kwok have suggested a very fast transfer from an exited NO2 to the C-N bond as this was suggested as the primary mechanism as studied from Raman spectra[448]. Our results indeed find that even in the initial phases of equilibration, NO_2 bond scission occurs for temperatures of 2000K.

CHAPTER IX

ELASTIC PROPERTIES AT ELEVATED TEMPERATURES AND PRESSURES

Introduction

Molecular dynamics methods have been proven appropriate to describe the mechanical properties of metals, ceramics and some organic systems[253]. More recently, some attempts have been made to obtain the elastic properties of molecular crystals[449] under the isothermal isobaric (NPT) ensemble[450]. In particular for the energetic material (EM); 1,3,5-triamino-2,4,6-trinitrobenzene (TATB), understating the mechanical properties at elevated temperatures and pressure, is important since subtle differences can have implications in the stability and properties of this insensitive[339,387] EM as subjected to external stimuli, such as heat or compression[341,403,415,431,451]. Therefore, related molecular and atomistic level information and its behavior as compared to other type[284] of EM could hint to the unusual insensitivity[407,408] of this material. As opposed to the limit of 0K, elastic properties of a material at ambient conditions do have contributions from kinetic energy and stress fluctuations in the system.

For a solid, stress and strain (σ,ϵ) can be related to each other by Hooke's law;

$$\sigma_{ij} = C_{ijkl}\varepsilon_{kl} + C_{ijklmn}\varepsilon_{kl}\varepsilon_{mn} + C_{ijklmnpq}\varepsilon_{kl}\varepsilon_{mn}\varepsilon_{pq} + \ldots \qquad (42)$$

The fourth order rank tensor C_{ijkl} is commonly known as the elastic constant tensor, and its elements comprise the second order elastic constants. Under finite strain theory, this proportionality constant can describe the mechanical behavior of solids. Different

approaches to obtain this elastic behavior vary from empirical force models[452], the second derivative method[453], temperature and stress control molecular dynamics methods[454] fluctuation formulas [294,455] at thermodynamic equilibrium state and engineering[243,251] and finite deformation or stress application methods[283,456,457]. The second order elastic constants are found to vary considerably under finite strain conditions. These nonlinear effects can be accounted for by the higher order terms to above equation, namely introducing higher order elastic constants. For instance, we find that the second order compliance tensor is defined as:

$$S_{ijkl} = \frac{V_o}{k_b T}\left(< \varepsilon_{ij}\varepsilon_{kl} > - < \varepsilon_{ij} >< \varepsilon_{kl} > \right) \tag{43}$$

While the third order elastic compliance tensor is defined as

$$S_{ijklmn} = \frac{V_o}{k_b T}\delta\left(\varepsilon_{ij}\varepsilon_{kl}\varepsilon_{mn}\right) \tag{44}$$

The compliance tensor is related to the second and third order stiffness coefficients by;

$$C_{ijkl} = S_{ijkl}^{-1} \tag{45}$$

We have defined here the strain tensor as previously;

$$\varepsilon = \frac{1}{2}(h_0^{'-1} G h_0^{-1} - I) \tag{17}$$

And the crystalline system is defined by the set of h vectors ordered as;

$$h = \begin{pmatrix} a_x & 0 & 0 \\ a_y & b_y & 0 \\ a_z & b_z & c_z \end{pmatrix} \tag{46}$$

The matrix 'G' is defined as; $G = h^{'}h$. The second order isentropic elastic coefficients are thus defined as:

$$V_0 C^s_{ijkl} = -\frac{V_0^2}{k_B T}\left(<\sigma_{ij}\sigma_{kl}> - <\sigma_{ij}><\sigma_{kl}>\right) + 2Nk_B T\left(\delta_{ik}\delta_{jl} + \delta_{il}\delta_{jk}\right) + \chi_{ijkl} \quad (47)$$

The term that depends on the potential energy is called the 'Born" term. It is defined as;

$$\chi_{ijkl} = \frac{\partial^2 E}{\partial\varepsilon_{ij}\partial\varepsilon_{kl}} \quad (48)$$

For metallic systems, it is known that the stress (σ_{mn}) fluctuations are at least an order of magnitude smaller than the Born Term. The behavior is unknown for softer molecular crystals, like EM's. The third order fluctuation formulas are defined as;

$$C^s_{ijklmn} = \frac{V_0}{k_B T}\left[\delta\left(\tau_{ijkl}\sigma_{mn}\right) + \delta\left(\tau_{klmn}\sigma_{ij}\right) + \delta\left(\tau_{ijmn}\sigma_{kl}\right)\right] - \left(\frac{V_0}{k_B T}\right)^2 \delta\left(\sigma_{ij}\sigma_{kl}\sigma_{mn}\right) + \frac{V_0}{k_B T^2}\left(\frac{\partial T}{\partial\varepsilon_{mn}}\right)\delta\left(\sigma_{ij}\sigma_{kl}\right) - \frac{3Nk_B T}{V_0} D_{ijklmn} + \frac{\zeta_{ijklmn}}{V_0} \quad (49)$$

Here, τ is second derivative of the Hamiltonian with respect to strain 'ε', 'ζ' is the third derivative of potential energy with respect to 'ε' and D_{ijklmn} is a 6th rank tensor product of δ_{ij};

$$D_{ijklmn} = \delta_{im}\delta_{\ln}\delta_{jk} + \delta_{im}\delta_{kn}\delta_{jl} + \delta_{in}\delta_{km}\delta_{jl} + \delta_{in}\delta_{lm}\delta_{jk} + \delta_{ik}\delta_{lm}\delta_{jn} + \delta_{ik}\delta_{\ln}\delta_{jm} + \delta_{il}\delta_{km}\delta_{jn} + \delta_{il}\delta_{kn}\delta_{jm} \quad (50)$$

We have performed molecular dynamics simulations with the Dreiding exp-6 form force field[117]. A time step of 1fs is used. For the equilibration part of the dynamic run, both kinetic energy scaling through ionic velocities and Hoover thermostat was used. The

evaluation of total energy averages was obtained from for at least 200 ps. after these stabilization runs, which were typically found in the range of 400 ps. From here, average values of lattice vectors were obtained to construct or reference h_0 matrix.

The equilibrated lattice parameters can be thus used in constant volume microcanonical or canonical ensemble; to obtain the average energies and stresses at each applied strain state. This results in either the isentropic or isothermal elastic constants. We show here the results at low temperature for the system TATB. We have used the method of QEq for charge equilibration, with the use of the exponential-6 form of the Dreiding forcefield, with the use of Cerius2 or Forcite module of Materials Studio, from Accelrys Software, Inc[458].[248]

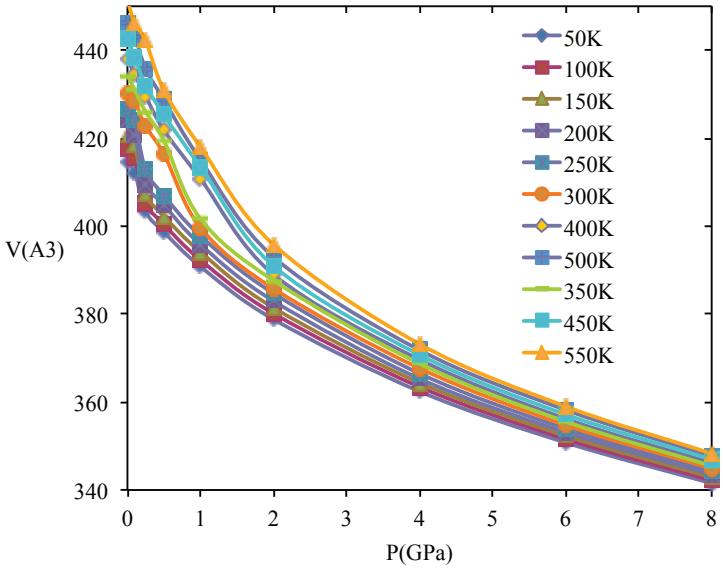

Figure 9.1 TATB isotherms.

Results

Equilibrium lattice parameters are obtained from isothermal isobaric ensemble averages. The obtained isotherms can be found in Figure 9.1.

For the case of TATB, a larger aromatic system, which is stable at ambient temperatures and pressures, we see that the choice of strain amplitude is more important in describing the system in the current thermodynamic state. On a system that fluctuates around an average value of temperature and pressure, we can expect visits to thermodynamic states that differ from the equilibrium thermodynamic state, when the strain amplitudes are large. As an example we take the case for the strain in the 'x' direction. We have plotted the results of the whole studied strain amplitude strain, the error bars represent one standard deviation from the total collected data points in the 200 ps evaluation run (Figure 9.2). Even though the single point energy calculations at strains amplitudes show an elastic behavior up to 10% tensile strain, this behavior is not observed when compressing the TATB crystal. We have thus restricted our calculations to strains in the elastic region.

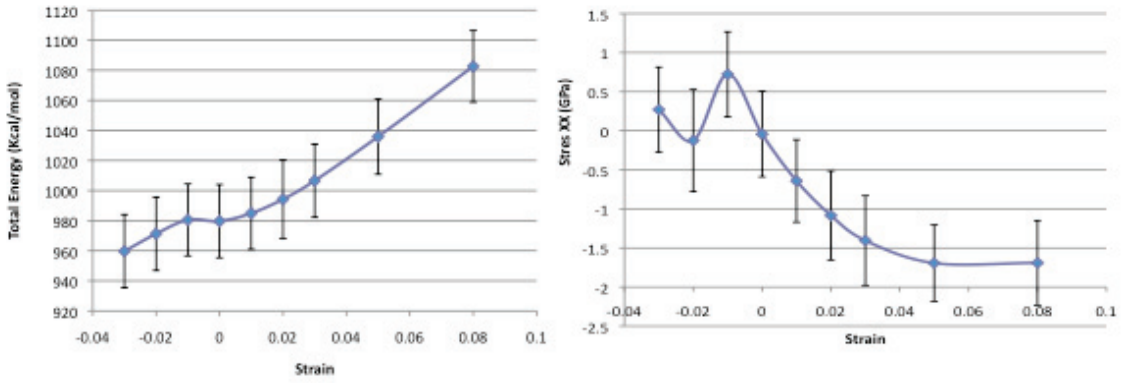

Figure 9.2 Strain in the 'x' direction. Strain values up to 8% tensile and 3% compressive. Error bars represent one standard deviation in the average error of the total run.

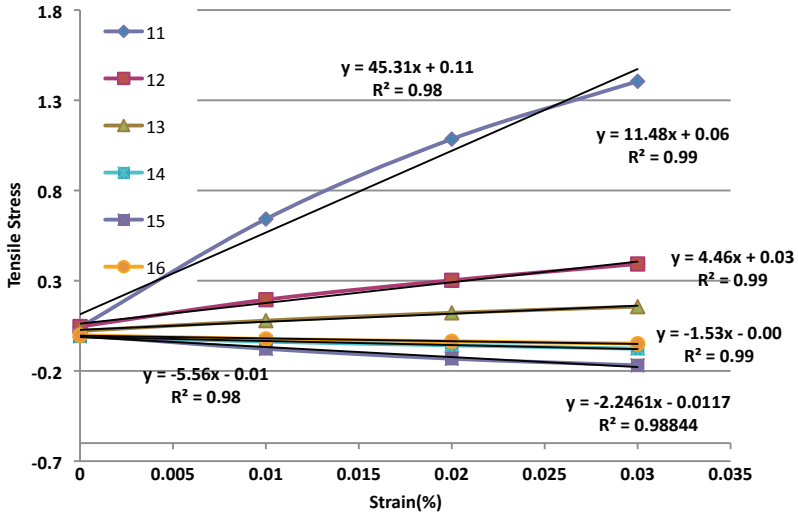

Figure 9.3 Stress/strain components. Strain in the x direction.

From Figure 9.3, we can see that the proper choosing of strain amplitude has an effect on the value of the calculated elastic constants. For a crystalline system, like TATB, we see the onset of non-elastic deformation at 5%. This indicates that there is strong contribution from higher order elastic terms, and therefore the use of an elastic constant of second order describing the linear relationship between stress and strain in this amplitudes, is no longer valid.

Table 9.1 Stress/strain and energy/strain results for C_{11}.

Strain Range:	0.5%	1%	2%
$C_{11}(E)$	70.33	48.54	68.74
$C_{11}(\sigma)$	70.125	37.41	60.211

We can see in table 9.1, that the range in which the stress follows a linear relationship with the applied strain is rather small. We see that te value of 0.5% gives

comparable values as obtained from stress/strain relationship as compared to strain/energy relationships. The use of stress or energy in this case gives a value within less than 1% of one another.

To assess the precision of our calculations, and based on two and four block averages over the evaluation period of 200ps, we have observed a variation in the standard deviation in Energy smaller than 400 cal/mol and 0.0064GPa in total pressure. We then proceed to obtain strains with a change from the equilibrium parameters at least twice the magnitude of this standard deviation.

Table 9.2 Second order elastic tensor for TATB, 300K.

70.33	19.83	8.16	-5.46	-7.80	-1.65
*	62.43	13.31	-17.76	-1.10	-3.36
*	*	19.67	-0.55	-0.19	2.69
*	*	*	7.74	2.06	-2.59
*	*	*	*	4.85	-6.53
*	*	*	*	*	22.57

This ensures that higher order contributions are kept to a minimum. We can observe the complete elastic tensor for TATB in Table 9.2 above. For most strains a value of 0.5% or 1% maximum was used. Linear stress/strain relationships are used for each of the stress components on a given applied strain. For the strain d1, we will have 6 different stress /strain relationships, from the 6 independent stress tensor components. This also gives the advantage of obtaining independent values for the off-diagonal second order elastic stiffness components, which can be averaged to report a single value. Strain step size was kept as 0.05%.

Care was taken to use a strain range in which the energy difference between tensile and compressive strain energy was below 2Kcal/mol. In case of the diagonal elements of the elastic stiffness matrix, values smaller than the precision of the calculation were discarded. The most common type of linear fit comprised of a 9 data step curve, with a maximum strain amplitude of 1%. Calculations at elevated temperatures, in 50K increments up to 500 or 550K can now proceed. In the same fashion, calculations of the elastic constants at elevated pressures are now feasible.

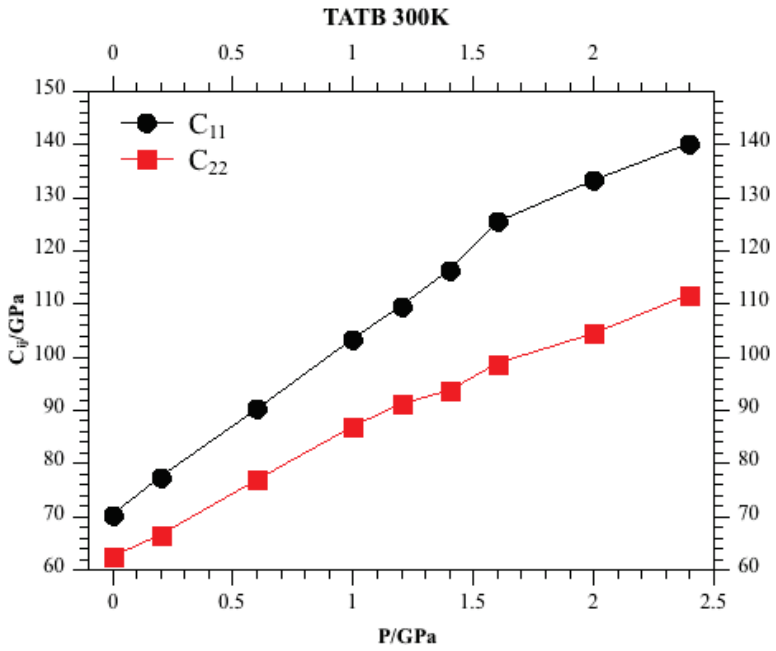

Figure 9.4 Second order elastic coefficients at elevated pressures. C_{11} and C_{22} shown.

The bulk modulus obtained from Voigt-Reuss-Hill Relationships is 26.11 GPa. In the cases of the shear strains, particularly the once with smaller value, like C_{25} and C_{43}, their value can be accounted for as zero. Due to the symmetry of the fourth rank tensor, Cij should equal Cji, here we are using the well known Voigt notation. Based on this

difference, we can observe a maximum value of 4.44 GPa in our calculation, for the case of C_{14} and C_{41}. This indicates the accuracy of the calculation.

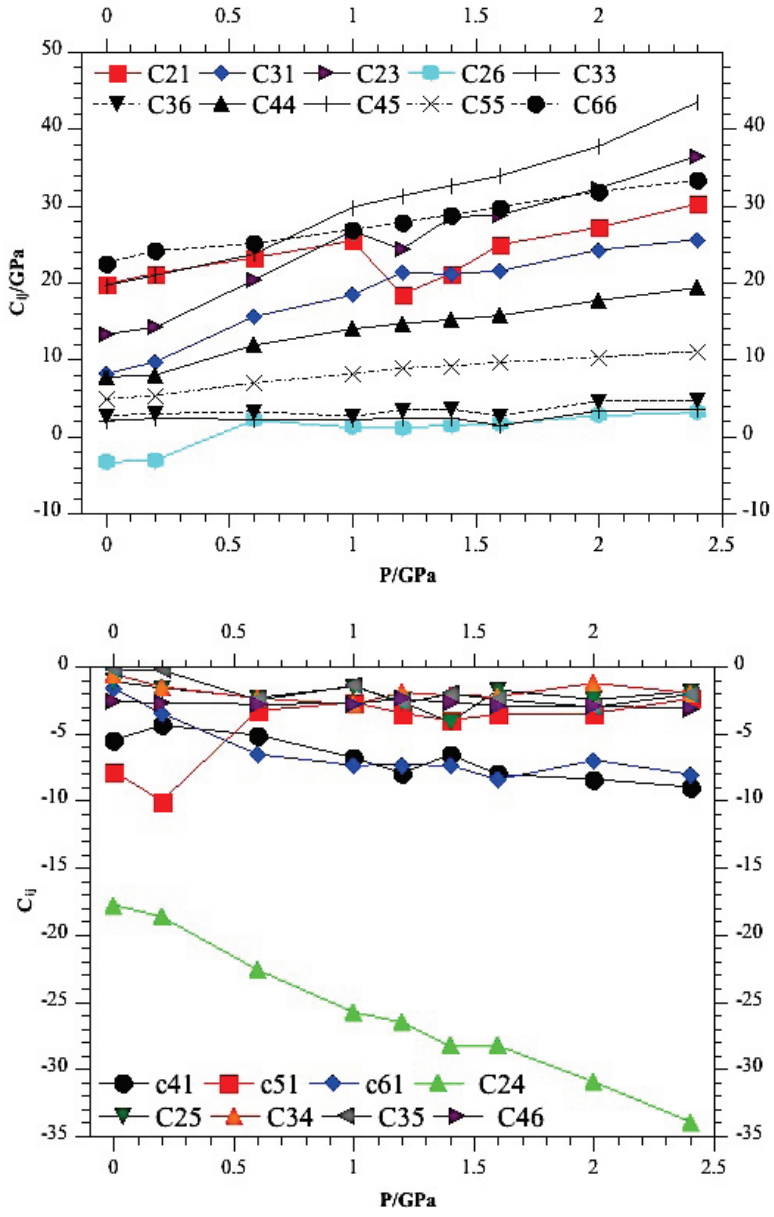

Figure 9.5 Individual second order elastic coefficients at elevated pressures.

From the value of the error value in stress for σ_{11}, we can se that the value of C_{11} can range from 74.66 GPa to 67.46 GPa. This gives a standard deviation for C_{11} of 5.1 GPa. We shall present now the results of the pressure variation of the elastic constants of TATB, with the consideration that the error at each given pressure value has to be determined (Figure 9.4, Figure 9.5).

At elevated pressures, account for the stress components of the reference system are obtained through the use of effective elastic coefficients:

$$B_{ijkl}^{T} = \frac{1}{2}(\tau_{il}\delta_{jk} + \tau_{jl}\delta_{ik} + \tau_{ik}\delta_{jl} + \tau_{jk}\delta_{il} - 2\tau_{ij}\delta_{kl}) + C_{ijkl} \quad (50)$$

The values obtained from the calculated B_{11} and B_{22} components can be observed in the following Figure 9.6.

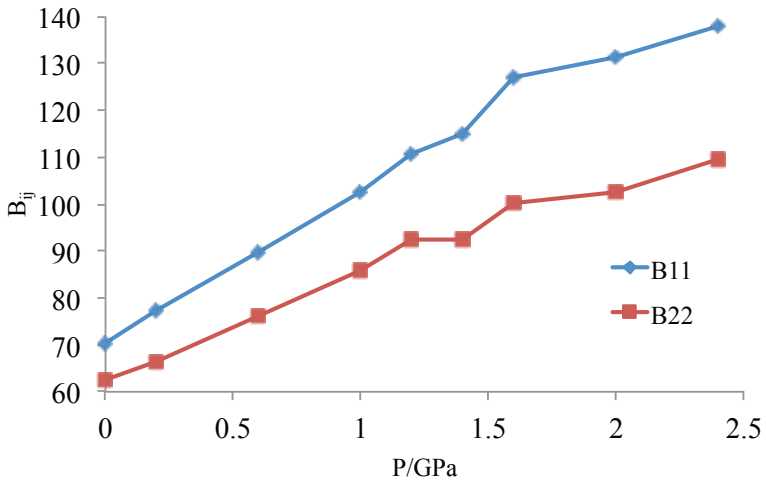

Figure 9.6 Effective elastic coefficients. B_{11} and B_{22} at different hydrostatic pressures.

The calculations from fluctuation formulas will require larger unit cells, as opposed to the 2x2x3 used here, and longer simulation runs. On a single unit cell, with 400ps, of equilibration and 2.5 ns of evaluation time, we calculate the born term, every 3 frames, recorded every 10 steps.

Table 9.3 Born term, 2.5 ns.

63.46174	14.33102	8.51812	-9.18417	-12.44448	-3.07727
14.33102	57.45807	11.55457	-20.76957	-4.87455	-1.19021
8.51812	11.55457	11.07151	0.06052	-0.05378	1.54034
-9.18417	-20.76957	0.06052	4.99442	-1.86259	-2.20373
-12.44448	-4.87455	-0.05378	-1.86259	-0.30678	-6.79433
-3.07727	-1.19021	1.54034	-2.20373	-6.79433	21.32726

As compared to the calculation run on 7 ns of evaluation time;

Table 9.4 Born term, 7 ns.

100.36758	47.12743	28.06895	-66.24329	-38.51751	11.90937
47.12743	58.29267	13.74542	-38.50781	-10.43822	-8.14332
28.06895	13.74542	18.13992	-21.89618	-11.09003	0.35722
-66.24329	-38.50781	-21.89618	70.84115	29.85327	2.29928
-38.51751	-10.43822	-11.09003	29.85327	18.67084	-1.42712
11.90937	-8.14332	0.35722	2.29928	-1.42712	5.26445

We have found that convergence of average energies and stresses is the main issue when calculating the elastic properties of these organic systems. As opposed to metals and others strongly bound systems, in this cases not even the Born term converges rapidly as seen from values obtained from average of two different time length (Table 9.3, Table 9.4).

CHAPTER X

CONCLUSIONS

Energetic Materials

Due to the chemical, mechanical and thermodynamic level information that provides, multiscale modeling methods, can then be applied to the understanding of other type of systems and give a clearer understanding of the molecular processes that undergo energetic materials, prior to initiation. Beyond a generalization from a particualar model, spectroscopic paramters or isolated information from gas phase molecular structures, we have found that specific thermodynamic information can be substracted from particular type of theoretical experiments. In our particular case, We have conducted first principles ground state studies, complemented by atomistic calculations at elevated temperatures and pressures, for energetic commonly used secondary EM's with varying sensitivities. Chemical information found from *ab intio* methods, and from compression at elevated temperatures show that external conditions relevant to impact and shock behavior can have different effects on the studied systems. These range from changes in local conformation, changes in the hydrogen-bonding network, and more drastically to a full crystallographic transition in which the symmetry of the system undergoes a transformation.

A common assumption found in literature is that both impact and shock sensitivities are referred to as the same type of behavior. Any change observed in the electrostatic potential/charge of the system at different compressed states shall be correlated to

specific thermodynamic states accessible from experimental techniques (flyer plate viz. hammer test. Information found from *ab intio* methods, and from compression at elevated temperatures indicates that impact and shock behavior for secondary energetic materials will have different manifestations. These reveal the anisotropic behavior of the studied systems. Departing from normal conditions, we observe that there is a discontinuity in the enthalpy pressure curves for NM, a system that is sensitive to shocks but insensitive to impact. A non-monotonic behavior is observed for the case of PETN. Although indications of sensitivity for the [100], [111] and [001] planes for NM have already been reported[159,381,382,384,385], our results give insight as to what is de mechanism for sensitivity for each crystallographic direction. As expected due to its low impact sensitivity, the NM system can undergo a monotonic change in enthalpy at low pressures/compressive uniaxial strains. At higher pressures, the shock sensitivity can be observe by the drastic change in enthalpy for the [111] direction, and the increase shear pressure for the <001> direction. Furthermore, the resolved increase in shear stresses for compression in all but the <111> and <110> directions at compressions below 20% volumetric strain value, could explain the difference observed between shock and impact sensitivities found from different studies.

In the case of PETN, the sensitivity at almost all pressures is observed from the non-monotonic energy behavior of the uniaxial compression. At higher compressions, we see a change in the electronic structure, as measured from the formal charges of the atoms involved in the initiation step for homolytic bond rupture. The formal charge of the nitro group and carbon atoms varies dramatically for the highest compressed state. This

indicates that for the extreme compressed states, initiation can me more easily achieved in preferential directions. For the case of NM, the formal charge of the nitro group varies less in the [101] direction, while there is a marked polarization for the [010] direction, which is observable in the change of the C atom. As expected for both cases there are a larger polarization in initiation bonds, at different pressures, and directions. Also, different relative values or charge can be observed for different values of uniaxial strain, which indicates that at different compressions (impact, vs. shock) the chemical environment of the strained system is highly anisotropic.

Localization of strain energy has long been the suspect of the formation of reaction zones and molecular changes in energetic materials, causing runaway reactions and unexpected initiation. A clear understanding of the mechanical properties is thus a perquisite in understanding the interplay between mechanical, chemical and thermodynamic properties that relate sensitivity and energetic materials before they undergo initiation. Relevant knowledge of the structure and properties of the material when subjected at extreme conditions is required. If constrained to the elastic behavior of the material, the method of the second derivative of the energy has the advantage of giving rather accurate results, as compared to stress derived elastic coefficients. In our case, we observe a discontinuity from the elastic behavior (as seen from the strain – energy curves) for the case of NM, at pressures above 3GPa. Although no available data on the elastic constants was available, the predicted higher sensitivity along the [001] direction, as predicted by the model of steric hindrance, is supported by the changes in

enthalpy observed from the uniaxial compression runs at 150K, and from the larger change in total energy from calculations in the limit of 0K.

Our calculated values for PETN agrees with the calculated by Gupta's group with sound speed experiments[363]. Values of the bulk modulus and its pressure derivative correspond well to the ones found experimentally by Ollinger and Cady[162]. Changes in both symmetry and elastic coefficients indicate that for pressures below 5GPa, there is crystal symmetry transformation. This can also be observed from changes in the lattice parameters, molecular structure and mechanical properties of the system. As opposed to NM and PETN, we found that the elastic properties of Fox-7 showd and increased stiffness. Nontheless, this enhanced mechanical properties, the relationship between softer shearing constatns and the anisotropic band gap closing indicated the sensitivity of this secondary energetic material to anisotropic stimulli.

We observed the structural behavior of TATB, with a planar layer arrangement in normal conditions, under hydrostatic compression. A change in the intermolecular hydrogen-bonding network is observed upon compression. This molecular rearrangement is systematically studied and characterized, from both gas phase and condensed phase studies. The number of hydrogen bonds along the 'Z' axis increases from 0 to 8, which is observed as an increase in the hydrogen bonding energy as well. From vibrational frequency studies, changes can bee seen in the nitro and amino group, as well as changes in the region of 100 cm^{-1} to 700 cm^{-1}. From gas phase calculations, the potential energy surface indicates the presence of two local minima within 3.42 Kcal/mol difference in energy, with a minima located at the conformation observed from

the structure under pressure. Correlation between reported spectroscopic data is reported. Even though this peculiar behavior does not induce a change of symmetry of the crystal unit cell, the inversion center within adjacent cells of different conformations is lost. In a contrasting behaviour, the insensitive TATB, revealed itself in an stiffenin upon compression.

Although the value of the C_{11} constant correlate directly with the experimentally observed sensitivity of the particular systems, (namely TATB>Fox-7>RDX>b-HM>PETN>NM, TATB, being the most insensitive), prediction of the reactivity and sensitivity of an explosive is complex since it depends on the interaction of mechanical, chemical and thermodynamic conditions. For a perfectly symmetric crystal, compression up to close the initiation pressure showed no signs of mechanical instability. Adiabatic compression showed the largest change in energy for β-HMX. We can correlate this energy requirement with the trend in sensitivity β-HMX<PETN<NM. Through the calculation of the effect of pressure upon band-gap closing, we can conclude that Metallization as the initiation step in an adiabatic uniaxial compression of a perfect crystals of Fox-7 and β-HMX cannot be excluded.

In addition to this, fractures along a given plane can act as energy barriers and hinder a complete reaction, causing unexpected behavior in some cases. Furhter studies on the effects of defects and grain boundaries can be further explore. This bearing in mind the need of the most stable satarting configuration, this is; stalk fault mapping. We can envision a study to understand the effect of defects, metal or cations that can act as external dopants and aide in the control the electronic properties of energetic materials.

Explicit modeling of the electronic degrees of freedom at finite temperatures has emerged as a possibility within the Car-Parrinello method. Here, dynamic behavior at different temperatures that govern the behavior of energetic materials can be studied. Processes like hydrogen bonding, structure evolution and preferential conformations can be easily observed. In our particular case study, fission of the C-NO_2 bond is identified as the initial step of nitroethane thermal decomposition. Further calculations directed towards differentiating the impact and shock sensitivities of Fox-7 under impact and shock compression can pursued.

The systematic understanding of different observed properties, like hydrogen bonding re-arrangement, anisotropic band gap closing, mechanical instabilities at given pressures, and other structural properties, like the pairing of NO_2-NH_3 could provide basis to a fundamental approach to express various properties of EM, like initiation pressure or impact sensitivities.

Studies on Prospective Systems

Due to the chemical, mechanical and thermodynamic level information that provides, multiscale modeling methods, can then be applied to the understanding of other type of systems and give a clearer understanding of the molecular processes that undergo energetic materials, prior to initiation. Based on known properties and structures, theoretical methods be applied to design new possible compounds with characteristics. The effect of crystal defects on the anisotropic mechanical response of the energetic materials under both hydrostatic and axial compression, and with the application of shock can also be approached. For example, complex non-stoichiometric materials like,

γ-AlON, which was first observed in experiments trying to find the stable structure of the Al_20_3 spinel[459] can be further studied. Nitrogen ions embedded in the crystal lattice, as opposed to the reduction of Al^{3+} to Al^{2+} were found responsible for this stabilization[460]. Due to its mechanical an optical properties[461-463] (i.e.; transparency) it under current study for applications in the area of armored defense[464]. Some of its recent applications include the use as a spin barrier for tunneling juntions[465], and high-K dielectric[466-468]. Its accumulation in alumina-alumina grain boundaries suggests its use as a wear protective film[469,470]. Some wear resistant si-alon glasses have also been reported[471]. This alloy can be found at a composition close to 35% AlN in the AlN-Alumina binary phase diagram[472,473]. Experimentally, this system is challenging since at temperatures close to its equilibrium conditions, AlN sublimes, while alumina melts[474]. Although there has been some efforts to develop a complete phase diagram, there are still many phases[472,475,476] and polytypoids[477] that need to be accounted for, and that have been observed experimentally[471]. In addition to this modulated phases, and the hability of Al to form different coordination structures[478], parameters like nitrogen vapor pressure and or oxygen concentration during synthesis[461] have shown to be influential in the observed phases, indicating the presence of vacancies and interstitials as possible sources of the non-stoichiometric forms found in literature[476,479,480]. There have been some efforts to change the young modulus and micro hardness of alumina surfaces by means of ion implantation[481,482] or incorporation with BN. For example; ALON and BN composites of ALON maintain their flexural strength (higher than 100MPa) in a large high temperature range[480] . In some cases, TiN and NiAl and CoGa are used as template

for the epitaxial growth of Alon films[483,484]. Young modulus and Poisson's ratios have been shown to be dependent on the lattice parameter of the Alon structure under study[485]. Although there are some reports on the elastic properties of Alon, these are isotropic values, and further investigations are needed[486].

As indicated by the relevance of the nitro and amino substituents, molecular crystal with nitrogen containing atoms[487] now pose a promising sub category of energetic materials. Advantages include a low exhaust temperature with high impulse, and complete combustion with mainly N_2 and H_2 as exhaust products. Low exhaust temperature also implies low traceability by current remote sensing applications. Based upon these preliminary findings, we propose electronic structure calculations to elucidate the solid state band-structure of each system, and the effect of different conformations/substituents. Trends in the family of tiazolium salts, as well as their amino and azido substituted relative compounds can be of interest. In order to probe the effects of the structure, the family of nitrogen rich extended ring systems, triazolim, tetrazolium, by-ciclic salts, utropinium, tetrazine will be compared. These higher volume salts seem to have increased stability to air, light and a low temperature emission.

Elasticity measurements for these compounds will be of special interest for compounds like cubane and azetidinium based compounds, versus aromatic nitrogen salts, like imidazole based compounds. Again, the advantage of multiscale methods should prove necessary in the detailed study this systems.

REFERENCES

(1) Jeacocke, J. In *Explosives in the Service of Man*; Dolan, J. E., Langer, S. S., Eds.; The Royal Society of Chemistry: Bath, 1997, p 21.

(2) *Organic Chemistry of Explosives*; Agrawal, J. P.; Hodgson, R. D. ed.; Wiley: Chichester, 2006.

(3) Zeman, S. In *High Energy Density Materials*; Klapötke, T., Ed.; Springer: Berlin, 2007; Vol. 125, p 195.

(4) Dick, J. J. *Applied Physics Letters* **1984**, *44*, 859.

(5) Dick, J. J. *Journal of Physical Chemistry* **1993**, *97*, 6193.

(6) Dick, J. J. *Journal of Applied Physics* **1997**, *81*, 601.

(7) *Chemistry and Physics of Energetic Materials*; Bulusu, S. N. ed.; Kluwer: Boston, 1990.

(8) *Lasl Explosive Property Data*; Gibbs, T. R.; Popolato, A.; Baytos, J. F. ed.; University of California Press Berkeley 1980.

(9) *Quantum-Mechanical Ab-Initio Calculation of the Properties of Crystalline Materials*; Pisani, C. ed.; Springer-Verlag: Berlin, 1996.

(10) *Continuum Mechanics: Concise Theory and Problems*; Chadwick, P. ed.; Dover: London, 1976.

(11) *Explosives;* 5th; Meyer, R.; Köler, J.; Homburg, A. ed.; Wiley-VCH: Berlin, 2002.

(12) *Detonation in Condensed Explosives*; Taylor, J.; Oxford, u. ed.; Clarendon press: Oxford, 1952.

(13) Lipinska-Kalita, K. E.; Pravica, M. G.; Nicol, M. *Journal of Physical Chemistry B* **2005**, *109*, 19223.

(14) *Computer Simulation of Liquids*; Allen, M. P.; Tildesley, D. J. ed.; Oxford University Press: Oxford, 1987.

(15) *Themodynamics*; Fermi, E. ed.; Dover Publications: New York, 1956.

(16) *Thermodynamics in Materials Science*; DeHoff, R. ed.; Taylor & Francis: Boca Raton, Fla., 2006.

(17) *Physics of Shock Waves and High-Temperature Hydrodynamic Phenomena*; Zel'dovich, Y. B.; Raizer, Y. P. ed.; Dover Publications: Mineola, N.Y., 2001.

(18) *Irreversible Phenomena: Ignitions, Combustion, and Detonation Waves*; Terao, K. ed.; Springer: Berlin; New York, 2007.

(19) Volker Weiser, S. K., Norbert Eisenreich, *Propellants, Explosives, Pyrotechnics* **2001**, *26*, 284.

(20) Campbell, A. W.; Holland, T. E.; Malin, M. E.; Cotter, T. P. *Nature* **1956**, *178*, 38.

(21) Dlott, D. D.; Peter, P.; Jane, S. M. In *Theoretical and Computational Chemistry*; Elsevier: Amsterdam, 2003; Vol. 13, p 125.

(22) *Molecular Orbital Theory for Organic Chemists*; Streitwieser, A. ed.; Wiley: New York, 1961.

(23) Sewell, T. D.; Menikoff, R.; Bedrov, D.; Smith, G. D. *The Journal of Chemical Physics* **2003**, *119*, 7417.

(24) *Lattice Dynamics of Molecular Crystals*; Califano, S.; Schettino, V.; Neto, N. ed.; Springer-Verlag: Berlin; New York, 1981.

(25) Miller, R. S. In *Decomposition, Combustion, and Detonation Chemistry of Energetic Materials*; 2nd ed.; Brill, T. B., Russell, T. P., Tao, W. C., Wardle, R. B., Eds.; Materials Research Society: Boston, 1995; Vol. 418, p 3.

(26) *Introduction to the Technology of Explosives;* 1st; Cooper, P. W.; Kurowski, S. R. ed.; VCH: New York, 1996.

(27) Sun, D. W.; Garimella, S. V.; Singh, S.; Naik, N. *Propellants Explosives Pyrotechnics* **2005**, *30*, 369.

(28) Firsich, D. W. *Journal of Hazardous Materials* **1984**, *9*, 133.

(29) Novozhilov, B. V. *Combustion Explosion and Shock Waves* **2005**, *41*, 709.

(30) Urtiew, P. A.; Tarver, C. M. *Combustion Explosion and Shock Waves* **2005**, *41*, 766.

(31) Patterson, J. E.; Lagutchev, A. S.; Hambir, S. A.; Huang, W.; Yu, H.; Dlott, D. D. *Shock Waves* **2005**, *14*, 391.

(32) Puduppakkam, K. V.; Beckstead, M. W. *Combustion Science and Technology* **2005**, *177*, 1661.

(33) Smith, G. D.; Bedrov, D.; Sewell, T. D.; Menikoff, R. *Journal of Chemical Physics* **2003**, *119*, 7417.

(34) Menikoff, R.; Sewell, T. D. In *LA-UR-00-3608-rev* Berkeley, 2001, p 15.

(35) Smith, G. D.; Sewell, T. D.; Bedrov, D.; Menikoff, R. In *Shock Compression of Condensed Matter*; AIP: 2001; Vol. Conf. Proc. No. 620.

(36) Menikoff, R.; Sewell, T. D. *Combustion Theory and Modeling* **2002**, *6*, 103.

(37) Cynn, H.; Choong-Shick, Y. *Journal of Chemical Physics* **1999**, *111*, 10229.

(38) Wu, C. J.; Ree, F. H.; Yoo, C.-S. *Propellants, Explosives, Pyrotechnics* **2004**, *29*, 296.

(39) Zhang, X.; Emge, T. J.; Ghosh, R.; Krogh-Jespersen, K.; Goldman, A. S. *Organometallics* **2006**, *25*, 1303.

(40) Arenas, J. F.; Otero, J. C.; Pelaez, D.; Soto, J.; Serrano-Andres, L. *Journal of Chemical Physics* **2004**, *121*, 4127.

(41) Wang, G.-X.; Xiao, H.-M.; Xu, X.-J.; Ju, X.-H. *Propellants, Explosives, Pyrotechnics* **2006**, *31*, 102.

(42) Raha, K.; Chhabra, J. S. *Journal of Hazardous Materials* **1993**, *34*, 385.

(43) Johnson, J. N. *Journal of Applied Physics* **1972**, *43*, 2074.

(44) Lynn, S.; Donald, R. C.; Donald, A. S. *Journal of Applied Physics* **1976**, *47*, 4814.

(45) Elban, W.; Armstrong, R.; Yoo, K.; Rosemeier, R.; Yee, R. *Journal of Materials Science* **1989**, *24*, 1273.

(46) Fried, L. E.; Manaa, M. R.; Pagoria, P. F.; Simpson, R. L. *Annual Review of Materials Research* **2001**, *31*, 291.

(47) Edwards, J.; Eybl, C.; Johnson, B. *International Journal of Quantum Chemistry* **2004**, *100*, 713.

(48) Armstrong, R. W.; Elban, W. L. In *Dislocations in Solids*; Nabarro, F. R. N., Hirth, J. P., Eds.; Elsevier: Amsterdam, 2005; Vol. Volume 12, p 403.

(49) Byrd, E. F. C.; Rice, B. M. *Journal of Physical Chemistry A* **2006**, *110*, 1005.

(50) McNesby, K. L.; Coffey, C. S. *The Journal of Physical Chemistry B* **1997**, *101*, 3097.

(51) Ye, S.; Tonokura, K.; Koshi, M. *Combustion and Flame* **2003**, *132*, 240.

(52) Zeman, S.; Krupka, M. *Propellants, Explosives, Pyrotechnics* **2003**, *28*, 301.

(53) Zeman, S. *Propellants, Explosives, Pyrotechnics* **2003**, *28*, 308.

(54) Kimmel, A. V.; Sushko, P. V.; Shluger, A. L.; Kuklja, M. M. *The Journal of Chemical Physics* **2007**, *126*, 234711.

(55) Manaa, M. R. *Applied Physics Letters* **2003**, *83*, 1352.

(56) Reed, E. J.; Riad Manaa, M.; Fried, L. E.; Glaesemann, K. R.; Joannopoulos, J. D. *Nature Physics* **2008**, *4*, 72.

(57) Wiegand, D. A.; Reddingius, B. *Journal of Energetic Materials* **2005**, *23*, 75.

(58) Dremin, A. N. *Philosophical Transactions: Physical Sciences and Engineering* **1992**, *339*, 355.

(59) Eyring, H. *Science* **1978**, *199*, 740.

(60) Cho, S. G.; No, K. T.; Goh, E. M.; Kim, J. K.; Shin, J. H.; Joo, Y. D.; Seong, S. *Bulletin of the Korean Chemical Society* **2005**, *26*, 399.

(61) Keshavarz, M. H.; Jaafari, M. *Propellants, Explosives, Pyrotechnics* **2006**, *31*, 216.

(62) Miller, M. S. In *Decomposition, Combustion, and Detonation Chemistry of Energetic Materials*; 2nd ed.; Brill, T. B., Russell, T. P., Tao, W. C., Wardle, R. B., Eds.; Materials Research Society: Boston, 1995; Vol. 418, p 3.

(63) Soto, M. R. In *Decomposition, Combustion, and Detonation Chemistry of Energetic Materials*; 2nd ed.; Brill, T. B., Russell, T. P., Tao, W. C., Wardle, R. B., Eds.; Materials Research Society: Boston, 1995; Vol. 418, p 3.

(64) White, C. T.; Barrett, J. J. C.; Mintmire, J. W.; Elert, M. L. In *Decomposition, Combustion, and Detonation Chemistry of Energetic Materials*; 2nd ed.; Brill, T. B., Russell, T. P., Tao, W. C., Wardle, R. B., Eds.; Materials Research Society: Boston, 1995; Vol. 418, p 3.

(65) Tsai, D. H. In *Decomposition, Combustion, and Detonation Chemistry of Energetic Materials*; 2nd ed.; Brill, T. B., Russell, T. P., Tao, W. C., Wardle, R. B., Eds.; Materials Research Society: Boston, 1995; Vol. 418, p 3.

(66) Soulard, L. In *Decomposition, Combustion, and Detonation Chemistry of Energetic Materials*; 2nd ed.; Brill, T. B., Russell, T. P., Tao, W. C., Wardle, R. B., Eds.; Materials Research Society: Boston, 1995; Vol. 418, p 3.

(67) Son, S. F.; Asay, B. W.; Bdzil, J. B.; Kober, E. M. In *Decomposition, Combustion, and Detonation Chemistry of Energetic Materials*; 2nd ed.; Brill, T. B., Russell, T. P., Tao, W. C., Wardle, R. B., Eds.; Materials Research Society: Boston, 1995; Vol. 418, p 3.

(68) Pinkerton, A. A.; Martin, A. In *Decomposition, Combustion, and Detonation Chemistry of Energetic Materials*; 2nd ed.; Brill, T. B., Russell, T. P., Tao, W. C., Wardle, R. B., Eds.; Materials Research Society: Boston, 1995; Vol. 418, p 3.

(69) Sewell, T. D. In *Decomposition, Combustion and Detonation Chemistry of Energetic Materials*; Brill, T. B., Russell, T. P., Tao, W. C., Wardle, R. B., Eds.; Materials Research Society: Boston, 1995, p 67.

(70) Boileau, J. In *Decomposition, Combustion, and Detonation Chemistry of Energetic Materials*; 2nd ed.; Brill, T. B., Russell, T. P., Tao, W. C., Wardle, R. B., Eds.; Materials Research Society: Boston, 1995; Vol. 418, p 3.

(71) Kunz, B. A. In *Decomposition, Combustion, and Detonation Chemistry of Energetic Materials*; 2nd ed.; Brill, T. B., Russell, T. P., Tao, W. C., Wardle, R. B., Eds.; Materials Research Society: Boston, 1995; Vol. 418, p 287.

(72) Cook, M. D.; Fellows, J.; Kaskins, P. J. In *Decomposition, Combustion, and Detonation Chemistry of Energetic Materials*; 2nd ed.; Brill, T. B., Russell, T. P., Tao, W. C., Wardle, R. B., Eds.; Materials Research Society: Boston, 1995; Vol. 418, p 3.

(73) Maharrey, S.; Behrens, R. *Journal of Physical Chemistry A* **2005**, *109*, 11236.

(74) Ju, X. H.; Xu, X. J.; Xiao, H. M. *Journal of Energetic Materials* **2005**, *23*, 121.

(75) Li, J. S.; Huang, Y. G.; Dong, H. S. *Journal of Energetic Materials* **2005**, *23*, 133.

(76) Xiao, H. M.; Ju, X. H.; Xu, L. N.; Fang, G. Y. *Journal of Chemical Physics* **2004**, *121*, 12523.

(77) Zhang, C. Y.; Shu, Y. J.; Zhao, X. D.; Dong, H. S.; Wang, X. F. *Journal of Molecular Structure-Theochem* **2005**, *728*, 129.

(78) Chen, C.; Wu, J. C. *Computers & Chemistry* **2001**, *25*, 117.

(79) Korolev, V. L.; Petukhova, T. V.; Pivina, T. S.; Sheremetev, A. B.; Miroshnichenko, E. A.; Ivshin, V. P. *Khimiya Geterotsiklicheskikh Soedinenii* **2004**, *12*, 1817.

(80) Qiu, L.; Xiao, H. M.; Ju, X. H.; Gong, X. D. *International Journal of Quantum Chemistry* **2005**, *105*, 48.

(81) Drake, G. W.; Hawkins, T. W.; Hall, L. A.; Boatz, J. A.; Brand, A. J. *Propellants Explosives Pyrotechnics* **2005**, *30*, 329.

(82) Moore, D. S.; Funk, D. J.; McGrane, S. D. In *Chemistry at Extreme Conditions;* 1st ed, Manaa, M. R., Ed.; Elsevier: Amsterdam, 2005, p 369.

(83) Zhao, Q. H.; Zhang, S. W.; Li, Q. S. *Chemical Physics Letters* **2005**, *412*, 317.

(84) Badders, N. R.; Wei, C.; Aldeeb, A. A.; Rogers, W. J.; Mannan, M. S. *Journal of Energetic Materials* **2006**, *24*, 17.

(85) Main, P. *Acta Crystalographica* **1985**, *C41*.

(86) Choi, S. C.; Boutin, H. P. *Acta Crystalographica* **1970**, *B26*, 1235.

(87) Brill, T. B.; Goetz, F. *The Journal of Chemical Physics* **1979**, *83*, 340.

(88) Pople, J. A.; von Rague Schleyer, P.; Kaneti, J.; Spitznagel, G. W. *Chemical Physics Letters* **1988**, *145*, 359.

(89) Lyman, J. L.; Liau, Y.-C.; Brand, H. V. *Combustion and Flame* **2002**, *130*, 185.

(90) Cobos, C. J. *Journal of Molecular Structure: THEOCHEM* **2005**, *714*, 147.

(91) Tokmakoff, A.; Fayer, M. D.; Dlott, D. D. *The Journal of Physical Chemistry* **1993**, *97*, 1901.

(92) Gusachenko, L. K.; Zarko, V. E. *Propellants Explosives Pyrotechnics* **2005**, *30*, 264.

(93) Nichols III, A. L.; Tarver, C. M.; Chidester, S. K. *Journal of Physical Chemistry* **1996**, *100*, 579.

(94) Holian, B. L.; Germann, T. C.; Strachan, A.; Maillet, J. B. In *Chemistry at Extreme Conditions;* 1st ed, Manaa, M. R., Ed.; Elsevier: Amsterdam, 2005, p 269.

(95) Kozak, G. D. *Propellants Explosives Pyrotechnics* **2005**, *30*, 291.

(96) Liu, X. Y.; Wang, X. C.; Huang, Y. G.; Zheng, M. X.; Wang, L.; Jiang, Y.; Luo, Y. W. *Spectroscopy and Spectral Analysis* **2006**, *26*, 251.

(97) Kohn, W.; Sham, L. J. *Physical Review* **1965**, *140*, A1133.

(98) Perdew, J. P.; Burke, K.; Ernzerhof, M. *Physical Review Letters* **1996**, *77*, 3865.

(99) Troullier, N.; Martins, J. L. *Physical Review B* **1991**, *43*, 1993.

(100) Kresse, G.; Hafner, J. *Physical Review B* **1993**, *47*, 558.

(101) Kresse, G.; Furthmüller, J. *Computational Materials Science* **1996**, *6*, 15.

(102) Kresse, G.; Furthmüller, J. *Physical Review B* **1996**, *54*, 11169.

(103) Kresse, G.; Hafner, J. *Journal of Physics: Condensed Matter* **1994**, 8245.

(104) Kresse, G.; Joubert, D. *Physical Review B* **1999**, *59*, 1758.

(105) Gatti, C.; Saunders, V. R.; Roetti, C. *The Journal of Chemical Physics* **1994**, *101*, 10686.

(106) Dovesi, R.; Saunders, V. R.; Roetti, C.; Orlando, R.; Zicovich-Wilson, C. M.; Pascale, F.; Civalleri, B.; Doll, K.; Harrison, N. M.; Bush, I. J.; D'Arco, P.; Llunell, M.; www.crystal.unito.it: 2007.

(107) CCSDT In *Cambridge Structural Database*; CCSD: 2007.

(108) Ledoux, I.; Zyss, J.; Siegel, J. S.; Brienne, J.; Lehn, J. M. *Chemical Physics Letters* **1990**, *172*, 440.

(109) Dunning, J. T. H. *The Journal of Chemical Physics* **1989**, *90*, 1007.

(110) Yang, G.; Nie, F.; Huang, H.; Zhao, L.; Pang, W. *Propellants, Explosives, Pyrotechnics* **2006**, *31*, 390.

(111) Boddu, V. M.; Viswanath, D. S.; Ghosh, T. K.; Damavarapu, R. *Journal of Hazardous Materials* **2010**, *181*, 1.

(112) Goodson, D. Z. *The Journal of Chemical Physics* **2002**, *116*, 6948.

(113) Zicovich-Wilson, C. M.; Pascale, F.; Roetti, C.; Saunders, V. R.; Orlando, R.; Dovesi, R. *Journal of Computational Chemistry* **2004**, *25*, 888.

(114) Pascale, F.; Zicovich-Wilson, C. M.; López Gejo, F.; Civalleri, B.; Orlando, R.; Dovesi, R. *Journal of Computational Chemistry* **2004**, *25*, 888.

(115) Zicovich-Wilson, C. M.; Dovesi, R.; Saunders, V. R. *The Journal of Chemical Physics* **2001**, *115*, 9708.

(116) Valeev, E. F.; Allen, W. D.; Hernandez, R.; Sherrill, C. D.; Schaefer Iii, H. F. *The Journal of Chemical Physics* **2003**, *118*, 8594.

(117) Mayo, S. L.; Olafson, B. D.; Goddard, W. A. *The Journal of Physical Chemistry* **1990**, *94*, 8897.

(118) Hagler, A. T.; Huler, E.; Lifson, S. *Journal of the American Chemical Society* **1974**, *96*, 5319.

(119) Hagler, A. T.; Lifson, S. *Journal of the American Chemical Society* **1974**, *96*, 5327.

(120) Lifson, S.; Hagler, A. T.; Dauber, P. *Journal of the American Chemical Society* **1979**, *101*, 5111.

(121) Hagler, A. T.; Lifson, S.; Dauber, P. *Journal of the American Chemical Society* **1979**, *101*, 5122.

(122) Kitson, D. H.; Hagler, A. T. *Biochemistry* **1988**, *27*, 5246.

(123) Hagler, A. T.; Dauber, P.; Lifson, S. *Journal of the American Chemical Society* **1979**, *101*, 5131.

(124) Kitson, D. H.; Hagler, A. T. *Biochemistry* **1988**, *27*, 7176.

(125) Pnina Dauber-Osguthorpe, V. A. R., David J. Osguthorpe, Jon Wolff, Moniqe Genest, Arnold T. Hagler, *Proteins: Structure, Function, and Genetics* **1988**, *4*, 31.

(126) Sun, H. *The Journal of Physical Chemistry B* **1998**, *102*, 7338.

(127) Sun, H.; Ren, P.; Fried, J. R. *Computational and Theoretical Polymer Science* **1998**, *8*, 229.

(128) David Rigby, H. S., B. E. Eichinger, *Polymer International* **1997**, *44*, 311.

(129) Sun, H.; Rigby, D. *Spectrochimica Acta Part A: Molecular and Biomolecular Spectroscopy* **1997**, *53*, 1301.

(130) Rappe, A. K.; Casewit, C. J.; Colwell, K. S.; Goddard, W. A.; Skiff, W. M. *Journal of the American Chemical Society* **1992**, *114*, 10024.

(131) Rappe, A. K.; Goddard, W. A. *The Journal of Physical Chemistry* **1991**, *95*, 3358.

(132) Mulliken, R. S. *The Journal of Chemical Physics* **1955**, *23*, 1833.

(133) Plimpton, S. *Journal of Computational Physics* **1995**, *117*, 1.

(134) Martyna, G. J.; Tobias, D. J.; Klein, M. L. *Journal of Chemical Physics* **1994**, *101*, 4177.

(135) Parrinello, M.; Rahman, A. *Journal of Applied Physics* **1981**, *52*, 7182.

(136) Perger, W. F.; Pandey, R.; Blanco, A. M.; Zhao, J. *Chemical Physics Letters* **2004**, *388*, 175.

(137) Dewar, M. J. S.; Ritchie, J. P. *Journal of Organic Chemistry* **1985**, 1031.

(138) McKee, M. L. *Journal of the American Chemical Society* **1986**, *108*, 5784.

(139) Liu, F.-C.; Hu, W.-F.; He, T.-J.; Chen, D.-M. *Journal of Physical Chemistry A* **2002**, *106*, 7294.

(140) Nguyen, M. T.; Le, H. T.; Hajgato, B.; Veszpremi, T.; Lin, M. C. *Journal of Physical Chemistry A* **2003**, *107*, 4286.

(141) McClellan, J. J.; Hughes, T. F.; Bartlett, R. J. *International Journal of Quantum Chemistry* **2005**, *105*, 914.

(142) Gruzdkov, Y. A.; Dreger, Z. A.; Gupta, Y. M. *The Journal of Physical Chemistry A* **2004**, *108*, 6216.

(143) Kim, C. K.; Lee, K. A.; Hyun, K. H.; Park, H. J.; Kwack, I. Y.; Kim, C. K.; Lee, H. W.; Lee, B. S. *Journal of Computational Chemistry* **2004**, *25*, 2073.

(144) Zhang, Y. X.; Liu, D. B.; Lv, C. X. *Propellants Explosives Pyrotechnics* **2005**, *30*, 438.

(145) Quinet, O.; Champagne, B. *International Journal of Quantum Chemistry* **2001**, *85*, 463.

(146) Cady, H. H.; Larson, A. C.; Cromer, D. T. *Acta Crystallographica* **1963**, *16*, 617.

(147) Yoo, C.-S.; Cynn, H. *The Journal of Chemical Physics* **1999**, *111*, 10229.

(148) Stevens, L. L.; Eckhardt, C. J. *The Journal of Chemical Physics* **2005**, *122*, 174701.

(149) Bemm, U.; Ostmark, H. *Acta Crystallographica Section C* **1998**, *54*, 1997.

(150) Evers, J.; Klapotke, T. M.; Mayer, P.; Oehlinger, G.; Welch, J. *Inorganic Chemistry* **2006**, *45*, 4996.

(151) Meents, A.; Dittrich, B.; Johnas, S. K. J.; Thome, V.; Weckert, E. F. *Acta Crystallographica Section B* **2008**, *64*, 519.

(152) Meents, A.; Dittrich, B.; Johnas, S. K. J.; Thome, V.; Weckert, E. F. *Acta Crystallographica Section B* **2008**, *64*, 42.

(153) Gilardi, R. D.; George, C. F. In *Cambridge Structural Database*; The Cambridge Crystallographic Data Centre: 1984.

(154) Cady, H. H.; Larson, A. C. *Acta Crystallographica* **1965**, *18*, 485.

(155) John R. Kolb, H. F. R. *Propellants, Explosives, Pyrotechnics* **1979**, *4*, 10.

(156) Bower, J. K.; Kolb, J. R.; Pruneda, C. O. *Industrial & Engineering Chemistry Product Research and Development* **1980**, *19*, 326.

(157) Lewis L. Stevens, N. V., Daniel E. Hooks, Dana M. Dattelbaum, *Propellants, Explosives, Pyrotechnics* **2008**, *33*, 286.

(158) Trevino, S. F.; Prince, E.; Hubbard, C. R. *The Journal of Chemical Physics* **1980**, *73*, 2996.

(159) Cromer, D. T.; Ryan, R. R.; Schiferl, D. *The Journal of Physical Chemistry* **1985**, *89*, 2315.

(160) Bagryanskaya, I. Y.; Gatilov, Y. V. *Journal of Structural Chemistry* **1983**, *24*, 150.

(161) Olinger, B.; Cady, H. H. In *Sixth symposium on detonation*; Edwards, D. J., Jacobs, S. J., Eds.; Office of Naval Research: Coronado, California, 1976.

(162) Olinger, B.; Halleck, P. M.; Cady, H. H. *The Journal of Chemical Physics* **1975**, *62*, 4480.

(163) CCSDT In *Cambridge Crystallographic Database*; PERYTN11: 2001.

(164) Booth, A. D.; Llewellyn *J. Chem. Soc.* **1947**, *1947*, 837.

(165) Coleburn, N. L.; T. P. Liddiard, J. *The Journal of Chemical Physics* **1966**, *44*, 1929.

(166) Coleburn, N. L. *The Journal of the Acoustical Society of America* **1970**, *47*, 269.

(167) Stevens, L. L.; Velisavljevic, N.; Hooks, D. E.; Dattelbaum, D. M. *Applied Physics Letters* **2008**, *93*, 081912.

(168) Golovina, N. I.; Titkov, A. N.; Raevskii, A. V.; Atovmyan, L. O. *Journal of Solid State Chemistry* **1994**, *113*, 229.

(169) Brown, J. M.; Slutsky, L. J.; Nelson, K. A.; Cheng, L.-T. *Science* **1988**, *241*, 65.

(170) Cox, E. G. *Reviews of Modern Physics* **1958**, *30*, 159.

(171) Bacon, G. E.; Curry, N. A.; Wilson, S. A. *Proceedings of the Royal Society of London. Series A, Mathematical and Physical Sciences* **1964**, *279*, 98.

(172) Jeffrey, G. A.; Ruble, J. R.; McMullan, R. K.; Pople, J. A. *Proceedings of the Royal Society of London. Series A, Mathematical and Physical Sciences* **1987**, *414*, 47.

(173) Swaminathan, S.; Craven, B. M.; McMullan, R. K. *Acta Crystallographica Section B* **1984**, *40*, 300.

(174) Fischer, G.; Zarembow.J *Comptes Rendus Hebdomadaires Des Seances De L Academie Des Sciences Serie B* **1970**, *270*, 852.

(175) Haussuhl, S. *Zeitschrift für Kristallographie* **2001**, *216*, 339.

(176) Boldyreva, E. V. *Journal of Molecular Structure* **2003**, *647*, 159.

(177) Day, G. M.; Price, S. L.; Leslie, M. *Crystal Growth & Design* **2001**, *1*, 13.

(178) Boldyreva, E. *Acta Crystallographica Section A* **2008**, *64*, 218.

(179) Song, D. Y.; Holtz, M.; Chandolu, A.; Nikishin, S. A.; Mokhov, E. N.; Makarov, Y.; Helava, H. *Applied Physics Letters* **2006**, *89*, 21901.

(180) Figueroa, U.; Salas, O.; Oseguera, J. *Thin Solid Films* **2004**, *469-470*, 295.

(181) Wu, Z.; Chen, X.-J.; Struzhkin, V. V.; Cohen, R. E. *Physical Review B (Condensed Matter and Materials Physics)* **2005**, *71*, 214103.

(182) Lopez, G.; Staia, M. H. *Surface and Coatings Technology* **2005**, *200*, 2092.

(183) Lambrecht, W. R. L.; Miao, M. S.; Lukashev, P. In *49th Annual Conference on Magnetism and Magnetic Materials*; 10 ed.; AIP: Jacksonville, Florida (USA), 2005; Vol. 97, p 10D306.

(184) Bazhanov, D. I.; Knizhnik, A. A.; Safonov, A. A.; Bagatur'yants, A. A.; Stoker, M. W.; Korkin, A. A. *Journal of Applied Physics* **2005**, *97*, 044108.

(185) Bazhanov, D. I.; Safonov, A. A.; Bagatur'yants, A. A.; Korkin, A. A. In *Micro- and Nanoelectronics 2003*; 1 ed.; SPIE: 2004; Vol. 5401, p 418.

(186) *Properties of Advanced Semiconductor Materials : Gan, Ain, Inn, Bn, Sic, Sige*; Levinstein, M. E. ed.; John Wiley & Sons: New York, 2001.

(187) Ferreira da Silva, A.; Souza Dantas, N.; de Almeida, J. S.; Ahuja, R.; Persson, C. *Journal of Crystal Growth* **2005**, *281*, 151.

(188) Gusev, A. *Doklady Akademil nauk* **1997**, *357*, 490.

(189) Hu, Q.; Noda, T.; Tanigawa, H.; Yoneoka, T.; Tanaka, S. *Nuclear Instruments and Methods in Physics Research Section B: Beam Interactions with Materials and Atoms* **2002**, *191*, 536.

(190) M. Lerch, E. F. J. W. *Zeitschrift fur Anorganische und Allgemeine Chemie* **1996**, *622*, 367.

(191) Levy, F.; Hones, P.; Schmid, P. E.; Sanjines, R.; Diserens, M.; Wiemer, C. *Surface and Coatings Technology* **1999**, *120-121*, 284.

(192) Christensen, N. E. *Physical Review B* **1994**, *50*, 4397.

(193) Kuramoto, N.; Takada, K. *Key Engineering Materials* **2003**, *247*, 467.

(194) Zhang, Y.; Huang, L.; Arunagiri, T. N.; Ojeda, O.; Flores, S.; Chyan, O.; Wallace, R. M. *Electrochemical and Solid-State Letters.* **2004**, *7*, C107.

(195) *Interfacial Study of Copper Electrodeposition with the Electrochemical Quartz Crystal Microbalance*; Ojeda Mota, O. U. ed.; University of North Texas: [Denton, Tex.], 2005.

(196) Stejskal, J.; Leitner, K. *Chemicke Listy* **2002**, *5*, 311.

(197) Stampfl, C.; Mannstadt, W.; Asahi, R.; Freeman, A. J. *Physical Review B* **2001**, *63*, 155106.

(198) Ching, W. Y.; Xu, Y.-N.; Ouyang, L. *Physical Review B* **2002**, *66*, 235106.

(199) Zhao, M.; Xia, Y.; Liu, X.; Tan, Z.; Huang, B.; Song, C.; Mei, L. *The Journal of Physical Chemistry B* **2006**, *110*, 8764.

(200) Lepkowski, S. P.; Majewski, J. A.; Jurczak, G. *Physical Review B (Condensed Matter and Materials Physics)* **2005**, *72*, 245201.

(201) Merad, A. E.; Kanoun, M. B.; Cibert, J.; Aourag, H.; Merad, G. *Materials Chemistry and Physics* **2003**, *82*, 471.

(202) Ching, W. Y.; Harmon, B. N. *Physical Review B* **1986**, *34*, 5305.

(203) Wright, A. F. *Physical Review B* **1995**, *51*, 7866.

(204) Sedmidubsky, D.; Leitner, J. *Journal of Crystal Growth* **2006**, *286*, 66.

(205) Blöchl, P. E. *Physical Review B* **1994**, *50*, 17953.

(206) Kresse, G.; Joubert, J. *Physical Review B* **1999**, *59*, 1758.

(207) Becker, K. *Zeitschrif fur Physik* **1925**, *31*, 268.

(208) van Arkel, A. *Physica; Nederlandsch Tijdschrift voor Naturkunde* **1924**, *4*, 286.

(209) Lerch, M.; Fügein, E.; Wrba, J. *Zeitschrift fur Anorganische und Allgemeine Chemie* **1996**, 367.

(210) Werner H. Baur, M. L. *Zeitschrift fur Anorganische und Allgemeine Chemie* **1996**, *622*, 1729.

(211) Jeffrey, G. A.; Wu, V. Y. *Acta Crystallographica* **1963**, *16*, 559.

(212) Mair, S. L.; Zwi, B. *Acta Crystallographica A* **1975**, *31*, 201.

(213) Schulz, H.; Thiemann, K. H. *Solid State Communications* **1977**, *23*, 815.

(214) Meng, W. J. In *Properties of Group Iii Nitrides*; Edgar, J. H., Ed.; INSPEC: London, 1994, p 22.

(215) Ueno, M.; Onodera, A.; Shimomura, O.; Takemura, K. *Physical Review B* **1992**, *45*, 10123.

(216) *Crystal Structure;* 2nd; Wyckoff, R. W. G. ed.; Wiley Interscience: New York, 1963; Vol. 1.

(217) Xu, Y.-N.; Ching, W. Y. *Physical Review B* **1993**, *48*, 4335.

(218) Clearfield, A.; Blessing, R. H.; Stynes, J. A. *Journal of Inorganic and Nuclear Chemistry* **1968**, *30*, 2249.

(219) Clearfield, A.; Smith, G. D. *Inorganic Chemistry* **1969**, *8*, 431.

(220) Poojary, D. M.; Clearfield, A. *Inorganic Chemistry* **1994**, *33*, 3685.

(221) Poojary, D. M.; Vermeulen, L. A.; Vicenzi, E.; Clearfield, A.; Thompson, M. E. *Chemistry of Materials* **1994**, *6*, 1845.

(222) Yamai, I.; Oota, T. *Journal of the American Ceramic Society* **1985**, *68*, 273.

(223) Thompson, M. E. *Chemistry of Materials* **1994**, *6*, 1168.

(224) Cao, G.; Hong, H. G.; Mallouk, T. E. *Accounts of Chemical Research* **1992**, *25*, 420.

(225) Shimodaira, Y.; Miura, T.; Kudo, A.; Kobayashi, H. *Journal of Chemical Theory and Computation* **2007**, *3*, 789.

(226) Dickson, S. J.; Wallace, E. V. B.; Swinburne, A. N.; Paterson, M. J.; Lloyd, G. O.; Beeby, A.; Belcher, W. J.; Steed, J. W. *New Journal of Chemistry* **2008**, *32*, 786.

(227) Kumada, N.; Nakatani, T.; Yonesaki, Y.; Takei, T.; Kinomura, N. *Journal of Materials Science* **2008**, *43*, 2206.

(228) Saielli, G. *The Journal of Physical Chemistry A* **2008**, *112*, 7987.

(229) Causin, V.; Saielli, G. *Journal of Molecular Liquids* **2009**, *145*, 41.

(230) Wallis, D.; Claffey, J.; Gleeson, B.; Hogan, M.; Müller-Bunz, H.; Tacke, M. *Journal of Organometallic Chemistry* **2009**, *694*, 828.

(231) Wang, D.; Crowe, W. E.; Strongin, R. M.; Sibrian-Vazquez, M. *Chemical Communications* **2009**, 1876.

(232) Vermeulen, L. A.; Snover, J. L.; Sapochak, L. S.; Thompson, M. E. *Journal of the American Chemical Society* **1993**, *115*, 11767.

(233) Vermeulen, L. A.; Thompson, M. E. *Nature* **1992**, *358*, 656.

(234) Dokoutchaev, A.; Krishnan, V. V.; Thompson, M. E.; Balasubramanian, M. *Journal of Molecular Structure* **1998**, *470*, 191.

(235) Clearfield, A. *Chemical Reviews* **1988**, *88*, 125.

(236) Byrd, H.; Clearfield, A.; Poojary, D.; Reis, K. P.; Thompson, M. E. *Chemistry of Materials* **1996**, *8*, 2239.

(237) Poojary, D. M.; Shpeizer, B.; Clearfield, A. *Journal of the Chemical Society-Dalton Transactions* **1995**, 111.

(238) Nielsen, O. H.; Martin, R. M. *Physical Review B* **1985**, *32*, 3792.

(239) Nielsen, O. H.; Martin, R. M. *Physical Review B* **1985**, *32*, 3780.

(240) Hohenberg, P.; Kohn, W. *Physical Review* **1964**, *136*, B864.

(241) Kroll, P.; Schröter, T.; Peters, M. *Angewandte Chemie International Edition* **2005**, *44*, 4249.

(242) Wang, H.; Li, M. *Physical Review B (Condensed Matter and Materials Physics)* **2009**, *79*, 224102.

(243) Zhao, J.; Winey, J. M.; Gupta, Y. M. *Physical Review B (Condensed Matter and Materials Physics)* **2007**, *75*, 094105.

(244) Lopuszynski, M.; Majewski, J. A. *Physical Review B (Condensed Matter and Materials Physics)* **2007**, *76*, 045202.

(245) Zhang, R. F.; Veprek, S.; Argon, A. S. *Applied Physics Letters* **2007**, *91*, 201914.

(246) Zhang, R. F.; Sheng, S. H.; Veprek, S. *Applied Physics Letters* **2007**, *90*, 191903.

(247) Nagao, S.; Nordlund, K.; Nowak, R. *Physical Review B (Condensed Matter and Materials Physics)* **2006**, *73*, 144113.

(248) Aouadi, S. M. *Journal of Applied Physics* **2006**, *99*, 053507.

(249) Chen, X.-J.; Struzhkin, V. V.; Wu, Z.; Somayazulu, M.; Qian, J.; Kung, S.; Christensen, A. N.; Zhao, Y.; Cohen, R. E.; Mao, H.-k.; Hemley, R. J. *Proceedings of the National Academy of Sciences of the United States of America* **2005**, *102*, 3198.

(250) Hamann, D. R.; Wu, X.; Rabe, K. M.; Vanderbilt, D. *Physical Review B (Condensed Matter and Materials Physics)* **2005**, *71*, 035117.

(251) Li, W.; Wang, T. *Journal of Physics: Condensed Matter* **1998**, *10*, 9889.

(252) Sun, Y.; Kaxiras, E. *Philosophical Magazine A* **1997**, *75*, 1117

(253) Carvajal Diaz, J. A.; Cagin, T. *Nanotechnology* **2010**, *21*, 115703.

(254) Zhao, E.; Wu, Z. *Journal of Solid State Chemistry* **2008**, *181*, 2814.

(255) Steinle-Neumann, G.; Stixrude, L.; Cohen, R. E.; Gulseren, O. *Nature* **2001**, *413*, 57.

(256) Sarrao, J. L.; Mandrus, D.; Migliori, A.; Fisk, Z.; Bucher, E. *Physica B: Condensed Matter* **1994**, *199-200*, 478.

(257) Watanabe, H.; Yamamoto, H.; Ito, K.-i. *Journal of the Physical Society of Japan* **1963**, *18*, 995.

(258) Whitaker, M. L.; Liu, W.; Liu, Q.; Wang, L. P.; Li, B. S. *American Mineralogist* **2009**, *94*, 1039.

(259) Whitaker, M. L.; Liu, W.; Liu, Q.; Wang, L. P.; Li, B. S. In *International Workshop on Synchrotron High-Pressure Mineral Physics and Materials Science*; Irifune, T., Wang, Y., Eds.; Taylor & Francis Ltd: Argonne, Illinois, 2008, p 385.

(260) Wood, I. G.; Chaplin, T. D.; David, W. I. F.; Hull, S.; Price, G. D.; Street, J. N. *Journal of Physics-Condensed Matter* **1995**, *7*, L475.

(261) Vocadlo, L.; Price, G. D.; Wood, I. G. *Acta Crystallographica Section B-Structural Science* **1999**, *55*, 484.

(262) Zinoveva, G. P.; Andreeva, L. P.; Geld, P. V. *Physica Status Solidi (a)* **1974**, *23*, 711.

(263) Pauling, L.; Soldate, A. M. *Acta Crystallographica* **1948**, *1*, 212.

(264) *Treatise on the Mathematical Theory of Elasticity*; Love, A. E. H. ed.; University Press: Cambridge, U.K. 1927.

(265) *Continuum Mechanics*; Spencer, A. J. M. ed.; Longman: London, 1980.

(266) Fan, C. F.; Cagin, T.; Chen, Z. M.; Smith, K. A. *Macromolecules* **2002**, *27*, 2383.

(267) Ojeda, O. U.; Sevik, C.; Cagin, T. *Journal of Computational Materials Science* **2011**, *Submitted*.

(268) Zhang, R. F.; Sheng, S. H.; Veprek, S. *Applied Physics Letters* **2007**, *91*, 031906.

(269) Zhang, M.; He, J. *Surface and Coatings Technology* **2001**, *142-144*, 125.

(270) Benckert, S. *Physica Status Solidi (b)* **1971**, *43*, 681.

(271) Mehl, M. J. *Physical Review B* **1993**, *47*, 2493.

(272) Mehl, M. J.; Osburn, J. E.; Papaconstantopoulos, D. A.; Klein, B. M. *Physical Review B* **1990**, *41*, 10311.

(273) Ceperley, D. M.; Alder, B. J. *Physical Review Letters* **1980**, *45*, 566.

(274) Gonze, X.; Rignanese, G. M.; Verstraete, M.; Beuken, J. M.; Pouillon, Y.; Caracas, R.; Jollet, F.; Torrent, M.; Zerah, G.; Mikami, M.; Ghosez, P.; Veithen, M.; Raty, J. Y.; Olevanov, V.; Bruneval, F.; Reining, L.; Godby, R.; Onida, G.; Hamann, D. R.; Allan, D. C. *Zeitschrift für Kristallographie* **2005**, *220*, 558.

(275) Gonze, X.; Beuken, J. M.; Caracas, R.; Detraux, F.; Fuchs, M.; Rignanese, G. M.; Sindic, L.; Verstraete, M.; Zerah, G.; Jollet, F.; Torrent, M.; Roy, A.; Mikami, M.; Ghosez, P.; Raty, J. Y.; Allan, D. C. *Computational Materials Science* **2002**, *25*, 478.

(276) Goedecker, S. *SIAM Journal on Scientific Computing* **1997**, *18*, 1605.

(277) Payne, M. C.; Teter, M. P.; Allan, D. C.; Arias, T. A.; Joannopoulos, J. D. *Reviews of Modern Physics* **1992**, *64*, 1045.

(278) Fuchs, M.; Scheffler, M. *Computer Physics Communications* **1999**, *119*, 67.

(279) Suzuki, T. *Physical Review B* **1971**, *3*, 4007.

(280) *The Elastic Constants of Crystals*; Huntington, H. B. ed.; Academic Press: New York, 1958.

(281) Gerlich, D.; Fisher, E. S. *Journal of Physics and Chemistry of Solids* **1969**, *30*, 1197.

(282) Leigh, R. S. *Philosophical Magazine Series 7* **1951**, *42*, 139

(283) Pham, H. H.; Cagin, T. *Computers Materials & Continua* **2010**, *16*, 175.

(284) Ojeda, O. U.; Cagin, T. *Computers, Materials, & Continua* **2010**, *16*, 127.

(285) Mermin, N. D. *Physical Review* **1965**, *137*, A1441.

(286) Fu, C. L.; Ho, K. M. *Physical Review B* **1983**, *28*, 5480.

(287) Methfessel, M.; Paxton, A. T. *Physical Review B* **1989**, *40*, 3616.

(288) Marzari, N. Thesis (Ph. D.), University of Cambridge, 1996.

(289) Blochl, P. E.; Jepsen, O.; Andersen, O. K. *Physical Review B* **1994**, *49*, 16223.

(290) Bengone, O.; Alouani, M.; Blöchl, P.; Hugel, J. *Physical Review B* **2000**, *62*, 16392.

(291) Louail, L.; Maouche, D.; Roumili, A.; Ali Sahraoui, F. *Materials Letters* **2004**, *58*, 2975.

(292) Birch, F. *Physical Review* **1947**, *71*, 809.

(293) Li, J. H.; Liang, S. H.; Guo, H. B.; Liu, B. X. *Applied Physics Letters* **2005**, *87*, 194111.

(294) Çagin, T.; Ray, J. R. *Physical Review B* **1988**, *37*, 699.

(295) Sutton, P. M. *Physical Review* **1953**, *91*, 816.

(296) Kamm, G. N.; Alers, G. A. *Journal of Applied Physics* **1964**, *35*, 327.

(297) Thomas, J. F. *Physical Review* **1968**, *175*, 955.

(298) Sarma, V. P. N.; Reddy, P. J. *Physica Status Solidi (a)* **1972**, *10*, 563.

(299) *Ab Initio Molecular Dynamics : Basic Theory and Advanced Methods*; Marx, D.; Hutter, J. ed.; Cambridge University Press: Cambridge; New York, 2009.

(300) *Numerical Modeling of Explosives and Propellants*; Mader, C. L. ed.; CRC Press: Boca Raton, Fla., 1998.

(301) Gan, C. K.; Sewell, T. D.; Challacombe, M. *Physical Review B* **2004**, *69*, 035116 1.

(302) Byrd, E. F. C.; Scuseria, G. E.; Chabalowski, C. F. *Journal of Physical Chemistry B* **2004**, *108*, 13100.

(303) Ojeda, O. U.; Araujo, R. A.; Uludogan, M.; Cagin, T.; Wang, H. *Journal of Alloys and Compounds* **2011**, *Submitted*.

(304) Grimme, S.; Antony, J.; Schwabe, T.; Muck-Lichtenfeld, C. *Organic & Biomolecular Chemistry* **2007**, *5*, 741.

(305) Tsuzuki, S.; Luthi, H. P. *The Journal of Chemical Physics* **2001**, *114*, 3949.

(306) Tao, J.; Perdew, J. P. *The Journal of Chemical Physics* **2005**, *122*, 114102.

(307) Suzuki, S.; Green, P. G.; Bumgarner, R. E.; Dasgupta, S.; Goddard, W. A., III; Blake, G. A. *Science* **1992**, *257*, 942.

(308) Ziambras, E.; Kleis, J.; Schroder, E.; Hyldgaard, P. *Physical Review B* **2007**, *76*, 155425.

(309) Goursot, A.; Mineva, T.; Kevorkyants, R.; Talbi, D. *J. Chem. Theory Comput.* **2007**, *3*, 755.

(310) Byrd, E. F. C.; Rice, B. M. *J. Phys. Chem. C* **2007**, *111*, 2787.

(311) Hemmi, N.; Dreger, Z. A.; Gruzdkov, Y. A.; Winey, J. M.; Gupta, Y. M. *J. Phys. Chem. B* **2006**, *110*, 20948.

(312) Wu, X.; Vargas, M. C.; Nayak, S.; Lotrich, V.; Scoles, G. *The Journal of Chemical Physics* **2001**, *115*, 8748.

(313) Kurita, N.; Inoue, H.; Sekino, H. *Chemical Physics Letters* **2003**, *370*, 161.

(314) Stefan, G. *Journal of Computational Chemistry* **2004**, *25*, 1463.

(315) Thonhauser, T.; Cooper, V. R.; Li, S.; Puzder, A.; Hyldgaard, P.; Langreth, D. C. *Physical Review B (Condensed Matter and Materials Physics)* **2007**, *76*, 125112.

(316) Chakarova, S. D.; Schroder, E. *The Journal of Chemical Physics* **2005**, *122*, 054102.

(317) Kleis, J.; Schroder, E. *The Journal of Chemical Physics* **2005**, *122*, 164902.

(318) Xu, X.; Goddard, W. A., III *Proceedings of the National Academy of Sciences of the United States of America* **2004**, *101*, 2673.

(319) Engel, E. In *A Primer in Density Functional Theory*; Fiolhais, C., Nogueira, F., Marques, M., Eds.; Springer: Berlin, 2003.

(320) Qin Wu, H. O.; Weitao, Y. *Journal of Theoretical & Computational Chemistry* **2003**, *2*, 627.

(321) Ortmann, F.; Bechstedt, F.; Schmidt, W. G. *Physical Review B (Condensed Matter and Materials Physics)* **2006**, *73*, 205101.

(322) Gonzalez, C.; Lim, E. C. *Journal of Physical Chemistry A* **2003**, *107*, 10105.

(323) Bachorz, R. A.; Bischoff, F. A.; Hofener, S.; Klopper, W.; Ottiger, P.; Leist, R.; Frey, J. A.; Leutwyler, S. *Physical Chemistry Chemical Physics* **2008**, *10*, 2758.

(324) Hepburn, J.; Scoles, G.; Penco, R. *Chemical Physics Letters* **1975**, *36*, 451.

(325) LeSar, R. *The Journal of Physical Chemistry* **1984**, *88*, 4272.

(326) Marcus, E.; Pavel, H.; Thomas, F.; Sandor, S.; Efthimios, K. *The Journal of Chemical Physics* **2001**, *114*, 5149.

(327) Williams, R. W.; Malhotra, D. *Chemical Physics* **2006**, *327*, 54.

(328) Cybulski, S. M.; Bledson, T. M.; Toczylowski, R. R. *The Journal of Chemical Physics* **2002**, *116*, 11039.

(329) Halgren, T. A. *Journal of the American Chemical Society* **1992**, *114*, 7827.

(330) Slater, J. C.; Kirkwood, J. G. *Physical Review* **1931**, *37*, 682.

(331) Alonso, J.; Mañanes, A. *Theoretical Chemistry Accounts: Theory, Computation, and Modeling (Theoretica Chimica Acta)* **2007**, *117*, 467.

(332) Billeter, S. R.; Curioni, A.; Andreoni, W. *Computational Materials Science* **2003**, *27*, 437.

(333) I.B.M.; Stuttgart, M. P. I. In *CPMD*; 3.9.1 ed. 2007.

(334) Megyes, T.; Balint, S.; Grosz, T.; Radnai, T.; Bako, I.; Almasy, L. *The Journal of Chemical Physics* **2007**, *126*, 164507.

(335) Winey, J. M.; Gupta, Y. M. *The Journal of Physical Chemistry B* **1997**, *101*, 10733.

(336) Kuklja, M. M.; Rashkeev, S. N. *Applied Physics Letters* **2007**, *90*, 151913.

(337) Majano, G.; Mintova, S.; Bein, T.; Klapotke, T. M. *The Journal of Physical Chemistry C* **2007**, *111*, 6694.

(338) Kuklja, M. M.; Zerilli, F. J.; Peiris, S. M. *The Journal of Chemical Physics* **2003**, *118*, 11073.

(339) Dobratz, B. M. *The Insensitive High Explosive Triaminotrinitrobenzene (Tatb): Development and Characterization, 1888 to 1994*, Los Alamos Scientific Laboratory, 2008.

(340) Zhang, C. *The Journal of Physical Chemistry B* **2007**, *111*, 14295.

(341) Manaa, M. R.; Gee, R. H.; Fried, L. E. *The Journal of Physical Chemistry A* **2002**, *106*, 8806.

(342) Liu, H.; Zhao, J.; Du, J.; Gong, Z.; Ji, G.; Wei, D. *Physics Letters A* **2007**, *367*, 383.

(343) Choi, C. S.; Boutin, H. P. *Acta Crystallographica Section B* **1970**, *26*, 1235.

(344) Cavagnat, D.; Magerl, A.; Vettier, C.; Anderson, I. S.; Trevino, S. F. *Physical Review Letters* **1985**, *54*, 193.

(345) Ojeda, O. U.; Cagin, T. *Journal of Molecular Structure: THEOCHEM* **2011**, *To be submitted*.

(346) Baranyai, A.; Welberry, T. R. *Molecular Physics* **1991**, *73*, 1317.

(347) Trotter, J.; Williston, C. S. *Acta Crystallographica* **1966**, *21*, 285.

(348) Wojcik, G.; Mossakowska, I.; Holband, J.; Bartkowiak, W. *Acta Crystallographica Section B* **2002**, *58*, 998.

(349) *Elastic Properties of Solids : Biological and Organic Materials, Earth and Marine Sciences*; Levy, M. ed.; Academic Press: San Diego, Calif. , 2001.

(350) Birch, F. *Journal of Geophysical Research* **1978**, *83*, 1257.

(351) Shaw, R. *International Journal of Chemical Kinetics* **1973**, *5*, 261.

(352) Zeman, S. *Thermochimica Acta* **1995**, *261*, 195.

(353) Brill, T. B.; James, K. J. *The Journal of Physical Chemistry* **1993**, *97*, 8752.

(354) *Side Reactions in Organic Synthesis : A Guide to Successful Synthesis Design*; Dorwald, F. Z. ed.; Wiley-VCH: Weinheim, Germany 2005.

(355) Zhang, C.; Shu, Y.; Huang, Y.; Zhao, X.; Dong, H. *The Journal of Physical Chemistry B* **2005**, *109*, 8978.

(356) Manaa, M. R.; Fried, L. E. *The Journal of Physical Chemistry A* **1998**, *102*, 9884.

(357) *Thermal Decomposition and Combustion of Explosives and Propellants*; Manelis, G. B. ed.; Taylor & Francis: London, 2003.

(358) Sorescu, D. C.; Rice, B. M.; Thompson, D. L. *The Journal of Physical Chemistry B* **1999**, *103*, 6783.

(359) Kuklja, M. M.; Kunz, A. B. *Journal of Applied Physics* **1999**, *86*, 4428.

(360) Yuan, L.; Smith, A. C. *Journal of Loss Prevention in the Process Industries* **2009**, *22*, 426.

(361) Woodward, J. L.; Ketchum, D. E. *Journal of Loss Prevention in the Process Industries* **2001**, *14*, 251.

(362) Arman, B.; An, Q.; Luo, S. N.; Tonks, D. L.; Cagin, T.; Goddard, I. W. A.; Desai, T. G. *Journal of Applied Physics* **2011**, *109*.

(363) Winey, J. M.; Gupta, Y. M. *Journal of Applied Physics* **2001**, *90*, 1669.

(364) Perry, A. *Operations Research* **1978**, *26*, 1073.

(365) Bernhard Schlegel, H. *Theoretical Chemistry Accounts: Theory, Computation, and Modeling (Theoretica Chimica Acta)* **1984**, *66*, 333.

(366) Towler, M. D.; Zupan, A.; Causà, M. *Computer Physics Communications* **1996**, *98*, 181.

(367) Binkley, J. S.; Pople, J. A.; Hehre, W. J. *Journal of the American Chemical Society* **1980**, *102*, 939.

(368) Ditchfield, R.; Hehre, W. J.; Pople, J. A. *The Journal of Chemical Physics* **1971**, *54*, 724.

(369) Civalleri, B.; Doll, K.; Zicovich-Wilson, C. M. *The Journal of Physical Chemistry B* **2006**, *111*, 26.

(370) Schafer, A.; Horn, H.; Ahlrichs, R. *The Journal of Chemical Physics* **1992**, *97*, 2571.

(371) Ferro, D.; Barone, G.; Della Gatta, G.; Piacente, V. *The Journal of Chemical Thermodynamics* **1987**, *19*, 915.

(372) Birch, F. *Journal of Geophysical Research* **1978**, *83*, 1257.

(373) *Thermodynamics of Crystals*; Wallace, D. C. ed.; Dover: New York, 1972.

(374) *Solid State Physics. Volume 7*; Seitz; Turnbull ed.; Academic Press: 1958.

(375) Kohn, W.; Meir, Y.; Makarov, D. E. *Physical Review Letters* **1998**, *80*, 4153.

(376) Martyna, G. J.; Tobias, D. J.; Klein, M. L. *Journal of Chemical Physics* **1994**, *101*, 4177.

(377) Parrinello, M.; Rahman, A. *Journal of Applied Physics* **1981**, *52*, 7182.

(378) Kimmel, A. V.; Sushko, P. V.; Shluger, A. L.; Kuklja, M. M. *The Journal of Physical Chemistry A* **2008**, *112*, 4496.

(379) Trotter, J. *Acta Crystallographica* **1963**, *16*, 698.

(380) Courtecuisse, S.; Cansell, F.; Fabre, D.; Petitet, J.-P. *The Journal of Chemical Physics* **1995**, *102*, 968.

(381) Citroni, M.; Datchi, F.; Bini, R.; DiVaira, M.; Pruzan, P.; Canny, B.; Schettino, V. *J. Phys. Chem. B* **2008**, *112*, 1095.

(382) Conroy, M. W.; Oleynik, I. I.; Zybin, S. V.; White, C. T. *The Journal of Physical Chemistry A* **2009**, *113*, 3610.

(383) Piermarini, G. J.; Block, S.; Miller, P. J. *The Journal of Physical Chemistry* **1989**, *93*, 457.

(384) Reilly, A. M.; Habershon, S.; Morrison, C. A.; Rankin, D. W. H. *The Journal of Chemical Physics* **2010**, *132*, 094502.

(385) Hervouet, A.; Desbiens, N.; Bourasseau, E.; Maillet, J. B. *J. Phys. Chem. B* **2008**, *112*, 5070.

(386) Soulard, L.; Bauer, F. In *Shock Compression of Condensed Matter*; Schmidt, S. C., Johnson, J. N., Davidson, L. W., Eds.; Elsevier: Albuquerque, NM, 1989.

(387) Kamlet, M. J.; Adolph, H. G. *Propellants, Explosives, Pyrotechnics* **1979**, *4*, 30.

(388) Pravica, M.; Yulga, B.; Liu, Z.; Tschauner, O. *Physical Review B* **2007**, *76*, 064102.

(389) Baldridge, K. K.; Siegel, J. S. *Journal of the American Chemical Society* **1993**, *115*, 10782.

(390) Son, S. F.; Asay, B. W.; Henson, B. F.; Sander, R. K.; Ali, A. N.; Zielinski, P. M.; Phillips, D. S.; Schwarz, R. B.; Skidmore, C. B. *The Journal of Physical Chemistry B* **1999**, *103*, 5434.

(391) Zhang, C.; Yuanjie, S.; Xiadong, Z.; Dong, H. *Central European Journal of Energetic Materials* **2004**, *1*, 43.

(392) Gee, R. H.; Maiti, A.; Fried, L. E. *Applied Physics Letters* **2007**, *90*, 254105.

(393) Zhang, C. *The Journal of Physical Chemistry B* **2007**, *111*, 14295.

(394) Balu, R.; Byrd, E. F. C.; Rice, B. M. *The Journal of Physical Chemistry B* **2011**, *115*, 803.

(395) Liu, K.; Wang, Y.; Tu, Y.; Agren, H.; Luo, Y. *The Journal of Physical Chemistry B* **2008**, *112*, 4387.

(396) Oxley, J. C.; Smith, J. L.; Ye, H.; McKenney, R. L.; Bolduc, P. R. *The Journal of Physical Chemistry* **1995**, *99*, 9593.

(397) Satija, S. K.; Swanson, B.; Eckert, J.; Goldstone, J. A. *The Journal of Physical Chemistry* **1991**, *95*, 10103.

(398) Sharma, J.; Beard, B. C.; Chaykovsky, M. *The Journal of Physical Chemistry* **1991**, *95*, 1209.

(399) Sharma, J.; Forbes, J. W.; Coffey, C. S.; Liddiard, T. P. *The Journal of Physical Chemistry* **1987**, *91*, 5139.

(400) Sharma, J.; Garrett, W. L.; Owens, F. J.; Vogel, V. L. *The Journal of Physical Chemistry* **1982**, *86*, 1657.

(401) Sorescu, D. C.; Rice, B. M. *The Journal of Physical Chemistry C* **2010**, *114*, 6734.

(402) Trott, W. M.; Renlund, A. M. *The Journal of Physical Chemistry* **1988**, *92*, 5921.

(403) Manaa, M. R.; Schmidt, R. D.; Overturf, G. E.; Watkins, B. E.; Fried, L. E.; Kolb, J. R. *Thermochimica Acta* **2002**, *384*, 85.

(404) Brill, T. B.; James, K. J. *Chemical Reviews* **1993**, *93*, 2667.

(405) Millar, D. I. A.; Marshall, W. G.; Oswald, I. D. H.; Pulham, C. R. *Crystallography Reviews* **2010**, *16*, 115

(406) Politzer, P.; Boyd, S. *Structural Chemistry* **2002**, *13*, 105.

(407) Lee, E. L.; Tarver, C. M. *Physics of Fluids* **1980**, *23*, 2362.

(408) Tarver, C. M. *The Journal of Physical Chemistry A* **2010**, *114*, 2727.

(409) Manaa, M. R.; Reed, E. J.; Fried, L. E.; Goldman, N. *Journal of the American Chemical Society* **2009**, *131*, 5483.

(410) Saw, C. K.; Zaug, J. M.; Farber, D. L.; Weeks, B. L.; Aracne, C. M. *AIP Conference Proceedings* **2002**, *620*, 856.

(411) Gee, R. H.; Roszak, S.; Balasubramanian, K.; Fried, L. E. *The Journal of Chemical Physics* **2004**, *120*, 7059.

(412) Pastine, D. J.; Bernecker, R. R. *Journal of Applied Physics* **1974**, *45*, 4458.

(413) *An Ab Initio Study of Nitromethane, Hmx, Rdx, Cl-20, Petn, and Tatb*; Byrd, E. F. C.; Chabalowski, C. F.; Rice, B. M. ed.; Science Press Beijing: Beijing, 2007.

(414) Phillips, D. S.; Schwarz, R. B.; Skidmore, C. B.; Hiskey, M. A.; Son, S. F. *AIP Conference Proceedings* **2000**, *505*, 707.

(415) Kolb, J. R.; Rizzo, H. F. *Propellants, Explosives, Pyrotechnics* **1979**, *4*, 10.

(416) Catalano, E.; Rolon, C. E. *Thermochimica Acta* **1983**, *61*, 53.

(417) Foltz, M. F. In *13th Symposium (International) on Detonation* Norfolk, Virginia, USA, 2006, p 997.

(418) Pravica, M.; Yulga, B.; Tkachev, S.; Liu, Z. *The Journal of Physical Chemistry A* **2009**, *113*, 9133.

(419) Su-Hong, G.; Xin-Lu, C.; Li-Sha, W.; Xiang-Dong, Y. *Journal of Molecular Structure: THEOCHEM* **2007**, *809*, 55.

(420) *Molecular Vibrations; the Theory of Infrared and Raman Vibrational Spectra*; Wilson, E. B.; Decius, J. C.; Cross, P. C. ed.; McGraw-Hill: New York, 1955.

(421) Monkhorst, H. J.; Pack, J. D. *Physical Review B* **1976**, *13*, 5188.

(422) Çağin, T.; Pettitt, B. M. *Physical Review B* **1989**, *39*, 12484.

(423) Makashir, P. S.; Kurian, E. M. *Journal of Thermal Analysis and Calorimetry* **1996**, *46*, 225.

(424) Holy, J. A. *The Journal of Physical Chemistry B* **2008**, *112*, 7489.

(425) Deopura, B. L.; Gupta, V. D. *The Journal of Chemical Physics* **1971**, *54*, 4013.

(426) Towns, T. G. *Spectrochimica Acta Part A: Molecular Spectroscopy* **1983**, *39*, 801.

(427) Brill, T. B.; Royce, W. B. *Applied Spectroscopy* **2005**, *59*, 1194.

(428) McGrane, S. D.; Shreve, A. P. *The Journal of Chemical Physics* **2003**, *119*, 5834.

(429) Cady, H.; Olinger, B. In *Symposium (International) on Detonation (6th)* Coronado, California, 1976, p 700.

(430) Roszak, S.; Gee, R. H.; Balasubramanian, K.; Fried, L. E. *Chemical Physics Letters* **2003**, *374*, 286.

(431) Manaa, M. R.; Fried, L. E. *The Journal of Physical Chemistry A* **2001**, *105*, 6765.

(432) Borisenko, K. B.; Hargittai, I. n. *Journal of Molecular Structure* **1996**, *382*, 171.

(433) Kennedy, J. E.; Lee, K.-Y.; Son, S. F.; Martin, E. S.; Asay, B. W.; Skidmore, C. B. In *Second-harmonic generation and the shock sensitivity of TATB*; 1 ed.; Furnish, M. D., Chhabildas, L. C., Hixson, R. S., Eds.; AIP: Snowbird, Utah (USA), 2000; Vol. 505, p 711.

(434) Gan, C. K.; Sewell, T. D.; Challacomb, M. *Physical Review B* **2004**, *69*.

(435) Hill, R. *Mathematical Proceedings of the Cambridge Philosophical Society* **1975**, *77*, 225.

(436) Czerski, H.; Proud, W. G. *Journal of Applied Physics* **2007**, *102*, 113515.

(437) Landerville, A. C.; Oleynik, I. I.; White, C. T. *The Journal of Physical Chemistry A* **2009**, *113*, 12094.

(438) Lionel Borne, J.-C. P., Christian Spyckerelle, *Propellants, Explosives, Pyrotechnics* **1999**, *24*, 255.

(439) Antoine E. D. M. van der Heijden, Yves L. M. C., Emanuela Marino, Richard H. B. Bouma, Gert J. H. G. Scholtes, Willem Duvalois, Marc C. P. M. Roelands, *Propellants, Explosives, Pyrotechnics* **2008**, *33*, 25.

(440) Ruth M. Doherty, Duncan S. W. *Propellants, Explosives, Pyrotechnics* **2008**, *33*, 4.

(441) Zepeda-Ruiz, L. A.; Maiti, A.; Gee, R.; Gilmer, G. H.; Weeks, B. L. *Journal of Crystal Growth* **2006**, *291*, 461.

(442) Lozano, A.; Fernandez, J. In *Surface Hardening of Railway Crossings Comprises High Frequency Generation and Sonic Impacting Prior to Explosion on Hardened Surface*; European, P. O., Ed.; Corral, Bescos M.: Spain, 2007; Vol. ES2275366, p 7.

(443) Hartmut Kröber, U. T. *Propellants, Explosives, Pyrotechnics* **2008**, *33*, 33.

(444) Gallagher, H. G.; Halfpenny, P. J.; Miller, J. C.; Sherwood, J. N.; Tabor, D. *Philosophical Transactions: Physical Sciences and Engineering* **1992**, *339*, 293.

(445) Bouyer, V.; Darbord, I.; Hervé, P.; Baudin, G.; Le Gallic, C.; Clément, F.; Chavent, G. *Combustion and Flame* **2006**, *144*, 139.

(446) Tarasov, M.; Karpenko, I.; Sudovtsov, V.; Tolshmyakov, A. *Combustion, Explosion, and Shock Waves* **2007**, *43*, 465.

(447) Mathews, K. Y.; Ball, D. W. *Journal of Molecular Structure: THEOCHEM* **2009**, *902*, 15.

(448) Kwok, W. M.; Hung, M. S.; Phillips, D. L. In *Molecular Physics*; Taylor & Francis Ltd: London, 1996; Vol. 88, p 517.

(449) Yin, K.; Zou, D.; Zhong, J.; Xu, D. *Computational Materials Science* **2007**, *38*, 538.

(450) Parrinello, M.; Rahman, A. *Physical Review Letters* **1980**, *45*, 1196.

(451) Ojeda, O.; Cagin, T. *Journal of Physical Chemistry B* **2011**, *Submitted*.

(452) Keating, P. N. *Physical Review* **1966**, *145*, 637.

(453) Guanghua, G.; et al. *Nanotechnology* **1998**, *9*, 184.

(454) Andersen, H. C. *The Journal of Chemical Physics* **1980**, *72*, 2384.

(455) Cagin, T.; Ray, J. R. *Physical Review B* **1988**, *38*, 7940.

(456) Kalay, M.; Kart, H. H.; Ozdemir Kart, S.; Cagin, T. *Journal of Alloys and Compounds* **2009**, *484*, 431.

(457) Ojeda, O.; Cagin, T. *Phisica Status Solidi A* **2011**, *Submitted*.

(458) Accelrys Software, I. In *Accelrys, Materials Studio Release Notes* San Diego, 2008.

(459) Yamaguchi, G.; Yanagida, H. *Bulletin of the Chemical Society of Japan* **1963**, *36*, 1155.

(460) Corbin, N. D. *Journal of the European Ceramic Society* **1989**, *5*, 143.

(461) McCauley, J. W.; Corbin, N. D. *Journal of the American Ceramic Society* **1979**, *62*, 476.

(462) Thomas, M. E.; Joseph, R. I.; Tropf, W. J. *Applied Optics* **1988**, *27*, 239.

(463) Hartnett, T. M.; Bernstein, S. D.; Maguire, E. A.; Tustison, R. W. *Infrared Physics & Technology* **1998**, *39*, 203.

(464) Patel, P. J.; Gilde, G. A.; Dehmer, P. G.; McCauley, J. W. In *Transparent Ceramics for Armor and EM Window Applications*; 1 ed.; Marker Iii, A. J., Arthurs, E. G., Eds.; SPIE: San Diego, CA, USA, 2000; Vol. 4102, p 1.

(465) Sharma, M.; Nickel, J. H.; Anthony, T. C.; Wang, S. X. *Applied Physics Letters* **2000**, *77*, 2219.

(466) Zhu, M.; Tung, C.-H.; Yeo, Y.-C. *Applied Physics Letters* **2006**, *89*, 202903.

(467) Soares, G. V.; Bastos, K. P.; Pezzi, R. P.; Miotti, L.; Driemeier, C.; Baumvol, I. J. R.; Hinkle, C.; Lucovsky, G. *Applied Physics Letters* **2004**, *84*, 4992.

(468) Poyai, A.; Bunjongpru, W.; Klunngien, N.; Porntheerapat, S.; Hruanan, C.; Sopitpan, S.; Nukeaw, J. *Materials Science in Semiconductor Processing* **2008**, *11*, 319.

(469) Berriche, Y.; Vallayer, J.; Trabelsi, R.; Treheux, D. *Journal of the European Ceramic Society* **2000**, *20*, 1311.

(470) Shikha, D.; Jha, U.; Sinha, S. K.; Singh, A. K.; Barhai, P. K.; Nair, K. G. M.; Dash, S.; Tyagi, A. K.; Kothari, D. C. *International Journal of Applied Ceramic Technology* **2010**, *7*, 156.

(471) McMillan, P. F.; Sato, R. K.; Poe, B. T. *Journal of Non-Crystalline Solids* **1998**, *224*, 267.

(472) Willems, H. X.; Hendrix, M. M. R. M.; de With, G.; Metselaar, R. *Journal of the European Ceramic Society* **1992**, *10*, 339.

(473) Willems, H. X.; Hendrix, M. M. R. M.; Metselaar, R.; de With, G. *Journal of the European Ceramic Society* **1992**, *10*, 327.

(474) McCauley, J. W.; Patel, P.; Chen, M.; Gilde, G.; Strassburger, E.; Paliwal, B.; Ramesh, K. T.; Dandekar, D. P. *Journal of the European Ceramic Society* **2009**, *29*, 223.

(475) Tabary, P.; Servant, C. *Journal of Applied Crystallography* **1999**, *32*, 241.

(476) Willems, H. X.; de With, G.; Metselaar, R. *Journal of the European Ceramic Society* **1993**, *12*, 43.

(477) Bartram, S. F.; Slack, G. A. *Acta Crystallographica Section B* **1979**, *35*, 2281.

(478) Fitzgerald, J. J.; Kohl, S. D.; Piedra, G.; Dec, S. F.; Maciel, G. E. *Chemistry of Materials* **1994**, *6*, 1915.

(479) Granon, A.; Goeuriot, P.; Thevenot, F.; Guyader, J.; L'Haridon, P.; Laurent, Y. *Journal of the European Ceramic Society* **1994**, *13*, 365.

(480) Shimpo, A.; Ide, H.; Ueki, M. *Nippon Seramikkusu Kyokai Gakujutsu Ronbunshi-Journal of the Ceramic Society of Japan* **1992**, *100*, 504.

(481) Halitim, F.; et al. *Journal of Physics D: Applied Physics* **1997**, *30*, 330.

(482) Klaumünzer, S.; Hou, M.-d.; Schumacher, G. *Physical Review Letters* **1986**, *57*, 850.

(483) Kong, M.; Wu, X.; Huang, B.; Li, G. *Journal of Alloys and Compounds* **2009**, *485*, 435.

(484) Franchy, R.; Schmitz, G.; Gassmann, P.; Bartolucci, F. *Applied Physics A: Materials Science & Processing* **1997**, *65*, 551.

(485) Willems, H. X.; Van Hal, P. F.; De With, G.; Metselaar, R. *Journal of Materials Science* **1993**, *28*, 6185.

(486) Graham, E. K.; Munly, W. C.; McCauley, J. W.; Corbin, N. D. *Journal of the American Ceramic Society* **1988**, *71*, 807.

(487) Singh, R.; Gao, H.; Meshri, D.; Shreeve, J. N. In *High Energy Density Materials* 2007, p 35.

VITA

Name: Oscar Ulises Ojeda Mota

Address: Artie McFerrin Department of Chemical Engineering
Texas A&M University, Jack E. Brown Engineering Bldg.
3122 TAMU Room 200,College Station, TX 77843-3122
c/o Dr. T. Cagin.

Email Address: molecular.oscar@gmail.com

Education: B.S., Chemical Engineering, National Polytechnic Institute, 2003
M.S., Analytical Chemistry, University of North Texas, 2005
Ph.D., Chemical Engineering, Texas A&M University, 2011